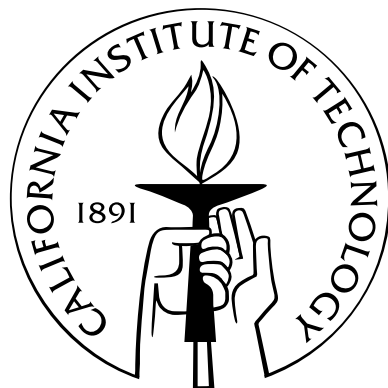


**The Physics of Ultracold Neutrons and Fierz Interference in  
Beta Decay**

Thesis by  
Kevin Peter Hickerson

In Partial Fulfillment of the Requirements  
for the Degree of  
Doctor of Philosophy



California Institute of Technology  
Pasadena, California

2013  
(Defended October 9, 2012)

© 2013

Kevin Peter Hickerson

All Rights Reserved

# Acknowledgements

I am very indebted to my research adviser, Dr. Bradley Filippone, who kindly asked me to join his research group, led me toward a rewarding path into nuclear physics, and gave precious advice to work and experiment with ultracold neutrons.

I am appreciative of my previous employer, Bill Gross, who enabled me to pursue my work outside of physics, ranging in far-reaching fields such as tablet computing, rapid prototyping, low-cost food production, and my personal favorite, solar energy.

I wish to show much appreciation to Dr. Chris Morris, Dr. Mark Makela, Dr. Takeyasu Ito, John Ramsey, Walter Sondheim and Dr. Andy Saunders of Los Alamos National Laboratory, whose ingenuity and creativity and mentoring were invaluable for designing the many neutron experiments we performed at LANSCE.

I am also grateful to all the graduate students and postdocs who have worked on the ultracold neutron projects with me. Their hard work and late hours make these experiments successful.

Finally, I am very grateful to my family, my friends, my wife, Anna, and my children, Melanie, Brian, and Jack for tolerating my many long trips to Los Alamos to work on this research and supporting me during my years in graduate school.

# Abstract

In the first component of this thesis, we investigate the physics of ultacold neutrons (UCN). UCN are neutrons so cold they can be stored inside of material, magnetic and gravitational bottles. Using this property we use UCN nonimaging optics to design a type of reflector that directs UCN upward in to vertical paths. Next we examine UCN passing through thin, multilayered foils. In the remaining sections we investigate the so-called Fierz interference term of free neutron beta decay, denoted  $b_n$ . It is theorized that contributions to scalar and tensor interactions from physics beyond the Standard Model could be detectable in the spectrum of neutron beta decay, manifest as a nonzero value for  $b_n$ . We investigate three techniques for measuring  $b_n$ . The first is to use the primordial helium abundance fraction and compare that to predictive Big Bang nucleosynthesis calculations. Second we extract  $b_n$  from the spectral shape generated by the 2010 data set of the UCNA experiment. Third, we discuss progress toward constructing the UCNb experimental prototype. We present the design of this new experiment that uses the UCN source at LANSCE for measuring  $b_n$ , in which UCN are guided into a shielded  $4\pi$  calorimeter where they are stored and decay. From Big Bang nucleosynthesis we can place the limit  $0.021 < b_n < 0.277$  (90% C.L.) on the neutron Fierz term and from the UCNA 2010 data we set  $-0.044 < b_n < 0.218$  (90% C.L.).

# Preface

This thesis is, at its core, about searching for new physics. In particular, it is about looking for Fierz interference by observing the decay of ultracold neutrons (UCN). Along the way toward that goal, I have performed many other experiments dealing with ultracold neutron physics that I also discuss.

Ultracold neutrons, an exotic state of free neutrons, are so cold, just 1/1000th of a degree above absolute zero, that they can be trapped in bottles and guides. Ultracold neutrons reflect off some smooth surfaces just like photons. There is one catch: photons move in straight lines, but neutrons have mass and move slowly enough that they are affected by Earth's gravity. Ultracold neutrons bounce about as high a basketball hoop, so their parabolic paths cannot be ignored.

I have divided the body of work into three major parts.

The first part covers the physics of neutrons in the Standard Model. In particular, we begin by developing the Standard Model, as generally as possible, and then move toward a more specific derivation of the components needed to discuss the known physics of the neutron. I then discuss several experiments involving ultracold neutrons (UCN). One such proposed experiment uses UCN nonimaging optics. Another experiment measured UCN transmission through zirconium foils of various thicknesses, resulting in an increase in UCN density past the foil at the Los Alamos Neutron Science Center in Los Alamos, New Mexico.

The second part of my thesis focuses on Fierz interference and the physics beyond the Standard Model that may manifest itself though a measurable quantity called the Fierz interference term, denoted  $b$  or “little  $b$ ,” of neutron beta decay. This term is essentially zero in the Standard model. Any nonzero value would be an indication of some type of scalar or tensor interaction, previously undiscovered. Obviously, this is a motivating place to look for discovery.

The third part of this work will focus on experimental efforts, both underway and

proposed, that will set new and improved limits on  $b$ . I begin by discussing an important experimental limit from Big Bang nucleosynthesis in the earliest moments of the universe. I spent a considerable amount of my graduate years working on the UCNA experiment. The aim of this experiment is to measure the neutron beta asymmetry. While working on this project, my primary focus during this time was to improve and measure the linearity of the photometric components of the experimental apparatus. While working on this, it became apparent that the UCNA experiment had a high quality beta decay spectrum. I became intrigued by the possibility of extracting the Fierz interference term from this spectrum. This effort paid off as we are able to place limits of  $< 0.13$  (90% C.L.) on  $b$ . Also of tremendous interest to me was the possibility of constructing a new, dedicated experiment to measure  $b$  in an apparatus optimized for high precision measurement of an UCN beta decay spectrum. This experiment would be called UCNb.

During these studies we discovered two interesting facts. First, that UCNA had surprising systematic sensitivity to  $b$  and second, measuring  $b$  requires large statistics that could be achieved, not in UCNA, but in this new experiment dedicated to measuring  $b$ . I am happy to have been given the opportunity to work at the ultracold neutron source at LANSCE that makes collecting such large statistics possible. It is an excellent location for situating an experiment like UCNb. The UCN source there is able to provide a large density of UCN, of about 60 UCN/cc. This large density is ideal for placing a simple calorimeter as close to the source as allowed by the concrete shield package.

I designed and constructed a significant fraction of the new UCNb experiment. I am hopeful that my efforts have begun a sequence of experiments towards the goal of measuring  $b$  to  $10^{-4}$ . As I will discuss, this limit is believed to be a range of significant scientific value for searching for new TeV-scale physics beyond the Standard Model.

Kevin Peter Hickerson

# Contents

<b>List of Figures</b>	<b>xi</b>
<b>List of Tables</b>	<b>xv</b>
<b>1 The Standard Model</b>	<b>1</b>
1.0.1 Yang-Mills Theory . . . . .	2
1.1 Particles, forces, and interactions . . . . .	3
1.1.1 Fermions . . . . .	3
1.1.2 Leptons and Quarks . . . . .	3
1.2 CKM matrix . . . . .	4
1.3 The $\theta$ -term . . . . .	5
1.4 Neutron electric dipole moment . . . . .	6
<b>2 The Neutron</b>	<b>7</b>
2.1 Why Study the Neutron? . . . . .	7
2.2 Beta Decay . . . . .	8
2.2.1 Symmetries of the Four Fermion Interaction . . . . .	9
2.3 Vector and Axial Vector Currents . . . . .	10
2.3.1 The Neutron $\beta$ Decay Spectrum . . . . .	11
2.3.2 Alphabet Soup . . . . .	13
2.3.3 The Neutron Lifetime . . . . .	13
2.3.3.1 The Lifetime Problem . . . . .	15
2.4 Ultracold Neutrons . . . . .	15
2.4.1 The Fermi Potential . . . . .	16
2.4.2 Magnetic Fields . . . . .	16
2.4.3 The Gravitational Potential . . . . .	17

<b>3 The Neutron Beyond the Standard Model</b>	<b>18</b>
3.1 Beyond V – A . . . . .	18
3.1.1 General Effective Lagrangian . . . . .	19
3.2 Fierz Interference . . . . .	19
3.2.1 The Standard Model Fierz Interference Term . . . . .	20
3.2.2 Spectral Effects of Fierz Interference . . . . .	21
3.2.3 The Fermi and Gamow-Teller Combination . . . . .	22
3.3 Supersymmetry . . . . .	24
3.3.1 Minimal Supersymmetric Standard Model . . . . .	24
3.3.2 Next-to-Minimal Supersymmetric Standard Model . . . . .	27
3.4 Leptoquarks . . . . .	27
3.4.1 Leptoquark Contributions to Fierz Interference . . . . .	27
3.4.2 Leptoquark Mixing . . . . .	28
3.5 Experimental Limits . . . . .	31
<b>4 Ultracold Neutron Nonimaging Optics</b>	<b>33</b>
4.1 Introduction . . . . .	33
4.2 Nonimaging UCN Optics . . . . .	34
4.3 Compound Parabolic Concentrators . . . . .	35
4.4 Monte Carlo Simulation . . . . .	40
4.5 Results . . . . .	40
4.6 Applications . . . . .	42
4.6.1 Measuring the Neutron Lifetime . . . . .	42
4.6.2 Pulsed UCN Source Using a CPC . . . . .	43
4.7 Conclusion . . . . .	44
<b>5 Transmission of Ultracold Neutrons Through Thin Foils</b>	<b>46</b>
5.1 1D Quantum Model . . . . .	47
5.2 Foil Measurements . . . . .	51
5.2.1 Depth Profilometry . . . . .	51
5.2.2 Experimental Setup . . . . .	51
5.2.3 Results . . . . .	52
5.2.4 Summary . . . . .	54

<b>6 Cosmological Limits on Fierz Interference</b>	<b>56</b>
6.1 Big Bang Nucleosynthesis . . . . .	57
6.2 BBN Simulation Code . . . . .	59
6.3 Simulation Results . . . . .	60
<b>7 Extracting the Fierz Term from <math>\beta</math>-asymmetry Measurements</b>	<b>63</b>
7.1 The UCNA Experiment . . . . .	64
7.1.1 UCNA Gain Monitoring System . . . . .	66
7.2 Overview of Analysis Procedures . . . . .	69
7.2.1 Rate Model . . . . .	69
7.2.2 Asymmetry and Energy Spectrum . . . . .	70
7.3 Estimation of Systematic Errors on $b$ from UCNA . . . . .	72
7.3.1 Analytical Detector Model . . . . .	74
7.3.2 Backscatter Effects on Asymmetry and $b$ Extraction . . . . .	76
7.3.3 Biased Polarization . . . . .	76
7.3.4 Simulation Study of Systematics . . . . .	77
7.4 Results from UCNA data . . . . .	80
<b>8 The UCNb Experiment</b>	<b>94</b>
8.1 Detector concept . . . . .	94
8.2 Modeling UCNb . . . . .	96
8.2.1 The integrating sphere . . . . .	96
8.2.2 Monte Carlo . . . . .	97
8.3 Error budget . . . . .	99
8.3.1 Response function . . . . .	99
8.3.2 Inherent $\gamma$ backgrounds . . . . .	100
8.3.3 UCN generated backgrounds . . . . .	101
8.3.4 Lead shield . . . . .	102
8.4 Calibration and gain monitoring . . . . .	102
8.4.1 Insertable sources . . . . .	104
8.4.2 Other calibration sources . . . . .	105
8.5 The experiment . . . . .	106
8.5.1 Mechanical setup . . . . .	107

8.5.2 Electronics . . . . .	108
8.6 Results . . . . .	110
<b>9 Future Directions</b>	<b>118</b>
9.1 Upgrades for UCNb . . . . .	118
9.2 Future Run plans . . . . .	120
9.3 Toward $10^{-4}$ . . . . .	120
<b>Appendix A <i>n</i>-forms</b>	<b>121</b>
<b>Appendix B Leptoquarks</b>	<b>122</b>
<b>Appendix C Asymmetry dilution from thin foils</b>	<b>125</b>
<b>Bibliography</b>	<b>128</b>

# List of Figures

2.1	The Feynman diagram for neutron $\beta$ -decay. . . . .	8
2.2	Weak interaction of the quarks with the mixing element of the CKM matrix. . . . .	9
2.3	The Feynman diagram for neutron four-fermion interaction. . . . .	10
2.4	The Feynman diagram for effective neutron $\beta$ -decay. . . . .	11
2.5	Strong renormalization of $g_V$ leaving charge current conserved. . . . .	11
2.6	An ideal beta decay spectrum of the neutron. . . . .	12
3.1	One loop contributions from the Standard Model. . . . .	21
3.2	Neutron spectrum probability function with a Fierz interference term. . . . .	22
3.3	The Fierz ratio shown for different values of $b$ . . . . .	23
3.4	One loop contributions from MSSM. . . . .	24
3.5	The Feynman diagrams for LQ quark-lepton mixing. . . . .	30
3.6	Possible experimental limits on $\varepsilon_S$ and $\varepsilon_T$ . . . . .	32
3.7	Plot of possible experimental limits on $\varepsilon_S$ and $\varepsilon_T$ . . . . .	32
4.1	A CPC with a slice cut out. . . . .	36
4.2	A CPC using the “neutron fountain” property. . . . .	37
4.3	A 3D Monte Carlo simulation of a vertical CPC . . . . .	41
4.4	Monochromatic UCN simulations for different energy levels. . . . .	42
5.1	The potential of a thin coated foil. . . . .	48
5.2	Depth profile of cleaned Zr foils . . . . .	52
5.3	Experimental setup for the foil transmission measurements. . . . .	53
5.4	Absolute transmission of UCN through Zr foils. . . . .	54
5.5	Relative transmission of UCN through Zr foils . . . . .	55
6.1	Mass fraction relative to hydrogen as a function of Baryon temperature. . . . .	60

6.2	BBN fit with different values for $b_n$ .	61
7.1	Detail of the Area B experimental hall at LANSCE.	64
7.2	Detail of the SCS experimental setup.	66
7.3	Optical schematic of the LED/PD pair gain and linearity monitoring system.	67
7.4	The linearity of an hour long run.	69
7.5	Plots of resolution and threshold functions	75
7.6	Control studies.	82
7.7	Linearity studies	83
7.8	Quadratic linearity studies	84
7.9	Quartic linearity studies	85
7.10	Resolution studies	86
7.11	Endpoint studies	87
7.12	Background studies	88
7.13	East and west backgrounds from UCNA 2010 data.	88
7.14	Background studies	89
7.15	Combination studies	90
7.16	Comparison of UCNA 2010 data and GEANT4.	91
7.17	Residual of UCNA 2010 data and GEANT4.	91
7.18	Comparison of the UCNA 2010 data and the PENELOPE.	92
7.19	Residual of UCNA 2010 data and PENELOPE.	92
7.20	Fierz ratio of UCNA 2010 data and GEANT4.	93
7.21	Fierz ratio of UCNA 2010 data and the PENELOPE.	93
8.1	The scintillator assembly for UCNb	95
8.2	The MgF <sub>2</sub> polystyrene scintillator box inside the integrating cube	96
8.3	One of the Monte Carlo 2012 geometry used as generated by GEANT4	98
8.4	GEANT4 simulation of 10 keV electrons	99
8.5	GEANT4 events directed toward a detector or toward a wall.	100
8.6	GEANT4 events in the center or the corner	101
8.8	The schematic of the Hamamatsu R7725 base design.	104
8.9	An insertable source used for calibrating.	105
8.10	A detailed schematic of the insertable source.	106

8.11	Exterior $^{60}\text{Co}$ source . . . . .	107
8.12	Exterior $^{137}\text{Cs}$ source . . . . .	108
8.13	Activated Xe run in the large DPS geometry. . . . .	109
8.14	Experimental setup for the foil transmission measurements. . . . .	110
8.15	The Spectralon reflector. . . . .	111
8.16	CAD drawing of the UCNb experiment. . . . .	112
8.17	CAD drawing of a cross section of the UCNb experiment. . . . .	113
8.18	Electronic schematic for UCNb NIM electronics . . . . .	114
8.19	A 2D plot of counts per time, by time versus pulse height. . . . .	114
8.20	$^{207}\text{Bi}$ 2010 from a calibration disk. . . . .	115
8.21	$^{113}\text{Sn}$ 2010 from a calibration disk. . . . .	115
8.22	Background-subtracted $^{207}\text{Bi}$ . . . . .	116
8.23	Background-subtracted $^{113}\text{Sn}$ . . . . .	116
8.24	Background-subtracted UCN generated signal from the 2012 run. . . . .	117
8.25	Background from the 2012 run. . . . .	117
9.1	A cartoon of a possible upgrade of the UCNb experiment. . . . .	119
9.2	A cross section of a possible upgrade of the UCNb experiment. . . . .	120



# List of Tables

2.1	Fermi potentials of common building materials . . . . .	16
3.1	Experimental limits on $g_T \epsilon_T$ from $\beta$ -decay . . . . .	31
5.1	Transmission as a function of magnetic field and thickness. . . . .	53
5.2	Foil transmission coefficients as a function of magnetic field strength. . . . .	54
7.1	A summary of numerical systematic studies . . . . .	79
8.1	Possible UCNb scintillator and wall coating material choices. . . . .	95
B.1	Four fermion vertices for leptoquarks inferred from the Lagrangian of reference [1–3] for $F = 0$ . Courtesy Dr. V. Cirigliano and Dr. E. Passemar [4]. . . . .	123
B.2	Four fermion vertices for leptoquarks inferred from the Lagrangian of reference [1–3] for $F = 2$ . Courtesy Dr. V. Cirigliano and Dr. E. Passemar [4]. . . . .	124

# Chapter 1

## The Standard Model

The more you see how strangely  
 Nature behaves, the harder it is to  
 make a model that explains how even  
 the simplest phenomena actually work.  
 So theoretical physics has given up on  
 that.

---

RICHARD FEYNMAN

In this chapter, we introduce the Standard Model in as simple a way as we can with the aim of explaining the physics of neutrons. That being said, the neutron requires almost all of the Standard Model to be understood. We start by introducing the Model by using the metric independent language of  $n$ -forms. From there, we move into a more explicit component form.

To introduce the Standard Model in the most geometrically abstract way possible, using the simplest and shortest description, we make use of  $n$ -forms, the exterior product, and the dual [5]. To begin, we look at the Lagrangian with unity coupling for QCD and QED

$$\mathcal{L}_{\text{QCD}} = -\frac{1}{4} \text{tr } F^2 + \bar{\psi} \not{D} \psi - m \bar{\psi} \psi. \quad (1.1)$$

Now given that  $A$  is a connection for the Lie group  $G$ , the covariant derivative along the connection is the operator given by

$$D = \partial + A. \quad (1.2)$$

Since this is the general theory without renormalization of  $A$  by a coupling constant, the

field curvature  $F$  is

$$F = D \wedge A = dA + A \wedge A, \quad (1.3)$$

where  $dA$  is the exterior derivative of the connection  $A$ . Since the exterior derivative operator is nilpotent  $d^2A = 0$ , the exterior derivative of  $F$ ,

$$dF = dA \wedge A - A \wedge dA, \quad (1.4)$$

which is already a derivative, vanishes. Along with the conserved current,  $J$ , we get the generalized non-abelian Maxwell's equations,

$$\begin{aligned} \partial F &= J, \\ dF &= 0. \end{aligned} \quad (1.5)$$

### 1.0.1 Yang-Mills Theory

We consider a non-abelian compact Lie group  $G$  generated from the Lie algebra  $\mathcal{G}$ . In Yang-Mills Theory, the gauge field is scaled with a coupling constant  $A \rightarrow igA$ , so that now the covariant derivative operator becomes

$$D = \partial + igA. \quad (1.6)$$

We now introduce a new gauge field curvature  $F = D \wedge A$  that in terms of the new coupling

$$F = dA + igA \wedge A. \quad (1.7)$$

The Lagrangian now becomes

$$\mathcal{L}_{\text{YM}} = -\frac{1}{4g^2} \text{tr } F^2. \quad (1.8)$$

If we have more than one gauge group  $G = G_1 \times G_2 \times \dots$ , each with its own coupling constant  $g_1, g_2, \dots$ , the covariant derivative becomes

$$D = \partial - ig_i A^{G_i}. \quad (1.9)$$

The Lie group in the Standard Model is a direct product of specific gauge groups

$$G_{\text{SM}} = \text{U}(1) \times \text{SU}(2) \times \text{SU}(3) \quad (1.10)$$

Each of these gauge groups corresponds to named gauge fields that have observable bosonic fields associated with them.

## 1.1 Particles, forces, and interactions

### 1.1.1 Fermions

For all fermions  $\psi$ , there exist antifermion partners,  $\bar{\psi}$  with equal mass and opposite charge as shown in the Dirac term,

$$\mathcal{L}_D = \bar{\psi}(\not{D} - m)\psi. \quad (1.11)$$

A fermion is spin degenerate with each fermion state possessing half-integer spin. Fundamental fermions in the Standard Model are spin- $\frac{1}{2}$  spinors. They have left- and right-hand components forming doublets

$$\psi \rightarrow \begin{pmatrix} \psi_L \\ \psi_R \end{pmatrix}. \quad (1.12)$$

### 1.1.2 Leptons and Quarks

The mass eigenstates of the fermions of the standard model are labeled into two groups, leptons and quarks. The leptons form three generation doublets of different mass scales,

$$\begin{pmatrix} \nu_e \\ e \end{pmatrix} \begin{pmatrix} \nu_\mu \\ \mu \end{pmatrix} \begin{pmatrix} \nu_\tau \\ \tau \end{pmatrix}. \quad (1.13)$$

The quarks are

$$\begin{pmatrix} u \\ d \end{pmatrix} \begin{pmatrix} c \\ s \end{pmatrix} \begin{pmatrix} t \\ b \end{pmatrix}. \quad (1.14)$$

The antiquarks are

$$\begin{pmatrix} \bar{u} \\ \bar{d} \end{pmatrix} \begin{pmatrix} \bar{c} \\ \bar{s} \end{pmatrix} \begin{pmatrix} \bar{t} \\ \bar{b} \end{pmatrix}, \quad (1.15)$$

which are degenerate in mass and have opposite charge just like any Dirac fermion eigen-

state. The left-handed leptons can be written as the doublets

$$e_i^L = \begin{pmatrix} \nu_i \\ \ell_i^- \end{pmatrix}, \quad (1.16)$$

and the left-handed quarks are written as the doublets

$$u_i^L = \begin{pmatrix} u_i \\ d'_i \end{pmatrix}. \quad (1.17)$$

## 1.2 CKM matrix

For quarks, weak eigenstates are not the same as the mass eigenstates. Instead there is a projection,

$$d'_i = V_{ij} d_j, \quad (1.18)$$

where  $V_{ij}$  is the Cabibbo-Kobayashi-Maskawa matrix given by

$$V_{\text{CKM}} = \begin{pmatrix} V_{ud} & V_{cd} & V_{td} \\ V_{us} & V_{cs} & V_{ts} \\ V_{ub} & V_{cb} & V_{tb} \end{pmatrix}. \quad (1.19)$$

$V_{\text{CKM}}$  measures the transition probability from  $q_u \rightarrow q_d$  due to the rotation of states of the down quark

$$\begin{pmatrix} d' \\ s' \\ b' \end{pmatrix} = \begin{pmatrix} V_{ud} & V_{cd} & V_{td} \\ V_{us} & V_{cs} & V_{ts} \\ V_{ub} & V_{cb} & V_{tb} \end{pmatrix} \begin{pmatrix} d \\ s \\ b \end{pmatrix}. \quad (1.20)$$

The CKM matrix is unitary, so precision tests of this unitary property can look at the sum

$$|V_{ud}|^2 + |V_{us}|^2 + |V_{ub}|^2 = 1 - \Delta, \quad (1.21)$$

where a nonzero  $\Delta$  would indicate deviation from unitarity. As we will show in the following chapter, neutron  $\beta$  decay gives important insight into unitarity as it can be used to measure the  $|V_{ud}|$  component [6].

### 1.3 The $\theta$ -term

While it has not been observed experimentally, there is nothing to stop us from writing a  $\theta$ -term that has  $F \wedge F$  dependence,

$$\mathcal{L}_\theta = \frac{\theta g^2}{8\pi^2} \text{tr } F \wedge F, \quad (1.22)$$

where in component form,

$$F \wedge F = \frac{1}{2}\epsilon_{\mu\nu\alpha\beta}F_{\mu\nu}F^{\alpha\beta}. \quad (1.23)$$

Experimentally, the parameter  $\theta$  is observed to be small. Note that we can also write  $F^2 = F \wedge \tilde{F}$ . For the  $\theta$ -term, we will have dependence on the dual term,

$$F \wedge F = dA \wedge dA + 2A \wedge A \wedge dA. \quad (1.24)$$

The  $\theta$ -term differs from the gauge field term in that it can be written as a total exterior derivative,

$$F \wedge F = dK, \quad (1.25)$$

where  $K$  is the Chern-Simons 3-form,

$$K = A \wedge dA + \frac{2}{3}A \wedge A \wedge A. \quad (1.26)$$

A useful property of the total exterior derivative is that we can use Stokes' Theorem to integrate  $dK$  on a 4-manifold  $M$  with boundary  $\partial M$  by integrating  $K$  on  $\partial M$ ,

$$\int_M \text{tr } F \wedge F = \int_{\partial M} \text{tr } K. \quad (1.27)$$

Let  $\partial M$  be a 3-cylinder with future time-slice three-disk,  $\mathbb{D}^3(t^+)$ , and past time-slice,  $\mathbb{D}^3(t^-)$ , as end-caps for times  $t^\pm \rightarrow \pm\infty$  and  $\mathbb{S}^2$  as the side. We can take the limit of  $r \rightarrow \infty$  of the 2-sphere,

$$\partial M = \mathbb{D}^3 \cup \mathbb{D}^3 \cup \mathbb{S}^2 \times \mathbb{R}. \quad (1.28)$$

In pictorial form this looks like

$$\partial M = \text{[Diagram of a cylinder with a dashed horizontal line through its center, representing the boundary of a 3D volume.]}. \quad (1.29)$$

The Chern-Simons action for level  $k$  can be written

$$S_{\text{CS}}^k(M) = \frac{k}{4\pi} \int_Y \text{tr } K. \quad (1.30)$$

$\tilde{K}$  is the Adler-Bell-Jackiw anomalous current [7–9]

$$\partial \tilde{K} = F \wedge F. \quad (1.31)$$

## 1.4 Neutron electric dipole moment

The neutron has a very small electric dipole moment (edm). In the Standard Model, it is estimated to be as small as  $d_n \approx 2 \times 10^{-32} e \text{ cm}$  by Khriplovich and Zhitnitsky [10].

A neutron edm can be generated by the QCD theta term [11] and is estimated by Pospelov to be [12]

$$d_n = (2.4 \times 10^{-16}) \bar{\theta} e \text{ cm}. \quad (1.32)$$

An experimental limit has most recently been set by the ILL at [13, 14]

$$|d_n| < 2.9 \times 10^{-26} e \text{ cm} \quad (90\% \text{ C.L.}). \quad (1.33)$$

This puts a limit on  $\bar{\theta}$  at

$$|\bar{\theta}| < 1.2 \times 10^{-10} \quad (90\% \text{ C.L.}). \quad (1.34)$$

## Chapter 2

# The Neutron

It is no good to try to stop knowledge from going forward. Ignorance is never better than knowledge.

---

ENRICO FERMI

### 2.1 Why Study the Neutron?

The neutron serves as a way of studying all four forces, the electroweak (the unification of electromagnetism and the weak force), strong and gravity. The neutron gives us a peek into the early universe as the free neutron made up half of all baryonic matter for the first three minutes. As we show, the neutron allows for searching for new forces and interactions beyond the Standard Model with relatively clean tests compared to complex nuclei. We will also show that the neutron has advantages even compared to high energy searches for new physics such as the Large Hadron Collider (LHC).

The neutron has a quark content of two valence down quarks and one valence up quark

$$|n\rangle = |udd\rangle. \quad (2.1)$$

This quark content is what gives the neutron its neutrality. As the neutron mass is slightly greater than the proton mass, it can decay via the weak force into a proton, an electron and an antielectron neutrino,

$$n \rightarrow p + e + \bar{\nu}_e. \quad (2.2)$$

As this decay is generated by the weak decay of a down quark into an up quark, the neutron

serves as a test of this interaction. Also, since the neutron is a complex baryon with internal QCD structure, the interaction is modified from the pure  $(V - A) \otimes (V - A)$  structure of the leptonic sector of the Standard Model, to reveal structure form factors in the interaction,

$$\mathcal{L}_\beta = \sqrt{8} G_F V_{ud} \bar{p} \gamma^\mu (g_V - g_A \gamma^5) n \bar{e} \gamma_\mu (1 - \gamma^5) \nu_e. \quad (2.3)$$

This gives us a metric by which to test lattice QCD calculations, which will likely be able predict the values  $g_A$  and  $g_V$  [15, 16]. Current experimental world average values for the vector and axial vector form factors have [17, 18]

$$g_V = 1.0000(3), \quad \lambda \equiv g_A/g_V = -1.2701(25). \quad (2.4)$$

## 2.2 Beta Decay

The  $\beta$ -decay process occurs both with free neutrons, and with neutrons bound inside the nucleus. In bound nuclear decay, the vector component of free neutron decay can be studied in Fermi  $0^+ \rightarrow 0^+$  decays. The nuclear structure can be ignored in favor of needing only to deal with the nucleon structure of the neutron and the final state proton instead. The axial vector component can be studied by pure Gamow-Teller decays or mixed decays such as the case with the neutron. As shown in figure 2.1, when a neutron decays, one of its valence

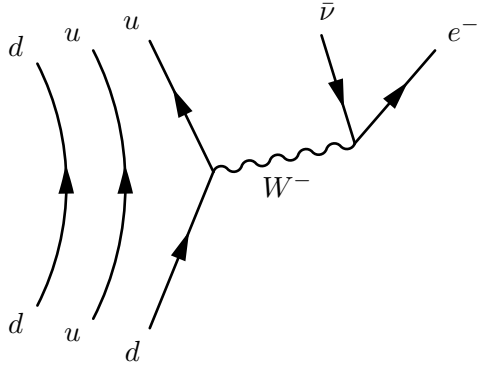


Figure 2.1. The Feynman diagram for neutron  $\beta$ -decay. The neutron, consisting of valence quark content  $|udd\rangle$ , decays into the proton which has valence content  $|udu\rangle$  by emitting an electron and an antineutrino via a  $W^-$  massive vector boson.

down quarks emits a massive  $W^-$  gauge boson. This then decays again into an electron, antineutrino pair. The lepton pair are QCD neutral, so they are both not bound inside

either the parent or daughter nucleon and can escape. However, the  $W^-$  is so massive and short-lived, that it never leaves the nucleon surface.

As mentioned in section 1.2, the quark mass eigenstates are not weak eigenstates. As a result, a  $u, d$  quark vertex has the CKM element  $V_{ud}$ . The diagram for this vertex is shown in figure 2.2.

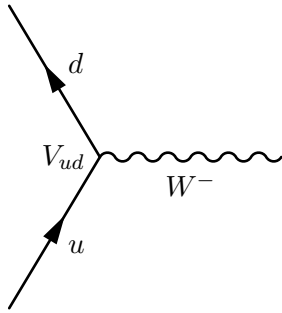


Figure 2.2. Weak interaction of the quarks with the mixing element of the CKM matrix, in this case  $V_{ud}$ .

### 2.2.1 Symmetries of the Four Fermion Interaction

The baryon structure of the neutron requires renormalization of the quark vertex. This is because the nuclear form factors  $g_A$  and  $g_V$  modify the underlying Standard Model vertex [19],  $\frac{1}{2} \bar{u}\gamma^\mu(1 - \gamma^5)d$ . Space-time symmetries of neutron beta decay only allow for vector, axial vector, scalar, and tensor (VAST) interactions. Potentially, any of these may have coupling constants and form factors modifying the associated vertex. The VAST form factors are defined in terms of the initial  $n$  state and final  $p$  states along with the Fermi and Gamow-Teller matrix elements,  $\mathcal{M}_F$  and  $\mathcal{M}_{GT}$  [20],

$$\begin{aligned} \langle p | \bar{u}\gamma^\mu d + \text{h.c.} | n \rangle &= g_V \mathcal{M}_F, \\ \langle p | \bar{u}\gamma^\mu \gamma_5 d + \text{h.c.} | n \rangle &= g_A \mathcal{M}_{GT}, \\ \langle p | \bar{u}d + \text{h.c.} | n \rangle &= g_S \mathcal{M}_F, \\ \langle p | \bar{u}\sigma^{\mu\nu} d + \text{h.c.} | n \rangle &= g_T \mathcal{M}_{GT}. \end{aligned} \tag{2.5}$$

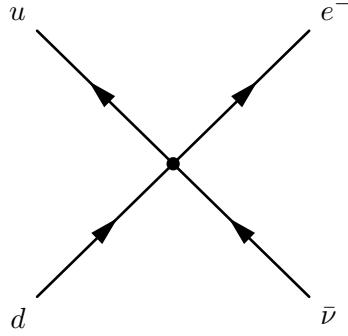


Figure 2.3. The Feynman diagram for neutron four-fermion interaction showing the effective point vertex for any physics. By Lorentz invariance, only the VAST terms are allowed at the vertex. The pseudoscalar term is suppressed.

The conserved vector current hypothesis of the Standard Model implies that  $g_V = 1$  up to  $\mathcal{O}(10^{-4})$  isospin breaking corrections [21]. It may seem as if we should have a pseudoscalar interaction,

$$\langle p | \bar{u} \gamma_5 d + \text{h.c.} | n \rangle = g_P \mathcal{M}_{\text{GT}}. \quad (2.6)$$

However, this is known to be suppressed in the Standard Model from the branching ratio of  $\pi^+$  decay,

$$\frac{\Gamma(\pi^+ \rightarrow e^+ + \nu_e)}{\Gamma(\pi^+ \rightarrow \mu^+ + \mu_\mu)} = \left( \frac{m_e}{m_\mu} \right)^2 \left( \frac{1 - m_e^2/m_\pi^2}{1 - m_\mu^2/m_\pi^2} \right)^2 \approx 10^{-4}. \quad (2.7)$$

## 2.3 Vector and Axial Vector Currents

The Conserved Vector Current (CVC) hypothesis states that  $g_V = 1$  exactly. This enforces conservation of charge. Assuming CVC to be the case, it is only necessary to use one parameter,  $\lambda = g_A/g_V$ , to parameterize the effective Lagrangian. As shown in figure 2.5, the vertex can be potentially renormalized via the strong force with strongly interacting pions [19]. CVC implies that this renormalization procedure leaves the “weak charge” unchanged. This is similar to the renormalization procedure in QED where each particle in the sum of diagrams has the same charge, thus the charge itself remains intact, thus charge is conserved.

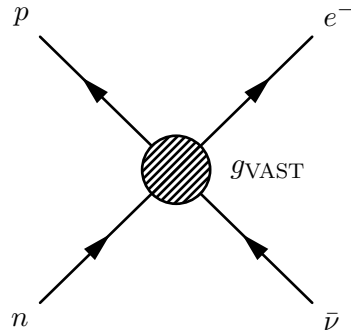


Figure 2.4. The Feynman diagram for effective neutron  $\beta$ -decay. The interaction at the four-fermion vertex contains form factors  $g_{\text{VAST}}$  from the QCD contributions to the nuclear structure that modify the pure  $(V - A) \otimes (V - A)$ .

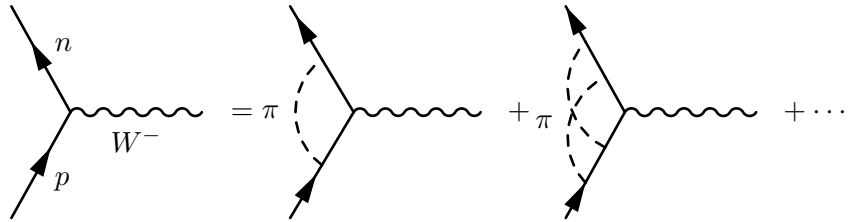


Figure 2.5. Strong renormalization of  $g_V$  leaving charge current conserved.

This is not the case for axial vector currents. While  $g_A \approx 1.27$  is close to one, it is not exactly one, as in the case of the CVC hypothesis. Axial vector current is only partially conserved.

### 2.3.1 The Neutron $\beta$ Decay Spectrum

The  $\beta$  decay spectrum has the differential form

$$\frac{d^2\Gamma}{dE d\Omega} = \frac{G_F^2}{2\pi^3} |V_{ud}|^2 (g_V^2 \mathcal{M}_F^2 + g_A^2 \mathcal{M}_{GT}^2) \mathcal{W}(E). \quad (2.8)$$

The phase space factor is given by

$$\mathcal{W}(E) = F(Z, E) p^2 (E_0 - E)^2 (1 + \Delta_{\text{RC}} + \Delta_{\text{recoil}}), \quad (2.9)$$

where  $E$  is the energy of the emitted  $\beta^\pm$ ,  $p$  is the momentum and  $E_0$  is the end point. We also have QCD and electroweak radiative corrections in  $\Delta_{\text{RC}}$ , and recoil order corrections due to the finite mass of the proton accounted for in  $\Delta_{\text{recoil}}$ . A plot of  $\mathcal{W}(E)$  is shown in figure 2.6. For general  $\beta$  decay of a nucleus with charge  $Z$  we have [22]

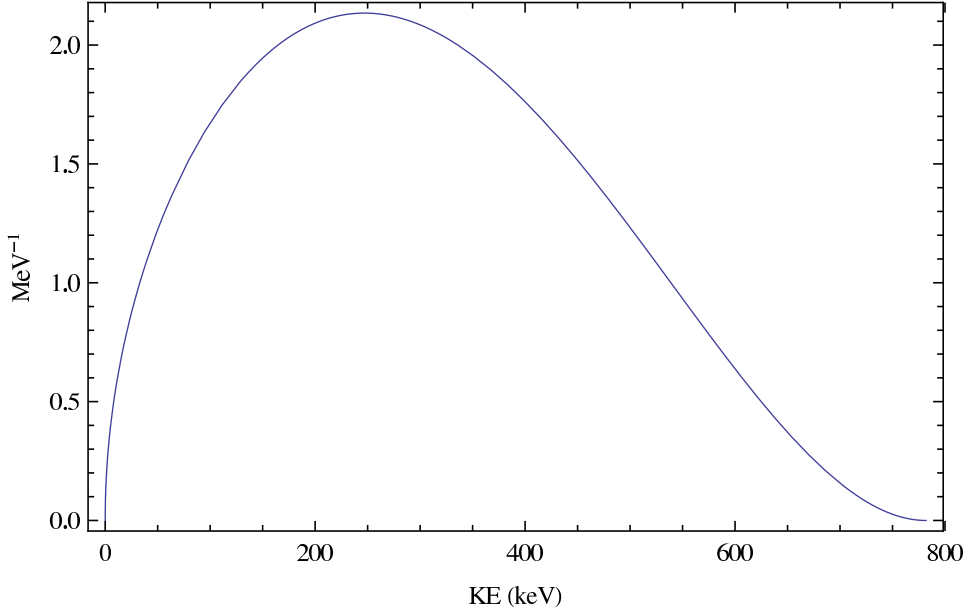


Figure 2.6. An ideal beta decay spectrum of the neutron.

$$F(Z, E) = \frac{2(1 + \gamma)}{\Gamma(1 + 2\gamma)} (2p\rho)^{2\gamma-2} e^{\pi\eta} |\Gamma(\gamma + i\eta)|^2, \quad (2.10)$$

where

$$\gamma = \sqrt{1 - \alpha^2 Z^2}, \quad (2.11)$$

and

$$\eta = \pm \alpha Z E, \quad (2.12)$$

for  $\beta^\mp$  decay, and  $\rho = r_N/\hbar$  for the final state nuclear radius. For the neutron, with  $Z = 1$  for the final state, this simplifies to

$$F(Z, E) \approx \frac{x}{1 - e^{-x}}, \quad (2.13)$$

where  $x \equiv \mp 2\pi\alpha Z c/v$  [23].

### 2.3.2 Alphabet Soup

The full form of the neutron spectrum has been parameterized with an “alphabet soup” of letters for each correlation coefficient of spin and momenta combinations of the parent and daughters [24, 25],

$$\frac{d^2\Gamma}{dE_e d\Omega_e d\Omega_\nu} \propto \mathcal{W}(E_e) \left[ 1 + a \frac{\vec{p}_e \cdot \vec{p}_\nu}{E_e E_\nu} + b \frac{m_e}{E_e} + A \frac{\vec{p}_e \cdot \vec{J}_n}{E_e} + B \frac{\vec{p}_\nu \cdot \vec{J}_n}{E_\nu} + D \frac{\vec{p}_e \times \vec{p}_\nu \cdot \vec{J}_n}{E_e E_\nu} + \dots \right]. \quad (2.14)$$

Terms in  $\vec{J}_e$  are not shown. The coefficients in (2.14) can be approximated at leading order by [15]

$$\begin{aligned} a_0 &= \frac{1 - \lambda^2}{1 + 3\lambda^2}, \\ A_0 &= -\frac{2\lambda(1 + \lambda)}{1 + 3\lambda^2}, \\ B_0 &= -\frac{2\lambda(1 - \lambda)}{1 + 3\lambda^2}, \\ b &= 0. \end{aligned} \quad (2.15)$$

Together, these give the dependent relations [26]

$$\begin{aligned} a_0 - A_0 + B_0 &= 1, \\ a_0 B_0 &= A_0(A_0 + 1). \end{aligned} \quad (2.16)$$

Measurements of  $A$  have recently been made using the Perkeo and UCNA experiments. Experiments by Perkeo II, UCNA, and Perkeo III have successfully reduced total corrections to the raw data down to the percent level [27]. The Perkeo III instrument uses a polarized cold neutron beam, unlike UCNA which uses ultracold neutrons. UCNA will be discussed in detail in chapter 7.

### 2.3.3 The Neutron Lifetime

Integrating equation (2.8) over energy and angle the Standard Model neutron lifetime is given by

$$\tau_n^{-1} = \frac{G_F^2}{2\pi^3} (1 + 3\lambda^2) |V_{ud}|^2 m_e^5 I_0(1 + \Delta), \quad (2.17)$$

where  $I_0$  is the zero moment of the phase space integral for neutron decay [28, 29]

$$I_k = \int_1^{x_0} x^{1-k} (x - \delta)^2 \sqrt{x^2 - 1} dx \quad (2.18)$$

integrated up to the reduced relativistic end point  $x_0 = E_0/m_e$  where  $E_0$  is the neutron beta decay end point. Also here,  $\Delta$  encapsulates radiative or recoil order corrections in this formula. Note that we have

$$\left\langle \frac{m_e}{E_e} \right\rangle = \frac{I_1}{I_0} \approx 0.652. \quad (2.19)$$

Experimentally, the current PDG world average value for the neutron lifetime is [17],

$$\tau_n = 880.1 \pm 1.1 \text{ sec.} \quad (2.20)$$

Using this value and  $\lambda$ , we can also extract  $V_{ud}$ ,

$$|V_{ud}|^2 = \frac{4908.7(1.9) \text{ sec.}}{\tau_n(1 + 3\lambda^2)}. \quad (2.21)$$

The current PDG value for  $V_{ud}$  is given by [30]

$$V_{ud} = 0.97425(22). \quad (2.22)$$

This value is extracted from superallowed decay  $ft$  values, using the half-lives,  $t$ , and phase space integrals, including the Fermi function, recoil, finite nuclear size, all of which give the nucleus dependent  $f$ .

$$|V_{ud}|^2 = \frac{2984.48(5) \text{ sec.}}{(1 + \Delta_{RC}) \langle \mathcal{F}t \rangle}, \quad (2.23)$$

where  $\Delta_{RC} = 0.02361(38)$  are nucleus-independent radiative corrections [30]. After accounting for transition-dependent and transition-independent radiative corrections and averaging over many superallowed nuclear decays [30]

$$\langle \mathcal{F}t \rangle = 3071.81 \pm 0.79_{\text{stat}} \pm 0.27_{\text{sys}} \text{ sec,} \quad (2.24)$$

where  $\mathcal{F}t$  is the corrected  $ft$  value after accounting for radiative effects such as bremsstrahlung photon emission.

### 2.3.3.1 The Lifetime Problem

The neutron lifetime, experimentally, has been a bit of a problem. Over the years since it was first measured, it has shortened. Of recent concern in particular, a measurement published in 2005 by Serebrov et al. [31] had a value of

$$\tau_n = 878.5 \pm 0.7 \pm 0.3 \text{ sec.} \quad (2.25)$$

This caused the PDG world average value to change from  $885.7 \pm 0.8$  sec in 2010 down to the present value of

$$\tau_n = 880.1 \pm 1.1 \text{ sec} \quad (2.26)$$

as they did not include Serebrov's measurement in their average until 2012.

As a result of this  $6\sigma$  discrepancy, the PDG called for the neutron community to make new measurements of the neutron lifetime. Accordingly, many new experiments have been planned or are underway. One such experiment uses a Gravito-magnetic trap planned at LANSCE using permanent magnets [32–35]. This trap is designed to have highly chaotic orbits by introducing an asymmetry into the trap design [32,33]. The trap is a bowl formed by two toroids of differing inner radii placed together obliquely.

## 2.4 Ultracold Neutrons

The neutron was first discovered in 1932 as a neutral particle with roughly the same mass as the hydrogen atom, but with an unprecedented ability to penetrate deep into matter. First proposed in 1920 by Ernest Rutherford as a component of the nucleus, before its actual discovery, no subatomic particle was known to evade entrapment quite like the neutron. It came as a great surprise then, when Ya. B. Zel'dovich proposed in 1959 [36,37] that neutrons could, in fact, be totally internally trapped by very thin coatings of materials on storage bottle walls, orders of magnitude thinner than the shielding thermal neutrons required to be stopped. The secret sauce was that these neutrons must be ultracold, possessing energies of only a few hundred nanoelectronvolts.

Ultracold neutrons were actually first proposed and experimentally shown by Enrico Fermi in 1946 [38] as a neutron that could be reflected off a thin surface. But it was only later that the prediction that UCN could be stored was made [37].

### 2.4.1 The Fermi Potential

The Fermi potential can be expressed as a sum of delta functions visible to the neutron wave packet when the wavelength is much larger than the atomic spacing of a material,

$$V_F = \frac{2\pi\hbar^2}{m_n} \sum_i b_i \delta(\mathbf{r} - \mathbf{r}_i). \quad (2.27)$$

Here, the  $b_i$  are the coherent neutron scattering lengths of the constituent nuclei. The delta functions sum to give an average scattering length for a material  $b$ ,

$$V_F = \frac{2\pi\hbar^2}{m_n} bn \quad (2.28)$$

where  $n$  is the number density of those nuclei. The Fermi potentials,  $V_F$ , of some common building materials used in UCN experiments are shown in table 2.1. For H and D, the density can vary depending on the material so the potential is not typically well defined but they do have opposite sign.

Table 2.1. Fermi potentials of common building materials

element	$b$ (fm)	$V_F$ (neV)
<sup>58</sup> Ni	14.4	335
Ni	10.3	252
Be	7.75	252
Fe	9.7	210
Cu	7.6	168
Al	3.45	54
H	-3.74	< 0
D	+6.67	> 0

### 2.4.2 Magnetic Fields

For a neutron with spin vector  $\vec{\sigma}$ , there is a potential induced by the magnetic moment of the neutron,  $\mu_n$ , and interaction with an external magnetic field,  $\vec{B}$ , given by

$$V_B = \mu_n \vec{\sigma} \cdot \vec{B}. \quad (2.29)$$

Since a neutron is a spin-1/2 particle, the spin can only be projected onto an axis where the spin is either aligned or antialigned with the field along that axis. This gives us a simple two-valued potential

$$V_B = \pm \mu_n B. \quad (2.30)$$

The magnetic moment can be conveniently expressed in “UCN units,”

$$\mu_n = -60.307\ 739(14) \text{ neV/T}. \quad (2.31)$$

This tells us that UCN of all energies up to the Fermi potential of  $^{58}\text{Ni}$  can be polarized and even trapped by a 6 T field. The trapping or conversely the repulsion of UCN from a field gradient is dependent on the spin states. The neutrons with spin antialigned state with the field are typically called the high-field seekers. Those that are in the aligned state are typically called the low-field seekers. High-field seekers gain energy by a field and so they can escape magnetic valleys. Low-field seekers are completely trapped. Many UCN experiments are designed to use this property.

### 2.4.3 The Gravitational Potential

Ultracold neutrons move so slowly that gravitational interactions cannot be ignored. Like the magnetic moment, the mass of the neutron can be represented in UCN units,

$$m_n = -10.454\ 074\ 7(23) \text{ neV s}^2 \text{ m}^{-2}, \quad (2.32)$$

such that at sea level, we have a potential per height [17],

$$m_n g = 1.025\ 19 \text{ neV/cm}. \quad (2.33)$$

UCN can be completely trapped by a “bowl” only 3.4 m deep. The LANL neutron lifetime experiment, UCN $\tau$ , uses low-field UCN and gravity to trap UCN in an essentially lossless bottle where UCN never touch the walls [33–35].

## Chapter 3

# The Neutron Beyond the Standard Model

### 3.1 Beyond V – A

The electroweak sector of the Standard Model so far has a well explored  $(V - A) \otimes (V - A)$  structure. Only vector and axial vector interactions have been observed and thus any deviation would be strong evidence for physics beyond the Standard Model. In this chapter, we explore how new physics would affect the beta decay of the neutron. In particular, we look at how new scalar and tensor interactions would affect the beta decay effective vertex. Fermi beta decays allow us to study new S and V interactions, and Gamow-Teller beta decays allow us to study A and T interactions. The neutron is a mix of both decays, so it has the ability to give us insight into both.

We showed in chapter 2 that for the neutron, the  $V - A$  coupling is complicated by the form factors  $g_A$  and  $g_V$ . The value of  $g_A$  has been measured to higher precision than the theoretical value has been derived. This makes it difficult to look for new physics by measuring  $V - A$  couplings alone. While this also is the case for  $g_S$  and  $g_T$  inside the nucleon, the scalar and tensor couplings are zero, so any nonvanishing scalar and tensor interactions serve as a good indicator of new physics.

In this chapter we will look at the general theory of beta decay beyond the Standard Model. We will examine a few theories, namely Supersymmetry and the theory of leptosquarks, and apply those to beta decay. Most relevant to this thesis, we will see how such theories would affect the Fierz interference term.

### 3.1.1 General Effective Lagrangian

The most general Lorentz invariant effective Lagrangian for beta decay is given by a four point contact term,

$$\mathcal{L}_\beta = -\sqrt{8} G_F^\mu a_{ij}^I \bar{e}_i \Gamma^I \nu_e \bar{u} \Gamma_I d_j, \quad (3.1)$$

where  $G_F^\mu$  is  $G_F$ , the Fermi constant, as extracted from the  $\mu$  decay vertex [20, 39]. There are two bilinear terms; one for the quark content and one for the lepton content. The generalized vertex elements have the four-fermion symmetries imposed by Lorentz invariance. As discussed in chapter 2, the only interactions possible are the generalized Dirac matrices,

$$\Gamma^S = 1, \quad \Gamma_\mu^V = \gamma_\mu, \quad \text{and} \quad \Gamma_{\mu\nu}^T = \sqrt{\frac{1}{2}} \sigma_{\mu\nu}. \quad (3.2)$$

The  $a_{ij}^I$  are the coupling constants for each Dirac matrix type and chirality  $i, j \in L, R$ . In the Standard Model, with its pure  $(V - A) \otimes (V - A)$  structure in the weak sector, only vector  $LL$  couplings survive, leaving only the CKM matrix element,

$$a_{LL}^V = V_{ud}(1 + \Delta_\beta - \Delta_\mu), \quad (3.3)$$

where  $\Delta_\beta$  is the radiative corrections to  $\beta$ -decay extraction of  $V_{ud}$ , and  $\Delta_\mu$  is the radiative corrections to the extraction of  $G_{F(\mu)}$  [20]. All other couplings vanish,

$$a_{ij}^I = 0, \quad (3.4)$$

so that any theory in which these couplings are nonzero will produce the possibility for a test of that theory in the  $\beta$ -decay of neutrons.

## 3.2 Fierz Interference

In this section, we discuss the theoretical heart of this thesis, the effect of Fierz interference on the beta decay energy spectrum of electrons emitted from neutron decay. The Fierz term is not something that should occur in the Standard Model, at least not in the center-of-mass energy spectrum. In the electron spectrum, in the lab frame, a nonzero Fierz term shows up at recoil order due to the finite mass of the proton. The term is small,  $\approx 10^{-3}$ , and the correction, calculable. When viewed in terms of a multiplier on the standard phase space

distribution as given in 2.18, this recoil order correction to  $b$  is

$$b^{\text{recoil}} = -\frac{m_e}{m_n} \frac{1 + \mu_V \lambda + \lambda^2}{1 + 3\lambda^2}. \quad (3.5)$$

This gives  $b_{\text{recoil}} = -1.35(1) \times 10^{-3}$  [15]. Any deviation from this nonzero factor in the lab frame is an indication that there are scalar or tensor interactions from physics beyond the Standard Model.

Of all the letters in the  $\beta$ -decay alphabet soup given by equation (2.14), only the Fierz interference term,  $b$ , survives integration over all polarization and momenta.

$$d\Gamma_b(E_e) = \left(1 + b \frac{m_e}{E_e}\right) d\Gamma_{\text{SM}}(E_e) \quad (3.6)$$

This term modifies the neutron lifetime, as can be seen by integrating over the electron energy,

$$\tau_n^{-1} = \int \left(1 + b \frac{m_e}{E_e}\right) d\Gamma_{\text{SM}}. \quad (3.7)$$

This gives us a ratio of lifetimes for the Fierz term compared to the predicted lifetime from the Standard Model,

$$\frac{\tau_n}{\tau_n^{\text{SM}}} = \frac{1}{1 + b \langle \frac{m_e}{E} \rangle}. \quad (3.8)$$

### 3.2.1 The Standard Model Fierz Interference Term

The Fierz interference term is very small in the Standard Model. This is because there are no scalar or tensor couplings present and  $b_n$  is dependent on combinations of these couplings.

Contribution to the center-of-mass Fierz term in the Standard Model are highly suppressed. In what we believe to be the largest contribution to the Fierz, we can construct a one-loop effective vertex involving the  $W$  and the Higgs boson. The effective vertex involves both the exchange of flavor changing  $W^-$  and flavor neutral Standard Model Higgs. The Higgs contributes to the scalar component that gives nonzero  $b$ . This contribution is small however, primarily due to the Yukawa coupling terms introduced by the Higgs coupling to the electron and quark content. In figure 3.1(a) we have the  $t$ -channel, which has a flavor changing  $W$  and then an exchange of a Higgs. In figure 3.1(b) we have the  $u$ -channel, which has a flavor changing  $W$  crossed with the Higgs. These two diagrams give us an effective

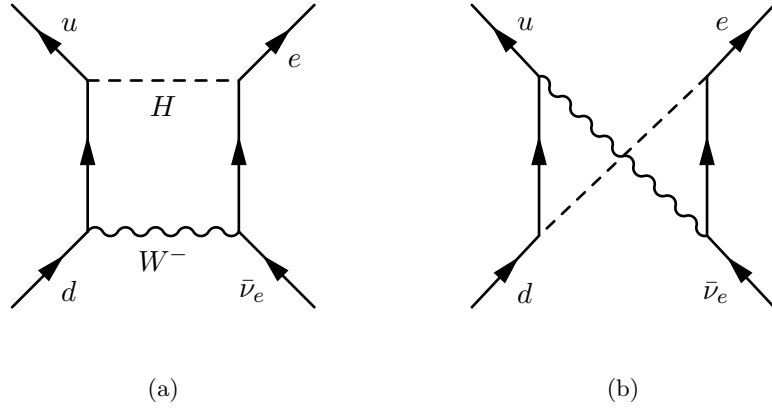


Figure 3.1. The two Feynman diagrams for the one-loop contributions from the Standard Model to the effective  $\beta$  decay vertex.

vertex that is roughly on the order of

$$\frac{m_e m_u}{M_W^2} + \frac{m_e m_d}{M_W^2} = \mathcal{O}(10^{-9}). \quad (3.9)$$

Because of the low mass of the neutrino, and therefore suppressed Yukawa coupling, the two diagrams with the Higgs connecting the  $\nu$  are neglected.

### 3.2.2 Spectral Effects of Fierz Interference

The Fierz term has the effect of shifting the neutron beta spectrum. If we have a probability distribution function,

$$P(E) = \tau_n \Gamma(E), \quad (3.10)$$

then the Fierz term shifts the probability spectrum by

$$P_b(E) dE = \frac{1 + bx^{-1}}{1 + b \langle x^{-1} \rangle} P_{\text{SM}}(E) dE. \quad (3.11)$$

where  $x \equiv E/m_e$ . This can be approximated, for small  $b$  as

$$P_b(E) dE = \left[ 1 + b \left( \frac{m_e}{E} - \left\langle \frac{m_e}{E} \right\rangle \right) + \mathcal{O}(b^2) \right] P_{\text{SM}}(E) dE. \quad (3.12)$$

Here  $\langle x^{-1} \rangle = \langle m_e/E \rangle$  is the expected value of  $m_e/E$  over the full energy range of  $P_{\text{SM}}$ . A plot of a family of spectral curves for different values of  $b$  are shown in figure 3.2. The

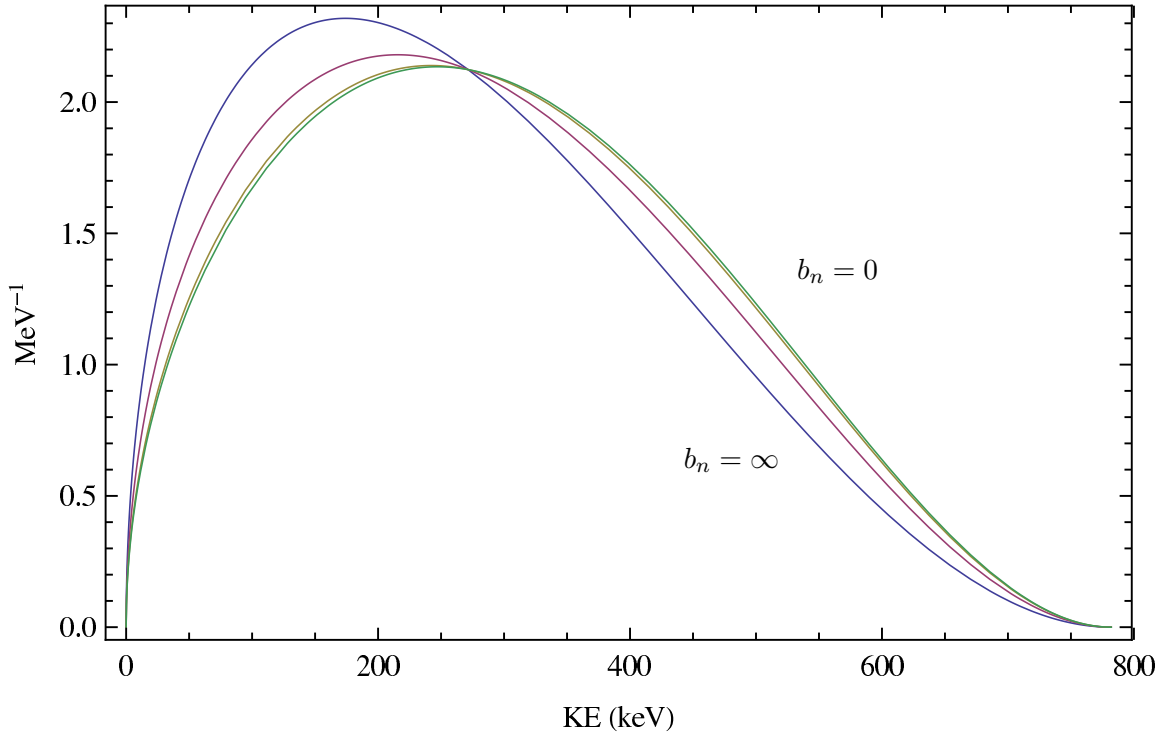


Figure 3.2. The neutron spectrum probability function under the effect of the Fierz interference term. Here is shown from left to right  $\lim b_n \rightarrow \infty$ ,  $b_n = 1$ ,  $b_n = 0.1$  and  $b_n = 0$ . A realistic Fierz term of  $b_n < 10^{-3}$  would not be visible on the plot.

spectral effect of  $b_n$  is most visible in the Fierz ratio,  $R_F$ , the ratio of the non-Standard Model spectrum containing  $b_n$ ,  $P_b$ , to the  $b_n = 0$  Standard Model spectrum,  $P_{SM}$ ,

$$R_F = \frac{P_b}{P_{SM}} = \frac{1 + b_n \frac{m_e}{E}}{1 + b \langle \frac{m_e}{E} \rangle}. \quad (3.13)$$

A plot of example Fierz ratios are shown in figure 3.3.

### 3.2.3 The Fermi and Gamow-Teller Combination

Using the contact Lagrangian in equation (3.1), we are able to write  $b$  in terms of all possible scalar and tensor couplings [20],

$$b = \pm \frac{2 \operatorname{Re} [\mathcal{M}_F^2 g_V g_S a_{LL}^V (a_{RL}^S + a_{RR}^S)^* - 2 \mathcal{M}_{GT}^2 g_A g_T a_{LL}^V a_{RL}^{T*}]}{\mathcal{M}_F^2 (g_V^2 |a_{LL}^V|^2 + g_S^2 |a_{RL}^S + a_{RR}^S|^2) + \mathcal{M}_{GT}^2 (g_A^2 |a_{LL}^V|^2 + 4 g_T^2 |a_{RL}^T|^2)}. \quad (3.14)$$

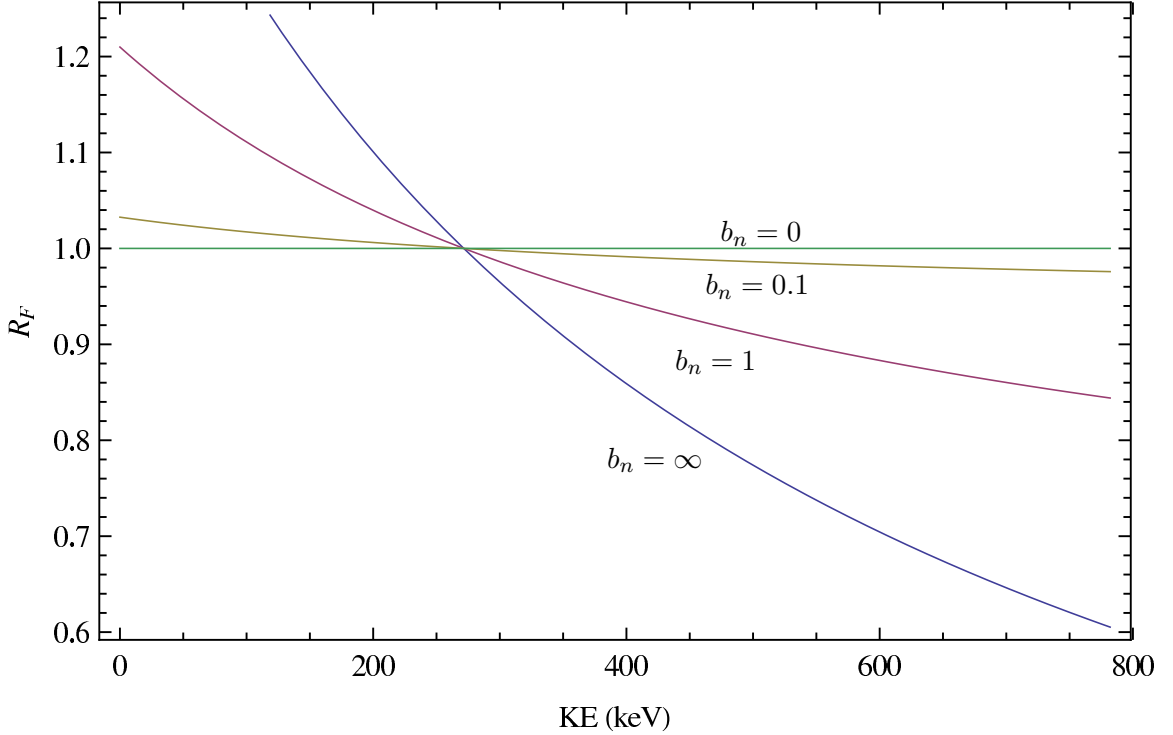


Figure 3.3. The Fierz ratio,  $R_F$ , shown for different values of  $b$ . Here is shown from top to bottom  $\lim b_n \rightarrow \infty$  (blue),  $b_n = 1$  (red),  $b_n = 0.1$  (yellow) and  $b_n = 0$  (green).

As the couplings other than  $a_{LL}^V \approx V_{ud}$  are known to be small, the general exact expression simplifies to

$$b = \pm \frac{2 \operatorname{Re} [\mathcal{M}_F^2 g_V g_S (a_{RL}^S + a_{RR}^S)^* - 2 \mathcal{M}_{GT}^2 g_A g_{GT} a_{RL}^{T*}]}{V_{ud} (\mathcal{M}_F^2 g_V^2 + \mathcal{M}_{GT}^2 g_A^2)}. \quad (3.15)$$

From equation (3.15) we can reduce the neutron component into two parts. The first part is the pure Fermi component,

$$b_F = 2 \frac{g_S}{g_V} \frac{a_{RL}^S + a_{RR}^S}{a_{LL}^V}. \quad (3.16)$$

The second part is the Gamow-Teller component,

$$b_{GT} = -4 \frac{g_T}{g_A} \frac{a_{RL}^T}{a_{LL}^V}. \quad (3.17)$$

Note that if

$$-a_{RL}^S \approx a_{RR}^S \gg 0, \quad (3.18)$$

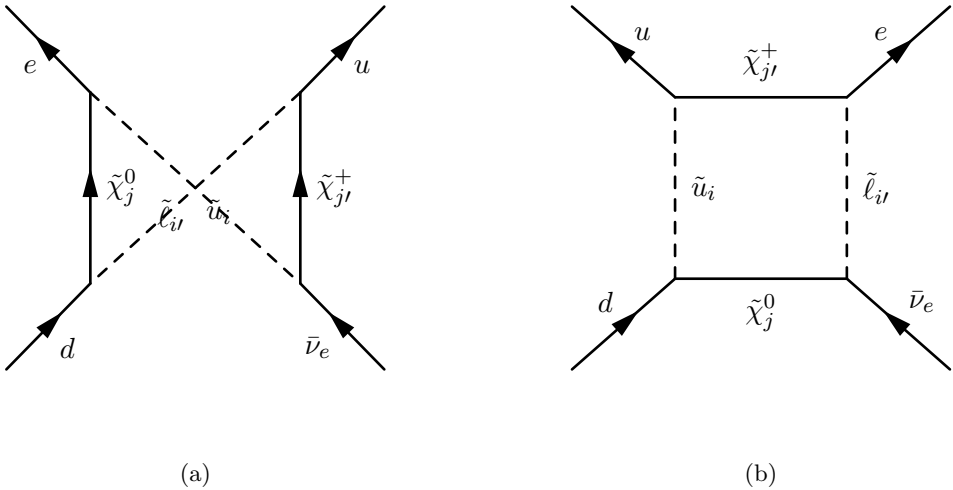


Figure 3.4. The two Feynman diagrams for the one-loop contributions from MSSM to the effective  $\beta$  decay vertex.

we have a condition whereby  $b_F$  may be small while  $b_{GT}$  is not. The linear combination of both the Fermi and Gamow-Teller components simplifies to the Fierz term for the neutron,

$$b_n = \frac{b_F + 3\lambda^2 b_{\text{GT}}}{1 + 3\lambda^2}. \quad (3.19)$$

### 3.3 Supersymmetry

### 3.3.1 Minimal Supersymmetric Standard Model

One of the most popular models for physics beyond the Standard Model, is Supersymmetry (SUSY), specifically the Minimal Supersymmetric Standard Model (MSSM). Now that the Higgs boson has been discovered with a mass of 125 GeV [40, 41], there is likely room for MSSM, or at least NMSSM. MSSM adds sfermions, superpartners of the fermions that allow for right-left mixing with the light quarks. MSSM also adds the neutrinolinos and charginos, the lightest superpartners of the gauge boson content of the Standard Model. Together, these form box diagrams that have an effective beta decay vertex. In Profumo [20], they arrive at some unusual conditions where MSSM may produce a  $b_n$  for the neutron as large

as  $10^{-3}$ . To do so, we must first look at the sfermion mass matrix;

$$\mathbf{M}_{\tilde{f}}^2 = \begin{pmatrix} \mathbf{M}_{\text{LL}}^2 & \mathbf{M}_{\text{LR}}^2 \\ \mathbf{M}_{\text{RL}}^2 & \mathbf{M}_{\text{RR}}^2 \end{pmatrix}, \quad (3.20)$$

where each block is a  $3 \times 3$  mixing block over the three flavors of fermions of a given chiral multiplet. After electroweak symmetry breaking, these take the form

$$\mathbf{M}_{\text{LL}}^2 = \mathbf{m}_Q^2 + \mathbf{m}_q^2 + \left( I_3^f - Q_f \sin^2 \theta_W \right) \cos 2\beta M_Z^2, \quad (3.21)$$

and

$$\mathbf{M}_{\text{RR}}^2 = \mathbf{m}_{\tilde{f}}^2 + \mathbf{m}_q^2 + Q_f \sin^2 \theta_W \cos 2\beta M_Z^2. \quad (3.22)$$

For  $\tilde{u}$ , sup type, we have

$$\mathbf{M}_{\text{LR}}^2 = \mathbf{M}_{\text{RL}}^2 = v (\mathbf{a}_f \sin \beta - \mu \mathbf{Y}_f \cos \beta), \quad (3.23)$$

and for  $\tilde{d}$ , sdown type, we have

$$\mathbf{M}_{\text{LR}}^2 = \mathbf{M}_{\text{RL}}^2 = v (\mathbf{a}_f \cos \beta - \mu \mathbf{Y}_f \sin \beta). \quad (3.24)$$

For the cases that diagonalize  $\mathbf{M}_{\text{LR}}^2$ , we have the mass matrices  $\mathbf{m}_Q^2$ ,  $\mathbf{m}_q^2$ ,  $\mathbf{m}_{\tilde{f}}^2$  for the LH squarks, the quarks and RH squarks, respectively. The model diverges from the standard assumptions about the  $3 \times 3$  Yukawa  $\mathbf{a}_f$  and soft triscalar couplings  $\mathbf{Y}_f$ . Traditionally, these are proportional

$$\mathbf{a}_f \propto \mathbf{Y}_f. \quad (3.25)$$

This assumption would suppress the Fierz term. Without it however, Fierz terms of order  $10^{-3}$  are possible.

Let  $\mathbf{Z}_f$  diagonalize  $\mathbf{M}_{\tilde{f}}^2$ . The sfermion mass eigenstates,  $\tilde{F}_j$ , are given by

$$\tilde{F}_j = Z_f^{jI} \tilde{f}_I, \quad (3.26)$$

where  $\tilde{f}_{1,2,3}$  are the LH flavor states and  $\tilde{f}_{4,5,6}$  are the RH flavor states.

In MSSM, the neutrolinos mix to give

$$\chi_i^0 = N_{ij} \psi_j^0. \quad (3.27)$$

Finally, the charginos are the mixes of the Winos and Higginos

$$\begin{pmatrix} \chi_1^+ \\ \chi_1^- \end{pmatrix} = \mathbf{V} \begin{pmatrix} \tilde{W}^+ \\ \tilde{H}_u^+ \end{pmatrix}, \quad (3.28)$$

and

$$\begin{pmatrix} \chi_1^- \\ \chi_1^+ \end{pmatrix} = \mathbf{U} \begin{pmatrix} \tilde{W}^- \\ \tilde{H}_d^- \end{pmatrix}. \quad (3.29)$$

The diagrams compute to give Fierz terms of

$$b_F = \frac{2\alpha}{3\pi} \frac{g_S}{g_V} M_Z^2 (\delta_1 - \delta_2), \quad (3.30)$$

and

$$b_{GT} = \frac{2\alpha}{3\pi} \frac{g_T}{g_A} M_Z^2 \delta_2, \quad (3.31)$$

where

$$\delta_1 = |U_{k1}|^2 Z_D^{1i*} Z_D^{4i} Z_L^{1m} Z_L^{4m*} |N_{j1}|^2 \mathcal{F}_1 \left( M_{\chi_j^0}, M_{\chi_k^+}, M_{\tilde{d}_i}, M_{\tilde{\ell}_m} \right), \quad (3.32)$$

and

$$\delta_2 = U_{j1} V_{j1}^* Z_U^{1i*} Z_U^{4i} Z_L^{1m} Z_L^{4m*} |N_{k1}|^2 M_{\chi_j^+} M_{\chi_k^0} \mathcal{F}_1 \left( M_{\chi_j^+}, M_{\chi_k^0}, M_{\tilde{u}_i}, M_{\tilde{\ell}_m} \right). \quad (3.33)$$

Here we are using the Profumo defined loop integral [20],

$$\begin{aligned} & \mathcal{F}_n(m_a, m_b, m_c, m_d) \\ & \equiv \int_0^1 dx \int_0^{1-x} dy \int_0^{1-x-y} dz \left[ xm_a^2 + ym_b^2 + zm_c^2 + (1-x-y-z)m_d^2 \right]^{-n}. \end{aligned} \quad (3.34)$$

### 3.3.2 Next-to-Minimal Supersymmetric Standard Model

The Next-to-Minimal Supersymmetric Standard Model (NMSSM) introduces a chiral superfield,  $S$ , by modifying the super potential with

$$\Delta W = \lambda S H_u H_d + \frac{1}{3} \kappa S^3, \quad (3.35)$$

which mixes with the MSSM Higgsinos and gauginos [42],

$$\tilde{\chi}_{1,2,3,4,5}^0 = \left( i\tilde{B}, -i\tilde{W}^0, \tilde{H}_u^0, \tilde{H}_d^0, \tilde{S} \right). \quad (3.36)$$

This alters the phenomenology of the Higgs and neutrolino sector. However, since this has minimal effect on the mass of neutrolinos, this mixing should not significantly alter the order of magnitude of the SUSY contribution to the Fierz interference term either [43].

## 3.4 Leptoquarks

While possible SUSY contributions to the neutron decay vertex are motivating, the extreme assumptions needed pose a likelihood problem. Further, even if these conditions are met, the SUSY sector only enters at the one-loop level. Instead, we should consider theories that contribute at tree level. Models that involve leptoquarks are good candidates for generating scalar interaction in the low energy sector.

### 3.4.1 Leptoquark Contributions to Fierz Interference

As described in [44–46], we have the following general Lagrangian for the scalar component

$$\begin{aligned} \mathcal{L}_{\text{LQ}}^S &= \lambda_{S_0}^R \cdot \bar{u}^c e_R \cdot S_0^{R\dagger} + \lambda_{\tilde{S}_0}^R \cdot \bar{d}^c e_R \cdot \tilde{S}_0^\dagger \\ &+ \lambda_{S_{1/2}}^R \cdot \bar{u}\ell_L \cdot S_{1/2}^{R\dagger} + \lambda_{\tilde{S}_{1/2}}^R \cdot \bar{d}\ell_L \cdot \tilde{S}_{1/2}^\dagger \\ &+ \lambda_{S_0}^L \cdot \bar{q}^c i\tau_2 \ell_L \cdot S_0^{L\dagger} + \lambda_{S_{1/2}}^L \cdot \bar{q} i\tau_2 e_R \cdot S_{1/2}^{L\dagger} \\ &+ \lambda_{\tilde{S}_1}^L \cdot \bar{q}^c i\tau_2 \ell_L \cdot \tilde{S}_1^\dagger + \text{h.c.} \end{aligned} \quad (3.37)$$

For the vector LQs, we have the Lagrangian

$$\begin{aligned}\mathcal{L}_{\text{LQ}}^V = & \lambda_{V_0}^R \cdot \bar{d}\gamma^\mu e_R \cdot V_{0\mu}^{R\dagger} + \lambda_{\tilde{V}_0}^R \cdot \bar{u}\gamma^\mu e_R \cdot \tilde{V}_{0\mu}^\dagger \\ & + \lambda_{V_{1/2}}^R \cdot \bar{d}^c\gamma^\mu \ell_L \cdot V_{1/2\mu}^{R\dagger} + \lambda_{\tilde{V}_{1/2}}^R \cdot \bar{u}^c\gamma^\mu \ell_L \cdot \tilde{V}_{1/2\mu}^\dagger \\ & + \lambda_{V_0}^L \cdot \bar{q}\gamma^\mu \ell_L \cdot V_{0\mu}^{L\dagger} + \lambda_{V_{1/2}}^L \cdot \bar{q}^c\gamma^\mu e_R \cdot V_{1/2\mu}^{L\dagger} \\ & + \lambda_{V_1}^L \cdot \bar{q}\gamma^\mu \ell_L \cdot \hat{V}_{1\mu}^\dagger + \text{h.c.}\end{aligned}\tag{3.38}$$

We can use the Lagrangian to determine what will contribute to a neutron Fierz term. We can used table B.1 and table B.2 in appendix B, courtesy Dr. Vincenzo Cirigliano and Dr. Emilie Passemar [4], to calculate the scalar and tensor terms. The tables show the interaction term from the leptoquark Lagrangian, an effective four fermion vertex, and the Fierz-transformed vertex after Fierz rearrangement. First, from table B.1 equation I.3 we have a scalar term. Second, from table B.1 equation I.4, we have a tensor contribution. From table B.1 equation IV.3 and equation I.3, and from table B.2 equation I.4, we have a tensor term. Also from table B.2 in equation III.3, we have final scalar term. We can plug these into the form for the BSM  $b_n$

$$b_n = \frac{2g_S \varepsilon_S - 24\lambda g_T \varepsilon_T}{1 + 3\lambda^2}.\tag{3.39}$$

The Fermi Fierz term is

$$b_F = 2g_S \varepsilon_S,\tag{3.40}$$

where

$$\varepsilon_S = \frac{1}{2} \frac{\lambda_{S_0}^L \lambda_{S_0}^{R*}}{M_{S_0}^2} - 2 \frac{\lambda_{V_{1/2}}^L \lambda_{V_{1/2}}^{R*}}{M_{V_{1/2}}^2} - \frac{1}{2} \frac{\lambda_{S_{1/2}}^L \lambda_{S_{1/2}}^{R*}}{M_{S_{1/2}}^2} - 2 \frac{\lambda_{V_1}^L \lambda_{V_1}^{R*}}{M_{V_0}^2}.\tag{3.41}$$

We also have the Gamow-Teller component of the Fierz term,

$$b_{\text{GT}} = \frac{g_T}{2\lambda} \cdot \left( \frac{\lambda_{S_0}^L \lambda_{S_0}^{R*}}{M_{S_0}^2} + 4 \frac{\lambda_{S_{1/2}}^L \lambda_{S_{1/2}}^{R*}}{M_{S_{1/2}}^2} \right).\tag{3.42}$$

### 3.4.2 Leptoquark Mixing

Quark-lepton mixing and mixing among the leptotquark states has been investigated by Hirsch et al. [44]. Hirsch has derived an effective leptoquark mixing Lagrangian at low-

energy for an effective leptoquark mixing four-point interaction of  $u$ ,  $d$ ,  $\bar{\nu}_e$ , and  $e$  [44].

$$\begin{aligned} \mathcal{L}_{\text{LQ-mix}}^{\text{eff}} = & \bar{\nu} e_R^c \left[ \frac{\epsilon_S}{M_S^2} \bar{u} d_R + \frac{\epsilon_V}{M_V^2} \bar{u} d_L \right] + \bar{\nu}^c e_L^c \left[ \frac{\omega_S}{M_S^2} \bar{u} d_L + \frac{\omega_V}{M_V^2} \bar{u} d_R \right] \\ & - \bar{\nu} \gamma^\mu e_L^c \left[ \left( \frac{\alpha_S^{(R)}}{M_S^2} + \frac{\alpha_V^{(R)}}{M_V^2} \right) \bar{u} \gamma_\mu d_R - \sqrt{2} \left( \frac{\alpha_S^{(L)}}{M_S^2} + \frac{\alpha_V^{(L)}}{M_V^2} \right) \bar{u} \gamma_\mu d_L \right], \end{aligned} \quad (3.43)$$

where the scalar parameters are

$$\begin{aligned} \epsilon_I = & 2^{-\eta_I} \left[ \lambda_{I_1}^{(L)} \lambda_{\tilde{I}_{1/2}}^{(R)} \left( \theta_{43}^I(Q_I^{(1)}) + \eta_I \sqrt{2} \theta_{41}^I(Q_I^{(2)}) \right) - \lambda_{I_0}^{(L)} \lambda_{\tilde{I}_{1/2}}^{(R)} \theta_{13}^I(Q_I^{(1)}) \right], \\ \omega_I = & 2^{-\eta_I} \left[ \lambda_{I_0}^{(L)} \lambda_{I_0}^{(R)} \theta_{12}^I(Q_I^{(1)}) + \lambda_{I_0}^{(R)} \lambda_{I_1}^{(L)} \theta_{42}^I(Q_I^{(1)}) + \lambda_{I_{1/2}}^{(L)} \lambda_{I_{1/2}}^{(R)} \theta_{32}^I(Q_I^{(2)}) \right], \end{aligned} \quad (3.44)$$

and the vector coupling constants are

$$\begin{aligned} \alpha_I^{(L)} = & \frac{2}{3 + \eta_I} \lambda_{I_{1/2}}^{(L)} \lambda_{I_1}^{(L)} \theta_{24}^I(Q_I^{(2)}), \\ \alpha_I^{(R)} = & \frac{2}{3 + \eta_I} \lambda_{I_0}^{(R)} \lambda_{\tilde{I}_{1/2}}^{(R)} \theta_{23}^I(Q_I^{(1)}), \end{aligned} \quad (3.45)$$

with a mixing angle

$$\theta_{kn}^I(Q) = \sum_l \mathcal{N}_{kl}^{(I)}(Q) \mathcal{N}_{nl}^{(I)}(Q) \left( \frac{M_I}{M_{I_l}(Q)} \right)^2, \quad (3.46)$$

and where  $Q = -1/3, -2/3$  and  $I = S, V$ . We also define the mass scale for the scalar LQ to be  $M_S$  and the vector LQ,  $M_V$ .

Using this result we can extract the  $RR$  scalar coupling term

$$a_{RR}^S = \frac{\epsilon_S}{M_S^2}, \quad (3.47)$$

and the  $RL$  scalar term,

$$a_{RL}^S = \frac{\epsilon_V}{M_V^2}. \quad (3.48)$$

Also we have the  $LL$  pseudoscalar term

$$a_{LL}^S = \frac{\omega_S}{M_S^2}, \quad (3.49)$$

and the  $LR$  pseudoscalar term, both of which are highly suppressed from  $\pi^- \rightarrow e^- + \bar{\nu}_e$  and

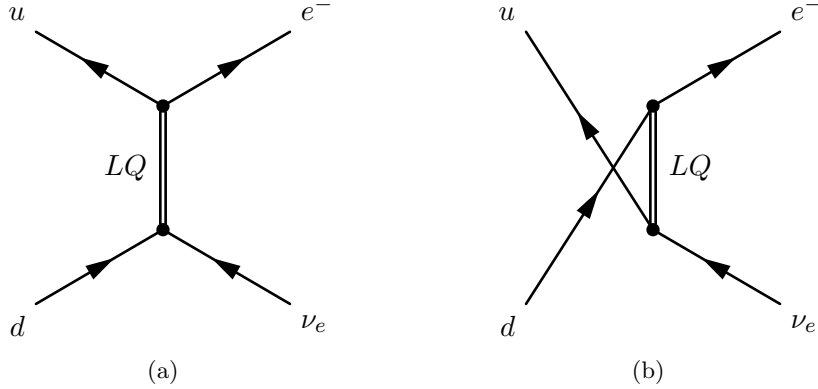


Figure 3.5. The Feynman diagrams for LQ quark-lepton mixing. The leptoquark in the diagram is a mixed  $L, R$  scalar, and vector mediator.

$\pi^- \rightarrow \mu^- + \bar{\nu}_\mu$  decay,

$$a_{RL}^S = \frac{\omega_V}{M_V^2}. \quad (3.50)$$

On the vector side, we have only  $LR$  and  $LL$  couplings. The  $LR$  side is

$$a_{LR}^V = \left( \frac{\alpha_S^{(R)}}{M_S^2} + \frac{\alpha_V^{(R)}}{M_V^2} \right). \quad (3.51)$$

The  $a_{LL}^V$  modifies the Standard Model contribution to  $V_{ud}$ ,

$$a_{LL}^V = \tilde{V}_{ud} + \sqrt{2} \left( \frac{\alpha_S^{(L)}}{M_S^2} + \frac{\alpha_V^{(L)}}{M_V^2} \right), \quad (3.52)$$

where  $\Delta_r$  are radiative correction.

Using equation (3.47), (3.48), and (3.16), we can compute the contribution to  $b_F$  from the LQ sector,

$$b_F = 2 \frac{g_S}{g_T} \left( \frac{\epsilon_S}{M_S^2} + \frac{\epsilon_V}{M_V^2} \right) \left[ \tilde{V}_{ud} + \sqrt{2} \left( \frac{\alpha_S^{(L)}}{M_S^2} + \frac{\alpha_V^{(L)}}{M_V^2} \right) \right]^{-1}. \quad (3.53)$$

Together, these give us two effective diagrams for the  $\beta$ -decay interaction.

### 3.5 Experimental Limits

The best limits for  $b_F$  are from a global fit to multiple superallowed  $J^\pi = 0^+ \rightarrow 0^+$   $\beta$ -decay  $ft$  values. Hardy and Towner [30] place this limit at

$$b_F = -0.0022 \pm 0.0026, \quad (3.54)$$

or  $|b_F| < 0.0043$  at 90% C.L. Several experiments have also measured  $b_{GT}$  using  $^{19}\text{Ne}$ ,  $^{60}\text{Co}$ ,  $^{114}\text{In}$  and  $^{107}\text{In}$  ( $\beta^+$ ). These are shown in table 3.1. We also can compare current limits on  $b_F$  with proposed future limits from experiments such as UCNB or UCNb. In figure 3.6 we plot possible limits for  $\varepsilon_S$  and  $\varepsilon_T$  assuming  $g_S = g_T = 1$ . However, this does not reflect the current uncertainties in the nucleon form factors. In figure 3.7 we plot possible limits for  $\varepsilon_S$  and  $\varepsilon_T$  with realistic limits expanded to account for the uncertainty in  $0.25 < g_S < 1.0$  and  $0.6 < g_T < 2.3$  at 90% confidence interval [15]. These limits assume one could measure  $b$  and  $B$  down to the  $10^{-3}$  level. For  $b_n$  this would require at least  $5 \times 10^7$  events.

Table 3.1. Experimental limits on  $g_T \varepsilon_T$  from  $\beta$ -decay

isotope	$g_T \varepsilon_T$ (90% C.L.)	$\gamma$	$b_{GT}$ (90% C.L.)	ref.
$^{60}\text{Co}$	$+1.5 \times 10^{-2}$ $-2.9 \times 10^{-3}$	0.980	$+0.018$ $-0.092$	Wauters [47]
$^{114}\text{In}$	$+1.3 \times 10^{-2}$ $-2.2 \times 10^{-2}$	0.934	$+0.139$ $-0.082$	Wauters [48]
$^{107}\text{In}$	$< 3.1 \times 10^{-3}$	0.94	$< 1.9 \times 10^{-2}$	Severijns [49]
$^{19}\text{Ne}$	-	0.99	$0.010 \pm 0.018$	Holstein [50]

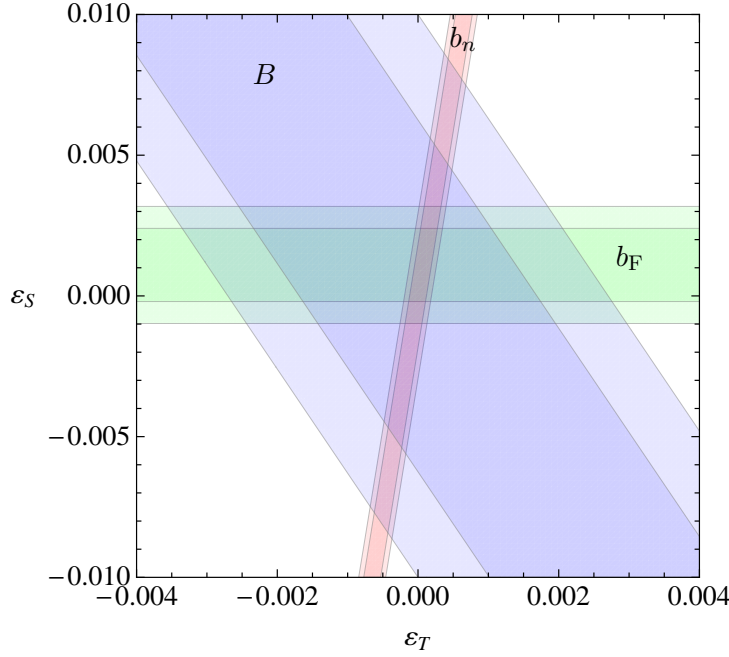


Figure 3.6. Possible experimental limits on  $\varepsilon_S$  and  $\varepsilon_T$  with the fixed values  $g_S = 1$  and  $g_T = 1$  assuming the accuracy on  $B$  and  $b_n$  of  $10^{-3}$  can be reached. For  $b_n$  this is achievable with  $5 \times 10^7$  events. The limit from superallowed beta decay is also shown.

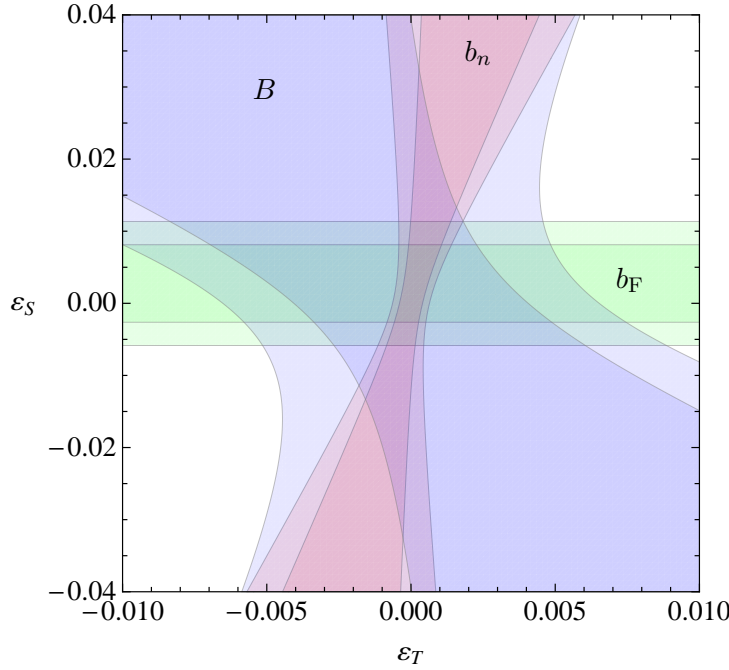


Figure 3.7. Plot of possible experimental limits on  $\varepsilon_S$  and  $\varepsilon_T$  showing possible values for  $g_S$  and  $g_T$ ,  $0.25 < g_S < 1.0$  and  $0.6 < g_T < 2.3$  90% confidence interval. The limit from superallowed beta decay is also shown.

## Chapter 4

# Ultracold Neutron Nonimaging Optics

Music is the arithmetic of sounds as optics is the geometry of light.

---

CLAUDE DEBUSSY

### 4.1 Introduction

Compound parabolic and elliptical concentrators, designed using the edge ray principle familiar from nonimaging optics [51] [52], have been used with success to collimate, focus and concentrate cold neutrons onto a distant target [53] [54]. In the ultra cold limit of the neutron, around a few hundred neV, these reflectors suffer from chromatic aberration as the kinetic energy and gravitational potential approach equal magnitude. Gravitational spectrometers and crank and storage “monochromators” have achieved energy resolutions of 1–10 neV [55], and UCN microscopes designed to compensate for chromatic aberration due to gravity using imaging optics techniques have achieved spatial resolutions of 0.1 mm [54]. But these techniques come at the cost of low UCN number efficiency by removing unused phase space volume. We show that the principles familiar from nonimaging optics can be applied to UCN optics to design an efficient vertical spectrometer. As a prime example, we investigate a vertical compound parabolic concentrator (CPC) which can isolate UCN in bands as narrow as  $\frac{1}{3}mga$  FWHM for a guide radius  $a$ . For 6 cm diameter guides, this gives 1 neV resolution, achievable after one pass through the optical system in the apogee time of the UCN,  $v_0/g$ .

This CPC spectrometer can be used for a number of new experiments such as measuring the neutron lifetime.

## 4.2 Nonimaging UCN Optics

In imaging neutron optics, each imaged neutron path is determined by Fermat's principle which also coincides with the classical action principle

$$\delta \int_a^b \frac{mv^2}{\hbar} dt = \delta \int_{t_a}^{t_b} L dt = 0, \quad (4.1)$$

so that the advancing wavefronts and the classical paths also coincide [56] [57]. We may consider all potentials, gravitational, magnetic and the Fermi potential, as affecting UCN via an effective index of refraction,

$$n^2(\vec{r}) = 1 - \frac{\lambda^2}{2m\hbar^2} V(\vec{r}). \quad (4.2)$$

For a rotationally symmetric system with angular momentum  $\ell$ , we have

$$V(r, z) = mgz \pm \mu_n B(r, z) + \frac{\ell^2}{2mr^2} + V_F(r, z). \quad (4.3)$$

For an imaging system, the integral from Fermat's principle is stationary for all neutron paths from object aperture to the image so we can solve for imaging optical surfaces using

$$\delta \int_a^b n^2 dt = 0. \quad (4.4)$$

To design a nonimaging optical system, we relax the requirement that this is satisfied for all paths emanating from the input aperture. Not every point in the input aperture must have a conjugate point in the target space. Instead we rely on the edge ray principle familiar from nonimaging photon optics [51] that states that imaged paths serve only as the *boundary* for the phase space volume of all other enclosed paths. We use Fermat's principle only to solve for the classical edge paths and pick a reflector surface or potential geometry parameters that map the input aperture extrema to the extrema of the output region. All paths within that imaged path boundary will be guaranteed to arrive at the target region, regardless of the path taken, the number of reflections, or the path complexity.

### 4.3 Compound Parabolic Concentrators

An interesting property that has been exploited in neutron optics is that a gravitational parabolic path originating at the focus of a parabolic surface will reflect to a conjugate parabolic path that also intersects the focus. A. Steyerl [58] called this property the “neutron fountain.” As a consequence, points in the neighborhood of the focus of a paraboloid are self-conjugate so the focal plane is imaged back on to itself. A. Steyerl and Frank used this property to design imaging systems and microscopes [59]. We use this property to show that a compound parabola can efficiently redirect UCN upward as with UCN microscopes but rather than rotate the parabola about its own axis as is done with UCN imaging optics, we place the focus of one parabola coincident with a reflected parabola, forming a compound parabola, and then rotate about the axis of symmetry.

For massive particles, it is not generally true that all imaged paths take equal time [56] [57], but for the case of the “neutron fountain”, the orbit time from the focus to the parabola wall and reflecting back, is given by

$$\oint dt = \frac{2v_a}{g}, \quad (4.5)$$

where  $v_a^2 \equiv v_0^2 + 2ag$ , where  $v_0$  is the initial velocity. This time depends only on the parabola’s focal length  $a$  and the UCN initial velocity magnitude  $v_0$ , and is independent of the initial angle to the vertical axis.

For the flight path from the focus ( $z = 0$ ) with an initial velocity  $(v_r, v_z) = (v_0 \sin \theta, v_0 \cos \theta)$ , the time to reach the parabolic reflector from the focus is

$$\frac{2a}{v_a - v_z}. \quad (4.6)$$

For each initial vertical velocity,  $v_z = v_0 \cos \theta$ , for a path starting at focus  $z = 0$  and angle  $\theta$  from the vertical axis, there is a reflected path with initial conditions  $v'_z = v_0 \cos \theta'$  that intersects the same point on the parabola. As we learned from the “neutron fountain” property, the path starting at the focus will reflect back onto the focus, so the orbit time in equation (4.5) is given by the sum of the two paths,

$$\frac{2v_a}{g} = \frac{2a}{v_a - v_z} + \frac{2a}{v_a - v'_z}. \quad (4.7)$$

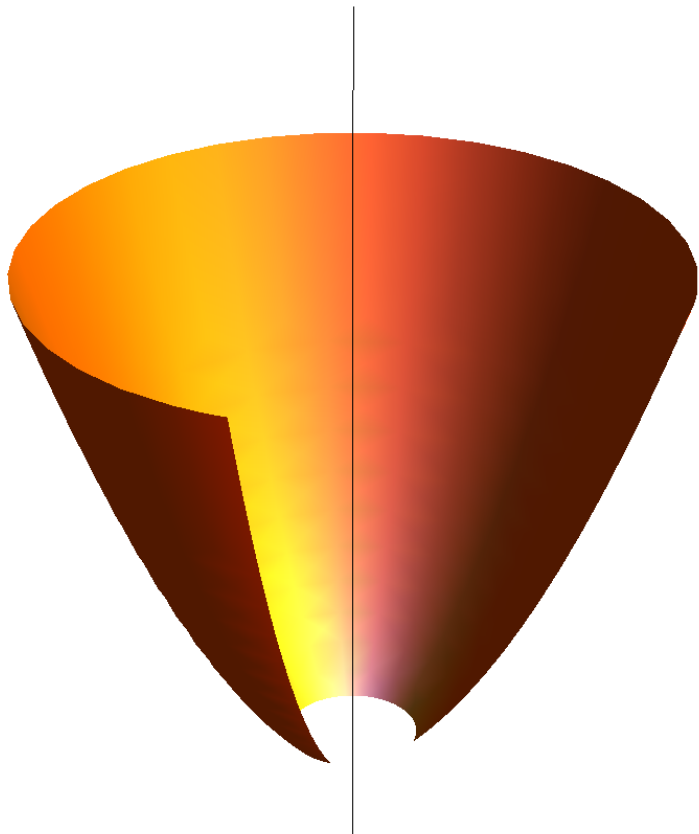


Figure 4.1. A CPC with a slice cut out.

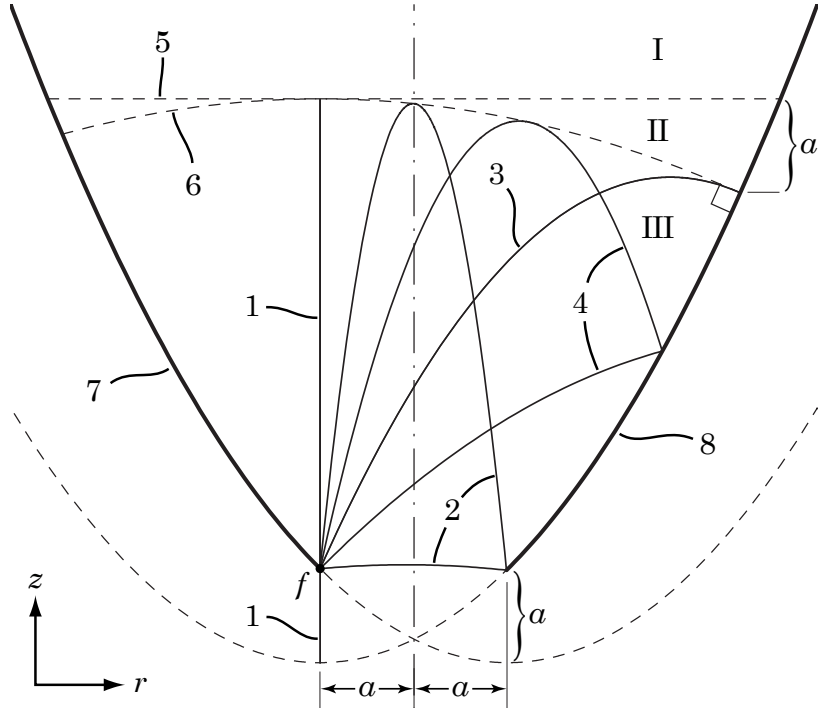


Figure 4.2. The construction of a CPC using the “neutron fountain” property. Each originating from the focus, these edge orbits are stationary to variations from Fermat’s principle and to orbital period. Examples shown are (1) a vertical orbit, (2) a focus to focus reflection orbit, (3) the self-conjugate orbit, and (4) an orbit with initial velocity with  $v_r = v_z = v_0/\sqrt{2}$ . In region I, with  $z > v_0^2/g$ , UCN are classically forbidden. All UCN from  $z = 0, r \in [0, a]$  will reach region II. And region III is bounded by the extrema of the edge orbits below 6, the ballistic umbrella of the point  $f$ . The compound parabola is formed by 7 and the reflection 8.

An extremum occurs at  $v_z = v'_z = v_0^2/v_a$ . These self-conjugate paths intersect the parabola at a height of  $v_0^2/2g - a$ . This reveals the interesting fact that the kinetic energy spread of the UCN orbits at their apogee is  $\Delta E < mga$  and is independent of  $v_0$ . Further, by the edge ray principle, all UCN emanating from the aperture between the focus to the parabola necessarily will be directed to enter region II, the region bounded below by the ‘ballistic umbrella’, the extrema of all monochromatic UCN paths originating at the parabola focus given by

$$z(r) = \frac{1}{4h}(r + a)^2 + h, \quad h \equiv \frac{v_0^2}{g}, \quad (4.8)$$

and bounded above by the classically forbidden height,  $z \leq v_0^2/2g$ .

From nonimaging optics for noncurvilinear rays, the general CPC family has reflective walls of a parabola that are tilted by the acceptance angle  $\theta_A$  to the axis of rotation. The traditional CPC design [51] with an aperture at  $z = 0$  radius  $a$ , has the parametric form

$$\begin{aligned} r(\varphi) &= \frac{2a' \sin(\varphi - \theta_A)}{1 - \cos \varphi} - a, \\ z(\varphi) &= \frac{2a(1 + \sin \theta_A) \cos(\varphi - \theta_A)}{1 - \cos \varphi}, \end{aligned} \quad (4.9)$$

where  $a'$  is the focal length of the parabola. For nonzero  $\theta_A$ , we truncate the CPC to a height of  $(a' + a) \cot \theta_A$ . When we take the limit  $\theta_A \rightarrow 0$  we find the CPC height as defined in [51] diverges and all UCN paths are contained inside the CPC. In this limit,  $a' \rightarrow a$  and the equation for a vertical CPC becomes

$$z(r) = \frac{1}{4a}(r + a)^2 - a. \quad (4.10)$$

The normal to the wall at the point  $(r, z)$  is

$$\hat{n} = \frac{(-r - a, 2a)}{\sqrt{r^2 + 2ar + 5a^2}}. \quad (4.11)$$

In this limit, all orbits originating from the input aperture are bound between extrema of the “neutron fountain” caustic, independent of their initial conditions.

We are interested in directing UCN vertically and the general solution of the intersection of the CPC wall with the UCN path can be solved in three dimensions with radial symmetry. This allows us to model the optical system in only two dimensions using cylindrical

coordinates. Without magnetic fields, the radially symmetric Euler-Lagrange equations are separable with vertical and radial solutions:

$$\begin{aligned} z(t) &= \frac{1}{2}gt^2 + v_0t + z_0, \\ r(t) &= \sqrt{v_\phi^2 t^2 + (v_r t + r_0)^2}. \end{aligned} \quad (4.12)$$

We need only solve for the intersection with the reflecting surface

$$-\frac{1}{2}g't^2 + v'_z t + z'_0 = \frac{1}{2}r(t), \quad (4.13)$$

where we have defined

$$g' \equiv \frac{v_a^2 - v_z^2}{2a}, \quad v'_z \equiv v_z - v_r \chi, \quad (4.14)$$

and

$$z'_0 \equiv z_0 + a(\chi^2 + \frac{3}{4}), \quad (4.15)$$

where  $\chi = r_0/2a$  is a dimensionless parameter. Squaring equation (4.13) gives the quartic equation with coefficients

$$\begin{aligned} A &= g'^2, \quad B = -4g'v'_z, \quad C = 4v_z'^2 - 4g'z'_0 - v_r^2 - v_\phi^2, \\ D &= 8v_z'z'_0 - 2v_r r_0, \quad E = 4z'_0^2 - r_0^2. \end{aligned} \quad (4.16)$$

Generally, we set the initial conditions so that  $(r_0, z_0)$  is at the entrance aperture at  $z_0 = 0$  and  $r_0 \in [0, a]$ , but the full solution is inappropriate if we have already solved for one intersection and are solving for another on the CPC surface. We need to remove the  $t = 0$  solution from the quartic for all intersections  $(r_n, z_n)$  for later times  $t > 0$ . This reduces computation time and numerical errors. When  $(r_n, z_n)$  lay on the wall they are dependent through equation (4.10) when  $z'_n \rightarrow \frac{1}{2}r_0$  and  $E = 0$ . The reflections also allow an iterative procedure to compute  $r_{n+1}, z_{n+1}$  from  $(r_n, z_n)$ . However, the computation is nonlinear, as the root of a cubic, and  $n$  can be any integer depending on initial conditions. There is no easy method to describe the state of an ensemble of UCN after an elapsed time without the use of a Monte Carlo simulation that recursively solves the cubic form of equation (4.16).

## 4.4 Monte Carlo Simulation

We use a Monte Carlo simulation in cylindrical coordinates with rotational symmetry of the CPC to analyze corrections to the 2D limits. The simulation first solves the quartic with coefficients in equation (4.16) and then iteratively solves the cubic form, which removes the  $t = 0$  solution, iteratively and propagates the path with specular reflections off the CPC wall. This simulation demonstrates that all UCN incident on the input aperture located on the interval  $r \in [0, a)$  and  $z = 0$  are redirected to the vertical region  $z \in [v^2/2g - a, v^2/2g]$  and each UCN path passes through region II, bound by  $z \leq v_0^2/2g$  and equation (4.8) as predicted.

We validated the simulation algorithm with a calculation of the simple case of a cylindrical wall with radius  $a$  instead of the CPC and compared to the analytic result of the probability distribution for a monochromatic random gas with initial velocity  $v_0$ , which has the distribution

$$P(z) = \sqrt{\frac{g}{v_0^2 z}}; \quad 0 \leq z \leq \frac{v_0^2}{2g}. \quad (4.17)$$

## 4.5 Results

In figure 4.3 we show the results of a small sample of UCN paths projected onto the  $(r, z)$  plane. The free part of the orbits are hyperbolic along the  $r$  axis due to conserved angular momentum, and parabolic in the vertical axis due to gravity. The multiple specular reflections off the CPC walls redirect all UCN into region II as predicted.

We ran batches of one million UCN in 5 neV increments with energies ranging from 5 to 40 neV. In figure 4.4, each probability distribution shows UCN are restricted to a horizontal band as wide as the focal length of the parabola and the diameter of the input aperture, which for this simulation was set to  $a = 4$  cm. However the probability curves still do not integrate to unity as there are some paths that fall back out of the input aperture at  $z = 0$ . While theoretically, these also should reach region II, in practice the CPC would require an input guide so these unphysical orbits are removed. The effect is most dramatic for the lowest energies,  $E_0 \approx mga$ .

While our predicted limits for the width of region II are  $\Delta E < mga$  the practical limits in three dimensions are much tighter and can be determined using our simulation to have a FWHM of  $\Delta E < \frac{1}{3}mga \approx 1.3$  neV for each initial energy and a guide width of  $a = 4$  cm.

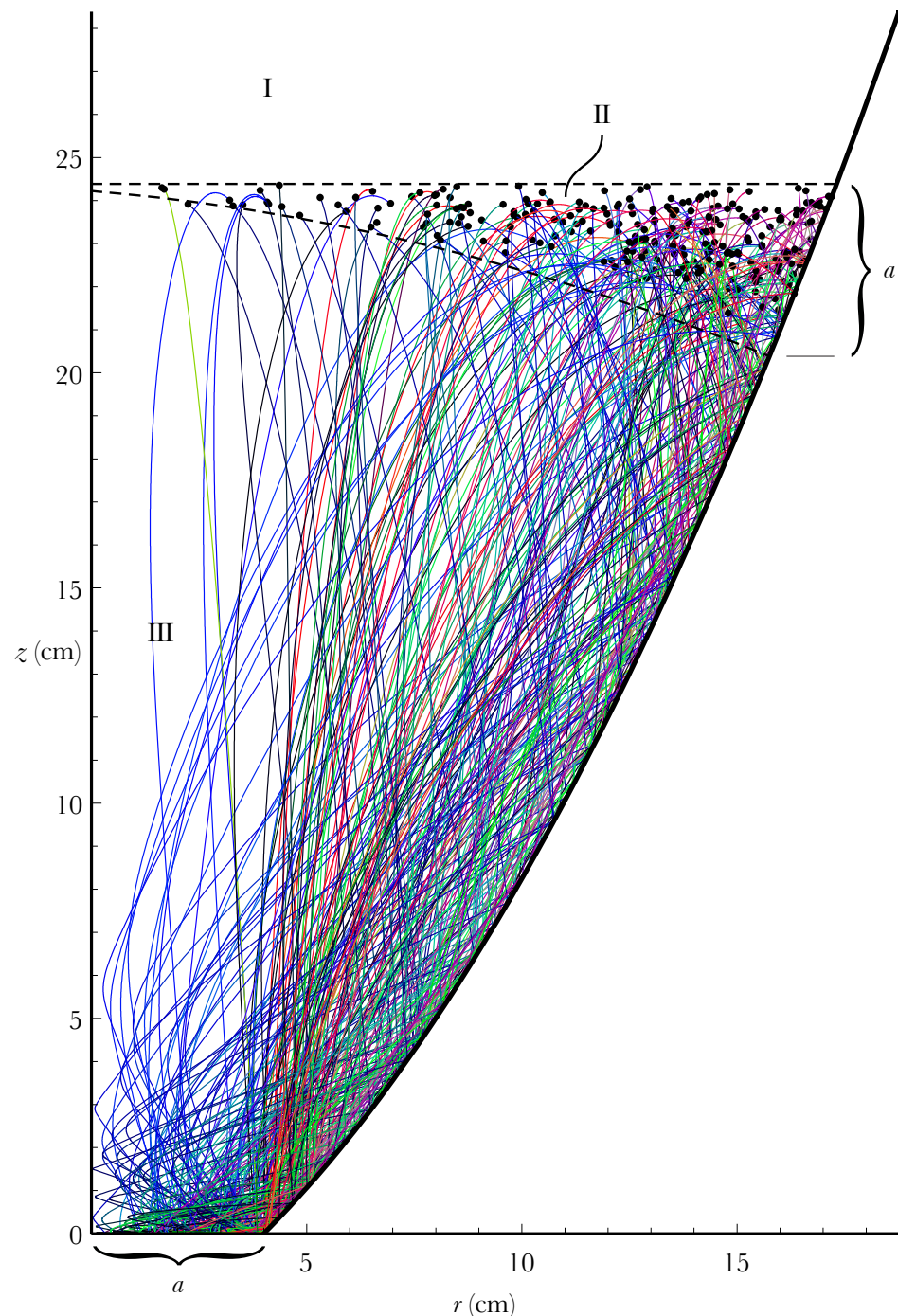


Figure 4.3. A 3D Monte Carlo simulation in the  $(r, z)$  plane of 1000 neutrons each with energy  $E = 25$  neV for one half orbit,  $0 < t < v_a/g$ . The solid circles indicate the end points at  $t = v_a/g$ . Each path passes into region II during the first orbit  $0 \leq t < 2v_a/g$ .

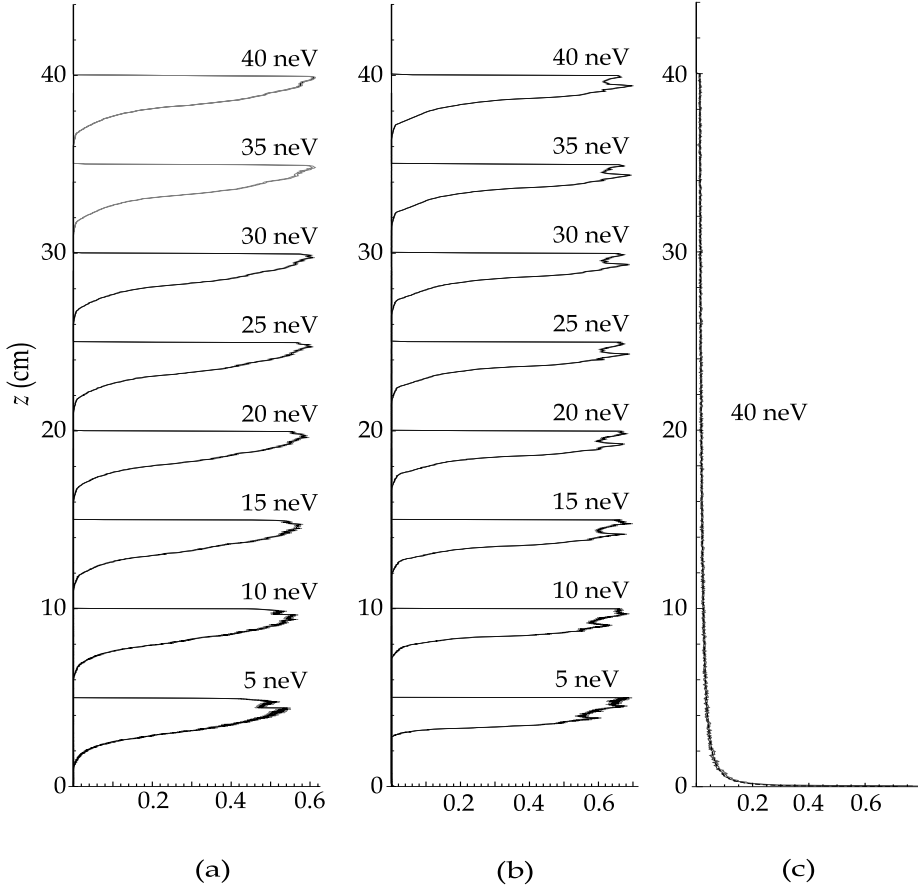


Figure 4.4. Results from  $10^6$  monochromatic UCN simulations for different energy levels. (a) The probability distribution of UCN at time  $t = v_a/g$  for energy levels 5–40 neV in a CPC. (b) The probability distributions of the apogees of UCN orbits during the first orbit  $t < 2v_0/g$  in a CPC. (c) The apogees of 40 neV UCN in a cylindrical guide.

## 4.6 Applications

### 4.6.1 Measuring the Neutron Lifetime

The lifetime of the neutron is an important component of refining the free parameters of the standard electroweak model particularly  $V_{ud}$  in the CKM matrix. Previous UCN trap designs relied on either walls [60] or magnetic multipoles [61]. Recently, interest has risen in high multipolarity Halbach array traps using permanent magnets to create a repulsive wall for low field seeking UCN [33]. The advantage of such a trap is that UCN of one polarization state can be repelled from the trap walls, thus minimizing neutron capture which quenches the storage lifetime. The radius of curvature is very large compared to

a standard reflection, on the order of the spacing of the multipole magnets,  $\lambda$ , which can be in the range  $\lambda \approx 1 \text{ mm} - 10 \text{ cm}$ . The difficulty of designing such a trap is that UCN with energy above  $E_H = 0.6\mu_n B_H \approx 50 \text{ neV}$  [33] will have enough energy to penetrate the magnetic barrier of the Halbach array, and the UCN may make contact with the surface exposing it to possible absorption by the magnet materials leading to an excess loss of UCN and resulting in a shorter measured lifetime. We must filter out UCN with an energy of less than  $E_H$  before the lifetime experiment begins.

UCN with energies of 40 neV and lower are desirable because they can be trapped inside a permanent magnetic bottle. We believe such a trap has the best possibility of holding UCN with the smallest possible systematic errors usually associated with walled traps. Walled traps have two main problems. Because the UCN scatter off of the nuclei of the walls themselves, even the lowest cross section materials still have a nonnegligible absorptive loss during the trapping time. The other problem is that with each collision, the UCN have a spin depolarization probability that introduces a loss from transitions into the high field seekers. A CPC can be used as a possible design of a lifetime experiment as it can redirect UCN to an absorber in 0.3 s to quickly and efficiently remove overly energetic and marginally trapped neutrons from a permanent magnetic trap that can only hold UCN with energies under  $\mu_n B \approx 50 \text{ neV}$  using NdFeB magnets [33].

#### 4.6.2 Pulsed UCN Source Using a CPC

The CPC creates an effective spectrometer with resolution of better than  $E = mga$ . This remarkable property leads us to propose a system for reducing the energy of UCN provided they start with a small phase space volume. For UCN created with a pulsed source such as  $\text{SD}_2$ , the creation and expulsion time is typically less than 100 ms and the energy distribution is boosted to the Fermi potential of deuterium. This gives a relatively short pulse ( $\tau_{\text{SD}2} \ll \sqrt{2a/g} \approx 0.1 \text{ s}$ ) of narrow band ( $\Delta E \approx \frac{1}{3}mga$ ) UCN which can be directed through a CPC to a trapping region. A mechanical shutter, if carefully timed with the pulse, closing  $v_a/g$  after the pulse, can select out a band of UCN that will remain trapped at a lower energy. Typically, these sources are only a few centimeters across so the minimum energy band that may be trapped is as small as 1–5 neV.

Experiments such as GRANIT [62] have detected quantization of gravitationally bound states by lowering an absorbing detector onto UCN passing over a reflective horizontal plate.

Currently, these experiments are limited by the poor statistics due to the low occupancy of the lowest ground states. A pulsed source coupled to a CPC with a trapping region could generate large numbers of UCN in these states as well as increase the experiment time due to the low lateral velocity of the trapped UCN. If combined with a pulsed UCN source and a mechanical shutter, the CPC can be used to collect high densities of UCN with reduced energy at a higher gravitational potential above the source. These can be guided to an experimental chamber to make large statistics quantized gravitational states measurements. UCN with such low lateral velocity can also be dropped into unperturbed vertical paths for efficient and compact  $n\bar{n}$  oscillation searches.

## 4.7 Conclusion

We have applied the design principles of nonimaging optics to UCN transport optics. We use these principles to a design an apparatus, the CPC with zero acceptance angle, that redirects monochromatic UCN (with velocity  $v_0$ ) from a Lambertian horizontal disk source, upward into a bound region. The region is strictly bound below the classically forbidden upper half-plane, and above the ballistic umbrella of the focus,  $h - (r + a)^2/4a \geq z \geq h$  where  $h = v_0^2/g$ . We have showed, using Monte Carlo simulation, that this bound holds empirically in three dimensions for a range of initial velocities and analyzed the resultant probability distribution of the UCN both after one-half average orbit time  $v_a/g$  and at the apogee of each individual orbit. We discussed the possibility of using these data to construct an apparatus that can have a shutter to trap UCN in the lower energy phase of the orbit. Such a device could trap UCN in the target region with energies  $E < mga$ . Such a device could be used to preserve the phase space of a spallation UCN source to more efficiently gravitationally cool UCN for use in experiments that require population of the lowest energy UCN such as gravitational states experiments and  $n\bar{n}$  searches. We also discussed how to construct an efficient spectrometer with effective resolution of  $E \approx mga/3$ . Such a spectrometer could be used to remove marginally trapped UCN from a magnetic trap for a precision neutron lifetime experiment.

We present the CPC as an interesting use of UCN nonimaging optics, but there are many new experimental designs that can also use the same design principles. We hope that this will motivate many novel and efficient geometries in future experiments that require

efficient UCN transport.

## Chapter 5

# Transmission of Ultracold Neutrons Through Thin Foils

UCN produced in the spallation source at LANSCE are required to pass through a pressure retaining foil that isolates the solid duterium ( $SD_2$ ) source [63] from the experiment downstream. A simple foil placed anywhere in the UCN beam line would pose a barrier to the transport of many UCN due to the Fermi potential that would reject a section of the available phase space. This potential can be positive, as is the case with aluminum, or negative, as is the case with titanium. In either case, some UCN will reflect off the foil. In addition there is neutron capture. As this cross section increases with  $1/v$ , there is an advantage to having greater velocity while passing through the foil.

One solution to both the potential barrier and the scattering problems, is to place the foil in the center region of a Prepolarizing Magnet (PPM) which operates at 6T. The field is large enough to provide a longitudinal boost that allows punch through of the high-field seeking UCN through large potential materials. This gives more options from which to choose materials to use as an isolation window.

As part of the UCNA experiment, UCN move from the source, out of the shield blocks, to the PPM, to the main polarizing magnet, to a spin flipper, and then to a beta decay detection volume. In this volume, the  $\beta$  decay asymmetry,  $A$ , is measured by counting the directionality of the resultant beta decay electrons. As mentioned, safety requirements for UCNA maintain that in order to contain the  $SD_2$  in case of a rapid warm-up event, windows are required at the exit of the beam line, just outside the shield packaging. The windows must pass a pressure test using water in order to prove they can withstand a certain blowout pressure from the source.

We do not place the window right above the SD<sub>2</sub> source [64], due to concern of freeze-out of contaminants onto the window surface, which could absorb UCN, decreasing the UCN production density. This was the motivator to place the window in the center of the PPM instead.

We also had a need for windows for <sup>3</sup>He gas detectors [65]. These detectors are very sensitive to UCN and we have used them with great success using aluminum. There is still a need to make the loss through the detector windows even better.

We decided to try different types of foils to see which worked best: aluminum, Mylar, and zirconium, each of different thicknesses. What we found was that surface properties matter as much as bulk properties. While much work was done on neutron transport through foils for cold and thermal neutrons [66–70], as well as using polarizing magnets of foils inside magnets to measure the UCN spectrum, [31] we found little work on the transport of UCN through thin foils with absorbing or reflective surface coatings as well as simultaneous bulk loss.

The center region of the PPM has a profile approximately given by the axial field of a solenoid along  $x$ :

$$B(x) = \frac{1}{2}\mu_0 NI (\cos \theta_1 + \cos \theta_2), \quad (5.1)$$

where  $r$  is the radius of the coil and

$$\theta_1 = \frac{b - x}{\sqrt{(b - x)^2 + r^2}}, \quad \text{and} \quad \theta_2 = -\frac{b + x}{\sqrt{(b + x)^2 + r^2}}. \quad (5.2)$$

## 5.1 1D Quantum Model

In this section, we will examine the theory behind transport of UCN through a thin foil. We can set up a simplified quantum mechanical model of neutrons traveling through a foil in one dimension immersed in a magnetic field. The simple model may include a thin surface layer with a thickness that is much smaller than the wavelength of neutrons passing through the foil. This thin layer can be approximated as a infinitesimally thin complex delta function potential with the real and imaginary parts given in terms of bulk potential and loss per distance.

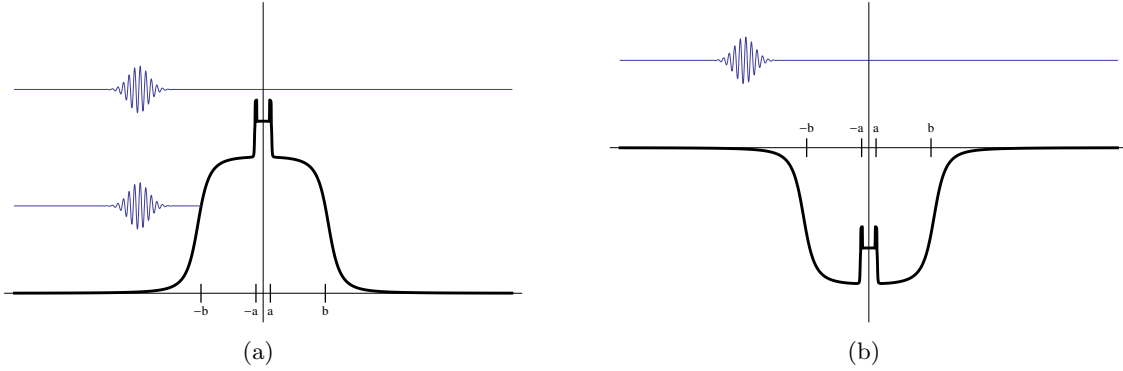


Figure 5.1. The potential of a thin coated foil. Low field-seeking UCN in (a) with insufficient classical energy are not able to penetrate the magnetic potential summed with the foil Fermi potential. The high-field seekers see a potential as shown in (b), which allows them to penetrate the foil with a sufficiently large magnetic field.

Consider a step and delta potential, shown in figure 5.1 given by

$$V(x) = \begin{cases} 0; & \text{approximately } |x| \gtrsim b, \\ \pm\mu B; & \text{in the region } |x| \lesssim b, \\ V + iU \pm \mu B; & \text{where } |x| < a, \\ (\alpha + i\beta)\delta(x \mp a); & x = \pm a. \end{cases} \quad (5.3)$$

We want to find the transmission and reflection coefficients for an unbound particle with energy,  $E$ , so we consider a wave incident on the left, in the region  $x \ll b$ . The general, time-independent solution for such a free particle at constant step potentials  $V(x)$ , is

$$\psi(x) = a_L(x)e^{ik(x)x} + a_R(x)e^{-ik(x)x}, \quad \text{where} \quad \frac{\hbar^2 k^2}{2m} = E - V(x). \quad (5.4)$$

In the region near  $|x| \approx b$ , the neutrons enter the magnetic field and become polarized such that their spins are either aligned or antialigned with the field. If they are aligned, they are low-field seekers, and are repulsed by the center magnetic field inside the PPM. If they are antialigned, they are high-field seekers, and are accelerated by the field inside the PPM.

The wavefunctions for the three regions that are parameterized by left-moving and

right-moving coefficients  $A, B$  and  $C$  are

$$\psi(x) = \begin{cases} A_R e^{ikx} + A_L e^{-ikx}, & x < -a, \\ B_R e^{ik'x} + B_L e^{-ik'x}, & |x| < a, \\ C_R e^{ikx}, & x > a. \end{cases} \quad (5.5)$$

We must enforce zeroth-order continuity on the wavefunction. The boundary conditions are

$$\begin{aligned} \psi(-a) &= A_R e^{-ika} + A_L e^{ika}, \\ \psi(\pm a) &= B_R e^{\pm ik'a} + B_L e^{\mp ik'a}, \\ \psi(a) &= C_R e^{ika}. \end{aligned} \quad (5.6)$$

We have a special boundary equation for the continuity of the wave function at the complex delta potential at  $x = \pm a$ , which integrates out to

$$[\psi'_-(\pm a) - \psi'_+(\pm a)] + g\psi(\pm a) = 0. \quad (5.7)$$

These boundary conditions require the first order derivatives which are

$$\begin{aligned} \psi'(-a) &= ikA_R e^{-ika} - ikA_L e^{ika}, \\ \psi'(\pm a) &= ik'B_R e^{\pm ik'a} - ik'B_L e^{\mp ik'a}, \\ \psi'(a) &= ikC_R e^{ika}. \end{aligned} \quad (5.8)$$

By defining the normalization  $R = A_L/A_R$ ,  $T = C_R/A_R$ ,  $b_L = B_L/A_R$ , and  $b_R = B_R/A_R$ , we have the system of equations,

$$\begin{aligned} 1 - Re^{2ika} - \frac{k'}{k} b_R e^{i(k-k')a} + \frac{k'}{k} b_L e^{i(k+k')a} + \frac{g}{ik} \left( 1 + Re^{2ika} \right) &= 0, \\ \frac{k'}{k} b_R e^{-i(k-k')a} - \frac{k'}{k} b_L e^{-i(k+k')a} - T \left( 1 - \frac{g}{ik} \right) &= 0, \\ 1 + Re^{2ika} - b_R e^{i(k-k')a} - b_L e^{i(k+k')a} &= 0, \\ b_R e^{-i(k-k')a} + b_L e^{-i(k+k')a} - T &= 0. \end{aligned} \quad (5.9)$$

We can transform these equations into four more

$$\left( 1 + \frac{k'}{k} \right) b_R e^{i(k-k')a} + \left( 1 - \frac{k'}{k} \right) b_L e^{i(k+k')a} = 2 + \frac{g}{ik} \left( 1 + Re^{2ika} \right). \quad (5.10)$$

Similarly we have

$$\left(1 + \frac{k'}{k}\right) b_R e^{-i(k-k')a} + \left(1 - \frac{k'}{k}\right) b_L e^{-i(k+k')a} = T \left(2 - \frac{g}{ik}\right). \quad (5.11)$$

This has solutions

$$\begin{aligned} R &= \frac{e^{-2ika}}{\Lambda} \left[ e^{2ik'a} (k^2 + (g - ik')^2) - e^{-2ik'a} (k^2 + (g + ik')^2) \right], \\ T &= -\frac{4e^{-2ika}kk'}{\Lambda}, \end{aligned} \quad (5.12)$$

where

$$\Lambda = e^{2ik'a} (ig - k + k')^2 + e^{-2ik'a} (ig - k - k')^2, \quad (5.13)$$

where we have split  $k'$  into real and imaginary parts,

$$k' \rightarrow \kappa + i\lambda, \quad (5.14)$$

and defined

$$-\frac{\hbar^2 g}{2m} = \alpha + i\beta. \quad (5.15)$$

The total transmission through the foil is given by the magnitude of the wavefunction on the right hand side of the foil,

$$|T|^2 = \frac{16k^2(\kappa^2 + \lambda^2)}{|\Lambda|^2}. \quad (5.16)$$

Since the magnetic field has smooth edges compared to the wavenumber of the neutron wavefunction, we may treat the wave packet as completely classical. Reflection will occur if and only if the neutron has energy below the magnetic potential,  $E < \pm \mu_n B_x$ . Thus we need only consider the QM components when dealing with the foil which has spacial components near the wave number of neutron. The energy and wave number inside the region  $|x| \lesssim b$  are given by

$$\frac{\hbar^2 k^2}{2m} = E \pm \mu_n B_x. \quad (5.17)$$

Inside the bulk of the foil the relation is

$$\frac{\hbar^2(\kappa + i\lambda)^2}{2m} = E \pm \mu_n B_x - V - iU. \quad (5.18)$$

Solving for  $k$ ,  $\kappa$ , and  $\lambda$  gives

$$k = \sqrt{\frac{2m}{\hbar^2}(E \pm \mu B)}, \quad (5.19)$$

and

$$\kappa = \sqrt{\frac{m}{\hbar^2} \sqrt{E \pm \mu B - V - \sqrt{-4U^2 + (E \pm \mu B - V)^2}}}, \quad (5.20)$$

and

$$\lambda = \sqrt{\frac{8mU}{\hbar^2 \kappa^2}}. \quad (5.21)$$

## 5.2 Foil Measurements

### 5.2.1 Depth Profilometry

Depth profile measurements were made by Russell Mammei at Virginia Polytechnic Institute using Auger electron profilometry and SIMS [71]. The results of the scans are shown in figure 5.2 and reveal a thin layer of about 60 nm of carbon and about 16 nm of oxide. The carbon layer is actually a hydrocarbon layer, but the H:C ratio cannot be determined using the Auger technique used, but the ratio is constant over the first tens of nanometers. It is likely to be in the alkane family, so the ratio is likely to be  $\approx 2:1$ .

### 5.2.2 Experimental Setup

The experimental setup is shown in figure 5.3. To measure the transmission through several foils, we inserted several foil thicknesses of different materials in the highest field region of the PPM just outside of the gate valve exiting the shield block that encases the LANSCE UCN source. After the foil, another stainless steel tube guided neutrons through a round elbow, called the “elephant trunk,” to a 1 meter long guide straight down to a UCN  ${}^3\text{He}$  detector. The windows, are mounted and sealed with o-rings in the center of the magnet. The guides are stainless steel tubes with an inside diameter of 60 mm. The guides are electropolished to increase the specularity of the inner surface. After the UCN pass through the PPM, the guide system bends down to boost the UCN using gravity so that they fall 1.3 meters onto our  ${}^3\text{He}$  proportional detector. The gravitational boost gives them  $\approx 130$  neV kinetic energy in the longitudinal direction of the guide and perpendicular to the detector window (which is needed to contain the  ${}^3\text{He}$  gas). For these experiments, we still used aluminum windows for detector windows, that are still transparent enough to allow most

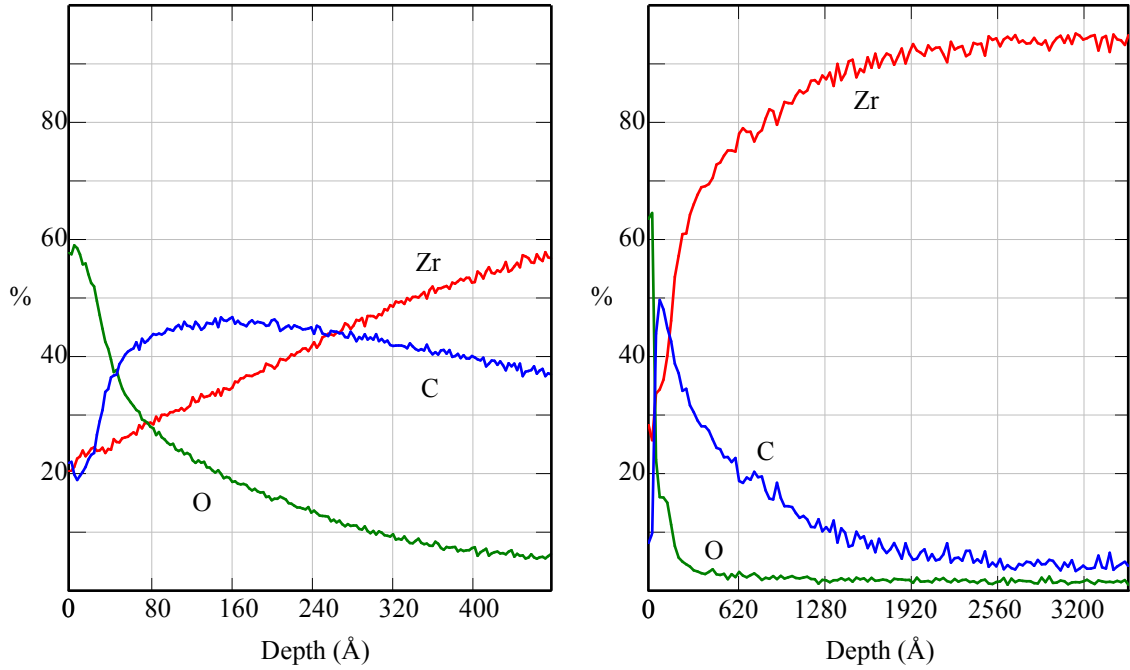


Figure 5.2. Depth profile of Zr foils cleaned with Citranox for both 5 Å and 50 Å resolution. Courtesy: Russell Mammei.

UCN to enter.

### 5.2.3 Results

We measured the transmission through zirconium foils, as well as no foils, and fit an interpolating function to the results. We can analyze the longitudinal spectrum by fixing the transmission at zero magnetic field to 100% transmission. Next an interpolating function was fit to the no-foil curve. In theory, this curve could be used to fit the reflection function of the various curves, but we believe that in practice this would require a Monte Carlo of the source-generated spectrum in order to separate the longitudinal spectrum from the full omnidirectional spectrum [72]. The initial raw data collected is shown in figure 5.4 as a function of longitudinal energy across the foil. For the case when there is no foil present in the PPM, the transmission decreases as the PPM magnetic field is increased. This is due to the splitting between polarization states. Low-field seekers are unable to penetrate the magnetic barrier, so only half of the UCN are able to pass through the field. When there is a foil, the transmission actually increases with the field. This is because the Fermi potential

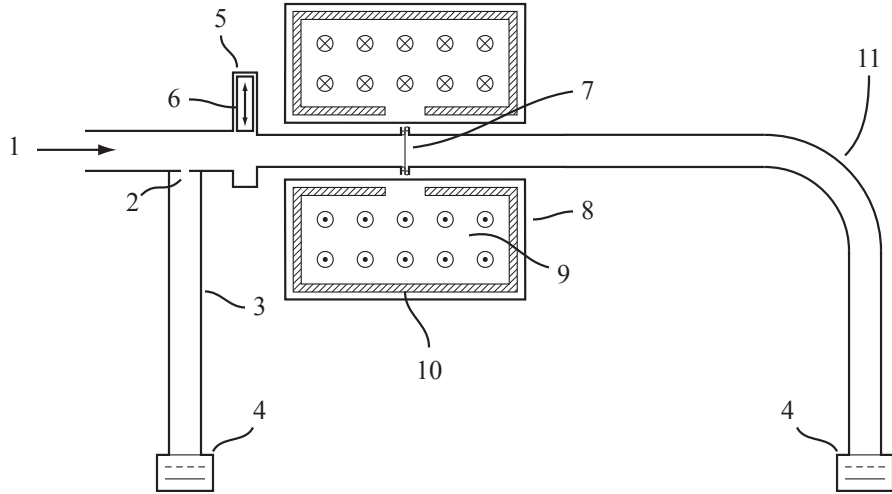


Figure 5.3. Experimental setup for the foil transmission measurements; (1) UCN; (2) Gate valve monitor port; (3) UCN guide; (4)  ${}^3\text{He}$  UCN detector; (5) Gate valve; (6) Valve door; (7) Foil; (8) PPM; (9) PPM current coils; (10) PPM yoke; (11) Elephant trunk.

of the foil (90 neV) is enough to prevent a large fraction of UCN from penetrating. As the field is increased, half the neutrons (the high-field seekers) are boosted past this potential, but the fraction of the spectrum that is able to penetrate the foil barrier is still greater than that at zero magnetic field. By dividing the transmission through each foil thickness by the transmission with no foil, we obtain the relative transmission fraction as a function of longitudinal energy as shown in figure 5.5. The foil transmission,  $|T|^2$ , can be used to

d (μm)	0 T	1 T	2 T	3 T	4 T	5 T	6 T
	0 neV	60 neV	120 neV	180 neV	240 neV	300 neV	360 neV
25.4	0.155	0.318	0.593	0.788	0.859	0.877	0.882
50.8	0.153	0.332	0.605	0.781	0.841	0.857	0.861
101.6	0.109	0.265	0.522	0.702	0.767	0.784	0.788

Table 5.1. Foil transmission as a function of Zr foil thickness and magnetic field strength and longitudinal energy. Longitudinal energy is listed below the magnetic field values.

extract the surface and bulk effects via

$$|T|^2(x, E_\ell) = c(E_\ell) + \xi(E_\ell)x, \quad (5.22)$$

by fitting the constants  $c(E_\ell)$ , the surface term, and  $\xi(E_\ell)$ , the bulk term, where  $x$  is the foil thickness. The results are presented in table 5.2. Some of this surface and bulk loss

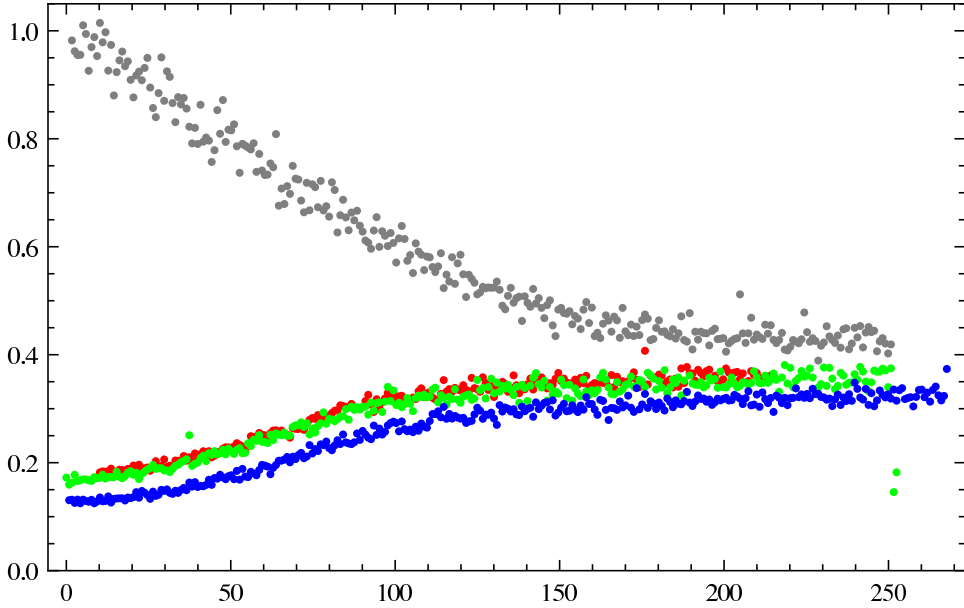


Figure 5.4. A family of plots of absolute transmission of UCN through Zr foils as a function of thickness.

B	0 T	1 T	2 T	3 T	4 T	5 T	6 T
$E_\ell$	0 neV	60 neV	120 neV	180 neV	240 neV	300 neV	360 neV
$c(E_\ell)$	0.177	0.352	0.635	0.828	0.896	0.914	0.918
$\xi(E_\ell)$	0.000635	0.000794	0.00103	0.00118	0.00123	0.00125	0.00125

Table 5.2. Foil transmission coefficients as a function of magnetic field strength.

is likely surface dependent [73–75]. We find that the constant component of the relative transmission,  $c(E_\ell)$ , increases dramatically with longitudinal energy. This is to be expected as the quantum mechanical reflection off the surface will decrease with increased energy. The bulk transmission per distance,  $\xi(E_\ell)$ , also increases, as we would expect from the  $1/v$  dependence of the cross section of the bulk material.

#### 5.2.4 Summary

We measured the transmission of UCN through a zirconium foil compared to the transmission with no foil. This foils were place inside of a polarizing magnet and the field was varied so as to alter the longitudinal spectrum of UCN passing through the foils. Bulk loss was measured separately from surface loss by measuring varying thicknesses of foils. We derived the surface loss from a thin layer, represented by a delta function, on the surface of a foil. What this told us is that there is inherent loss on the surface of the Zr foil that is not in the

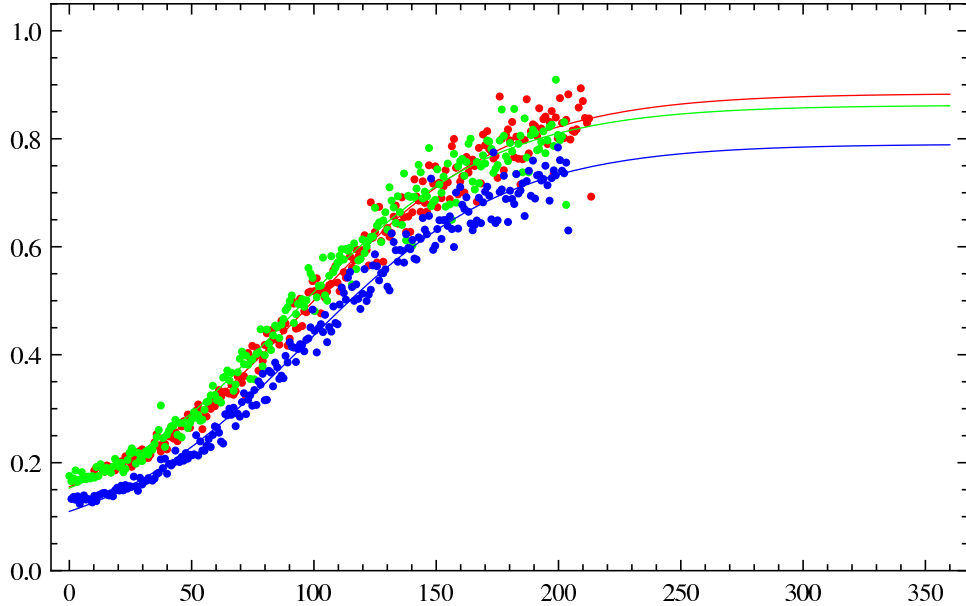


Figure 5.5. A family of plots of relative transmission of UCN through Zr foils as a function of thickness. The lines are arc tangent extrapolations to the data.

bulk. We may be able to use this knowledge to design better foils with a treated surface that is designed to scatter and reflect less. Using the QM model and a good understanding of the real and complex components of the Fermi potential of the surface materials, we may be able to design foils with near zero surface loss. Since this is the dominant loss factor, we might expect foils with very high transmission factors well over 90%. This measurement allowed us to find a replacement for the aluminum foils which had less than 80% transmission [76]. This improvement increased the UCN density available to the UCNA and other experiments downstream of the LANL UCN source.

## Chapter 6

# Cosmological Limits on Fierz Interference

Images of broken light, which dance  
before me like a million eyes, they call  
me on and on across the universe.

---

JOHN LENNON

One important limit on the Fierz term in neutron beta decay can come from Big Bang nucleosynthesis (BBN). The Fierz term,  $b_n$ , modifies the Standard Model neutron decay rate,  $\Gamma_{\text{SM}}$ ,

$$\Gamma(n \rightarrow p + e^- + \bar{\nu}) = \left(1 + b_n \frac{m_e}{E_e}\right) \Gamma_{\text{SM}}(n \rightarrow p + e^- + \bar{\nu}). \quad (6.1)$$

In the primordial universe during the nucleosynthesis era, up to about 3 minutes after the Big Bang, neutrons and protons were in equilibrium. As the universe cooled, this equilibrium began to freeze out, and the  $n/p$  ratio began to rapidly lower as neutrons decayed or were bound up in light nuclei. Prior to and during this transition, when a positron is absorbed by a neutron, (instead of an electron being emitted as with decay) the  $b_n$  term in the reaction rate will have an opposite sign from the decay rate equation [77],

$$\Gamma(n + e^+ \rightarrow p + \bar{\nu}) = \left(1 - b_n \frac{m_e}{E_e}\right) \Gamma_{\text{SM}}(n + e^+ \rightarrow p + \bar{\nu}). \quad (6.2)$$

These rate altering effects can modify the  $n/p$  ratio which then completely determines the  ${}^4\text{He}$  primordial abundance. [78] Thus we can turn this argument around and can deduce a limit on  $b_n$  from the  ${}^4\text{He}$  primordial mass fraction,  $Y_p$  familiar from observational cosmology [29].  $Y_p$  can be determined today from observation of nebulae where less stellar formation

has occurred since the dawn of the universe, leaving the primordial gas fractions relatively pure. In these regions, the mass fraction of hydrogen,  $X$ , and helium,  $Y$ , are expected to be in ratios largely untouched by contaminants generated by supernova remnant gases. These regions of gas can tell us how the final state of the BBN nuclear reaction network ended a few minutes after the Big Bang.

The neutron lifetime also strongly affects the  $n/p$  ratio. The recent lower values for the neutron lifetime  $\tau_n$  [79], will also alter the predicted primordial helium abundance [28, 80]. We will use the most recent value from [17].

## 6.1 Big Bang Nucleosynthesis

Big Bang nucleosynthesis provides tight constraints on searches for new physics [81]. To see why, we must look at how the helium abundance is strongly affected by the  $n/p$  ratio set by the BBN epoch. After the baryogenesis epoch when neutrons and protons were created, they were essentially in thermal equilibrium with a  $n/p$  ratio set by the neutron-proton mass difference  $m_n - m_p = \Delta = 1.293$  MeV. This equilibrium is given by  $n/p = e^{-\Delta/T}$  [29]. Weak equilibrium came to end once the weak reaction rate

$$\Gamma_{n \leftrightarrow p} = \frac{7\pi}{60}(1 + 3\lambda^2)G_F^2 T^5 \quad (6.3)$$

was less than the Hubble expansion rate

$$H \approx \sqrt{\frac{8\pi G}{3}\rho_\gamma}, \quad (6.4)$$

where the relativistic particle density is

$$\rho_\gamma = \frac{\pi^2}{30}g_*T^4, \quad (6.5)$$

with  $g_*$  the massless degrees of freedom [28] and in the Standard Model,  $g_* = 5.5 + \frac{7}{4}N_\nu = \frac{43}{4}$  [82]. This end of equilibrium occurs when the baryon temperature  $T \approx 1$  MeV. This epoch is referred to as the “freeze out” because neutrons and protons cease to be in equilibrium past this point and neutrons begin to freely beta decay [28].

There are three reactions involved before the freeze out,



For the early universe, these reactions are temperature dependent and we require a new phase space integral to calculate the reaction rates that reduces to equation (2.18) from Chapter 2 at low energy. The new phase space integral has the fermion state occupancy terms  $1/(1 + e^{xz})$  for the electron occupancy factor and  $1/[1 + e^{(x_0-x)z_\nu}]$  for the neutrino occupancy factor, where  $x$  is the reduced energy  $E/m_e$  and  $x_0 = E_0/m_e \approx 2.53$  is the neutron endpoint. Here  $z$  and  $z_\nu$  are the reduced temperatures of the final states where  $z = T/m_e$  and  $z_\nu = T_\nu/m_e$  are the baryon and neutrino temperatures, respectively.

There are six components to the reactions in (6.6). The first is just the standard neutron decay familiar from low energy,

$$\Gamma_{n \rightarrow pe\bar{\nu}} = \frac{1}{\tau_n I_0} \int_0^{x_0} \frac{(x+b)(x-x_0)^2 (x^2-1)^{1/2}}{(1+e^{-xz})(1+e^{(x_0-x)z_\nu})} dx, \tag{6.7}$$

where  $I_0$  is the standard phase space integral,

$$I_0 = \int_0^{x_0} x^{1-k} (x-x_0)^2 (x^2-1)^{1/2} dx. \tag{6.8}$$

We then have the rates for the absorption of a positron or an electron neutrino

$$\Gamma_{ne \rightarrow p\nu} = \frac{1}{\tau_n I_0} \int_{-\infty}^{-x_0} \frac{(x-b)(x-x_0)^2 (x^2-1)^{1/2}}{(1+e^{xz})(1+e^{(x_0-x)z_\nu})} dx, \tag{6.9}$$

and

$$\Gamma_{n\nu \rightarrow pe} = \frac{1}{\tau_n I_0} \int_{-\infty}^{-x_0} \frac{(x-b)(x-x_0)^2 (x^2-1)^{1/2}}{(1+e^{-xz})(1+e^{-(x_0-x)z_\nu})} dx. \tag{6.10}$$

We also have the reverse reaction  $p + e \rightarrow n + \nu$  which is [29]

$$\Gamma_{pe \rightarrow n\nu} = \frac{1}{\tau_n I_0} \int_{x_0}^{\infty} \frac{(x+b)(x-x_0)^2 (x^2-1)^{1/2}}{(1+e^{xz})(1+e^{(x_0-x)z_\nu})} dx. \tag{6.11}$$

The other two reverse reactions proceed in a similar manner.

## 6.2 BBN Simulation Code

To determine a limit for  $b_n$  in terms of the uncertainty on  $Y_p$ , we turn to running BBN code which has been used with success to predict the primordial light element abundance up to  ${}^4\text{He}$ . The code has proved accurate enough to be used previously to test beyond the Standard Model physics. The BBN code first uses the baryon to  $\gamma$  fraction  $\eta_B \approx 6.05 \times 10^{-11}$  to estimate the correct density for integrating forward the Friedmann equations. Next, it uses this result to establish a nuclear reaction network in terms of the differential rates of each of the nuclei that are modeled. Finally, it uses this reaction network to predict late time mass fractions of the light elements available to the network.

Since  $n/p$  determines  ${}^4\text{He}$  abundance, the most important part of the reaction rate network is the conversion from  $p$  to  $n$  and back again. This is all done in a thermal bath of electroweak constituents,  $e^-$ ,  $e^+$  and neutrinos.

The neutron rate integrands are combined, by analytic continuation from six integrals into four. Swapping of the proton and neutron is just the same integrand by analytic continuation to the region from the endpoint to infinity, but with  $x \rightarrow -x$ . The integrals are now

$$\begin{aligned} \Gamma(n \rightarrow p) = (\tau_n I_0)^{-1} & \int_1^\infty \frac{(x+b)(x-x_0)^2(x^2-1)^{1/2}}{(1+e^{-xz})(1+e^{(x-x_0)z_\nu})} \\ & + \frac{(x-b)(x+x_0)^2(x^2-1)^{1/2}}{(1+e^{xz})(1+e^{-(x+x_0)z_\nu})} dx. \end{aligned} \quad (6.12)$$

Similarly we have the two integrals for protons going to neutrons,

$$\begin{aligned} \Gamma(p \rightarrow n) = (\tau_n I_0)^{-1} & \int_1^\infty \frac{(x-b)(x+x_0)^2(x^2-1)^{1/2}}{(1+e^{-xz})(1+e^{(x+x_0)z_\nu})} \\ & + \frac{(x+b)(x-x_0)^2(x^2-1)^{1/2}}{(1+e^{xz})(1+e^{-(x-x_0)z_\nu})} dx. \end{aligned} \quad (6.13)$$

As the baryon and neutrino temperatures are changing over the course of the nucleosynthesis era, the best way to perform these integrals is to use the Big Bang nucleosynthesis (BBN) code. We modified code provided by Sarkar et al. [83] written by Wagoner [84] and then latter modified by Kawano [85,86] to include the Fierz term, accounting for the appropriate sign in the simulation, as well as the temperatures and phase space densities of the electron, positron, and neutrino populations.

### 6.3 Simulation Results

Figure 6.1 shows a plot of the nuclei,  $p$ ,  $^4\text{He}$ ,  $D$ ,  $^3\text{He}$ ,  $T$ , and the neutron  $n$  mass fractions as a function of temperature of the early universe,  $T$ .

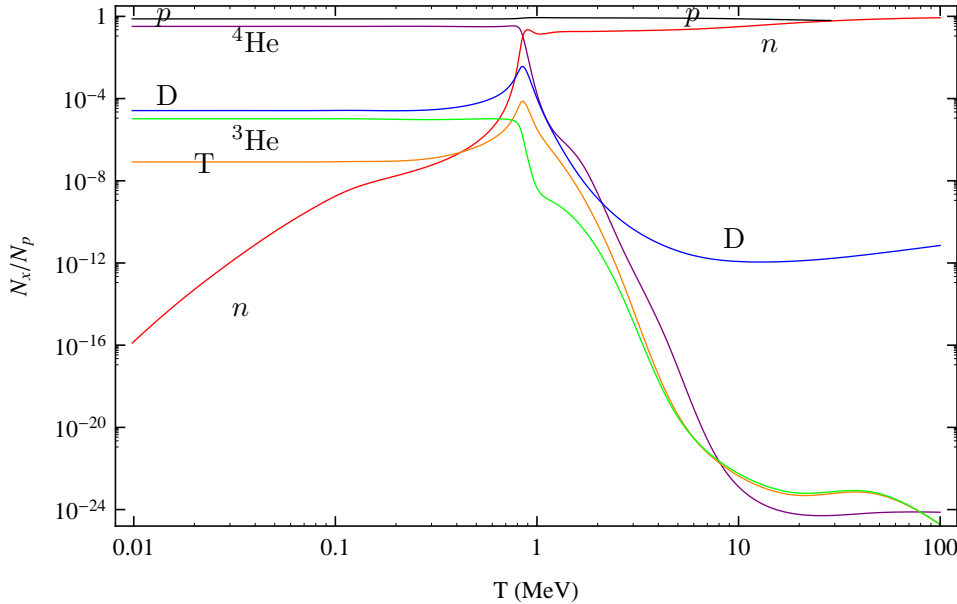


Figure 6.1. The results of the mass fraction relative to hydrogen ( $p$ ) as a function of Baryon temperature.

A fit to the results can be found in figure 6.2. We fit a linear function to the helium abundance mass fraction  $Y_p = Y_b b_n + Y_0$  and found

$$Y_b = 0.0773 \pm 0.0008, \quad \text{and} \quad Y_0 = 0.24502 \pm 0.00008. \quad (6.14)$$

Comparing this to the best current estimate for  $Y_0$ , this gives us a bound on  $b_n$ . There is some discrepancy in the estimates of  $Y_p$ , the primordial helium-4 abundance, but one estimate with the tightest bounds, by Izotov and Thuan (IzTh) [87] has  $Y_p = 0.2448(13)$ . This value is a combined value from their different analysis methods, each determined from observing spectra from 45 uniformly distributed, low metallicity HII regions [80]. These regions are selected because they are believed to have the most primordial content, undisturbed by stellar nucleosynthesis [88]. However, in 2010, Izotov and Thuan presented a new determination of  $Y_p$  based on 93 spectra of 86 low-metallicity extragalactic HII regions. Their analysis took into account new systematic effects such as collisional and fluorescent enhance-

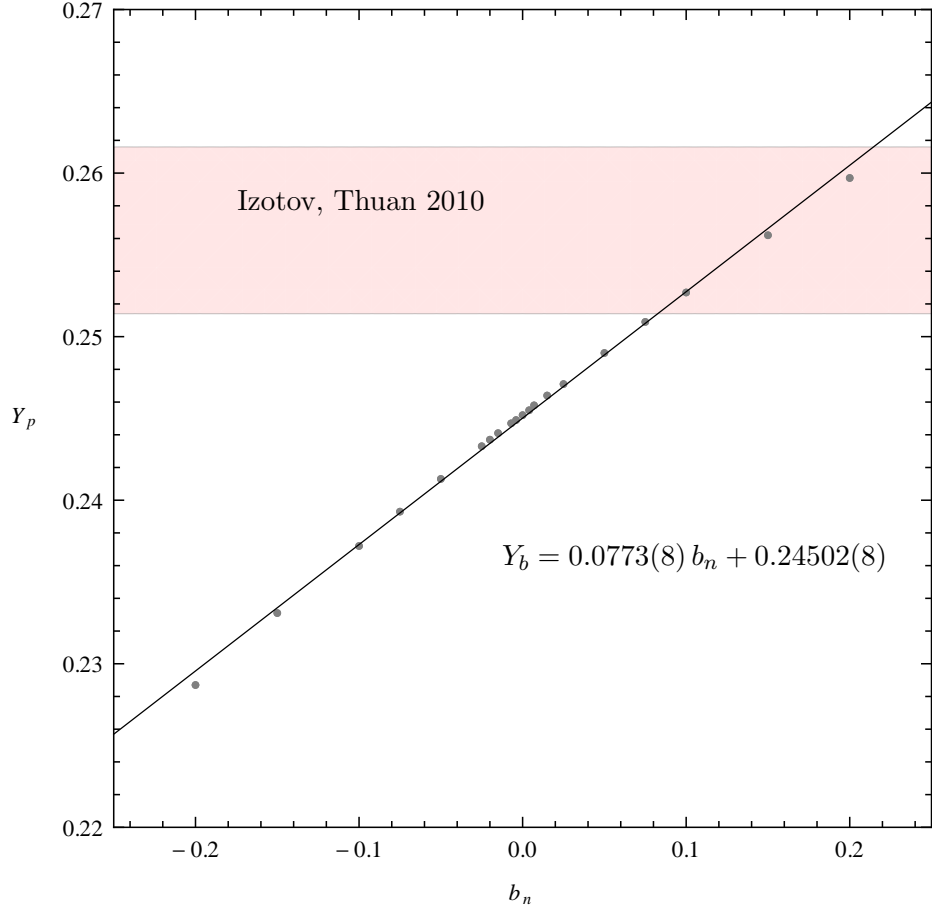


Figure 6.2. A fit of BBN code runs with different values for  $b_n$  versus the  ${}^4\text{He}$  mass fraction,  $Y$ .

ment of HeI recombination lines, HeI stellar absorption lines, and collisional and fluorescent excitation of hydrogen lines [89]. They give the best value estimated from a Monte Carlo combination of these systematic errors to be  $Y_p = 0.2565 \pm 0.0010$  (stat.)  $\pm 0.0050$  (syst.). This puts an estimate on  $b_n$  at

$$b_n = 0.149 \pm 0.078. \quad (6.15)$$

As was shown in chapter 3, we can write the neutron Fierz term in terms of Fermi and Gamow-Teller subcomponents,

$$b_{\text{GT}} = \frac{(1 + 3\lambda^2)b_n - b_F}{3\lambda^2} \approx 1.2b_n - 0.23b_F \quad (6.16)$$

Combined with the bounds from Hardy and Towner [30] for  $b_F$ , which had  $b_F = -2.2(2.6) \times$

$10^{-3}$ , this gives

$$b_{\text{GT}} = 0.179 \pm 0.092 \quad (6.17)$$

The systematic error in equations (6.15) and (6.17) give us limits  $0.021 < b_n < 0.277$  (90% C.L.) and  $0.028 < b_{\text{GT}} < 0.330$  (90% C.L.).

## Chapter 7

# Extracting the Fierz Term from $\beta$ -asymmetry Measurements

The universe is asymmetric and I am persuaded that life, as it is known to us, is a direct result of the asymmetry of the universe or of its indirect consequences.

---

LOUIS PASTEUR

The Fierz interference term introduced in chapter 3 provides a powerful device for searching for TeV-scale physics, even compared to high-energy experiments such as the Large Hadron collider (LHC). This enhanced sensitivity comes from  $m_e/E$  dependence as  $E \rightarrow m_e$ . The Fierz term for the neutron,  $b_n$ , gives us a method for putting limits on  $b_F$  and  $b_{GT}$ , which in turn put limits on  $\varepsilon_S$  and  $\varepsilon_T$ . As in chapter 3, the Fierz term modifies the energy spectrum of the electron emitted from neutron beta decay.

In this chapter we will explore in more detail a few experiments that are designed to measure other correlation parameters,  $A$  and  $B$  in particular, that may be able to set some reasonable limits on  $b$  compared to the existing *status quo* [30, 47–49]. Two experiments stand out due to their low background beta energy spectra, the UCNA and UCNB experiments at LANSCE [90, 91]. UCNA and UCNB both fill UCN into a decay volume and measure beta-decay correlation coefficients with two  $2\pi$  detectors on either end of a superconducting confining magnetic field. The UCNA experiment has been up and running since 2007. UCNB is a planned upgrade to UCNA using high resolution large area silicon detectors. UCNB’s detectors have better resolution, but also a larger backscatter correction

due to the higher  $Z$  of silicon over the MWPC and scintillator combination of UCNA. These experiments were not designed to measure  $b_n$ , but in this chapter, we explore how one goes about extracting the Fierz term from these asymmetry experiments and present results and progress on that front.

## 7.1 The UCNA Experiment

The UCNA experiment at LANSCE is designed to measure the neutron  $\beta$  asymmetry parameter,  $A$ , from (2.14). The UCNA experiment see figure 7.1, is composed of three

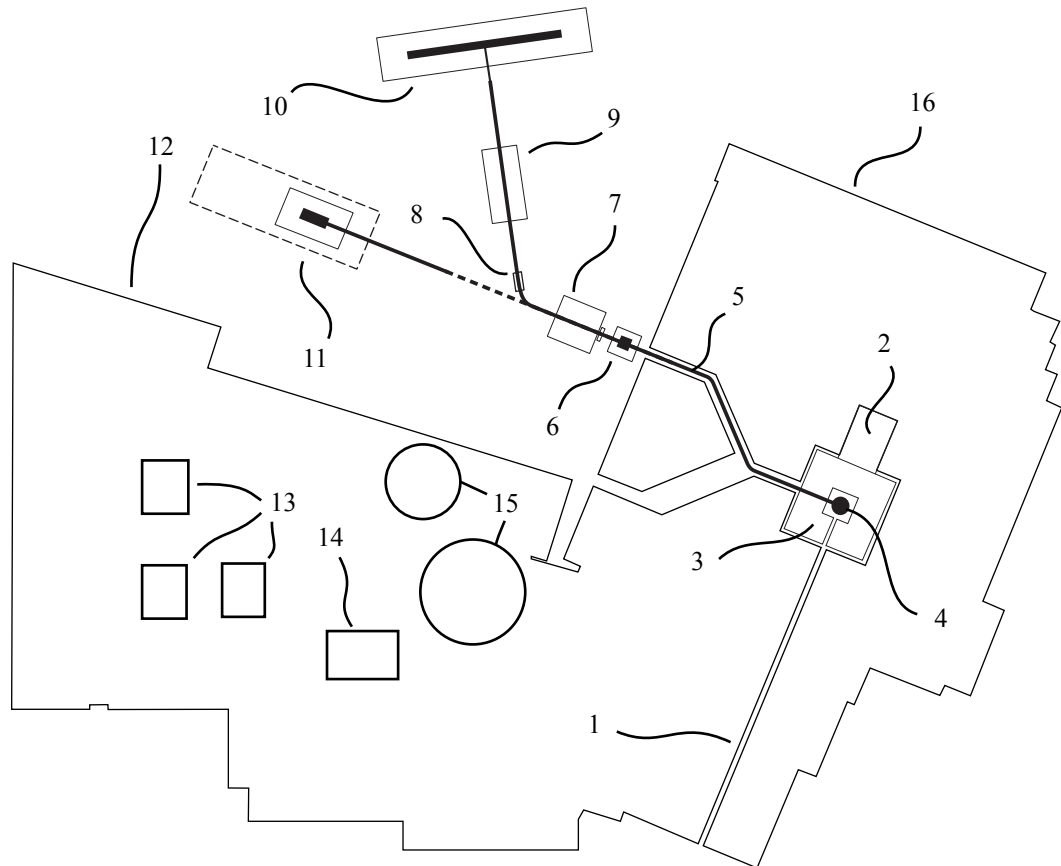


Figure 7.1. Detail of the Area B experimental hall at LANSCE. (1) proton beam; (2) beam stop; (3) Be, graphite, polyethylene moderators; (4) W and target and  $\text{SD}_2$  UCN source; (5) UCN “dog leg” guide; (6) UCNb experiment and UCN gate valve; (7) PPM; (8) switcher (UCNA); (9) AFP (UCNA); (10) SCS (see detail in figure 7.2); (11) nEDM test cryostat; (12) cryogenics mezzanine; (13) He compressors; (14) He liquefiers; (15) LHE dewars; (16) shielding package.

major magnet systems; the Prepolarizing Magnet (PPM), the Adiabatic Fast Passage (AFP) spin-flipper, and the Superconducting Spectrometer (SCS). UCN generated in the solid deuterium ( $SD_2$ ) source are guided through the PPM and are polarized in a 6 T field. Once polarized, high-field seeking UCN pass through the magnet while the low-field seeking UCN are reflected back into the source. Some of these reflected UCN are spin-flipped and have another chance to enter back into the experiment as high field seekers. Most, however, are captured on the source guide walls. Some are lost in the  $SD_2$  by neutron capture onto deuterium. However, the source has a flapper that closes after a sequence of UCN pulses. Some UCN leak back into the source and are absorbed. The polarized UCN are guided around a 45° elbow through a switcher that can redirect UCN heading the other direction down into a UCN detector. UCN headed through the switcher pass through another polarizing magnet, inside the AFP package, this time at 7 T. After this second polarizing stage, UCN pass through the AFP spin-flipping resonance coils where the spins can be adiabatically flipped. This critical step allows for selection of the desired spin state for injection into the SCS.

Once in the SCS decay trap, UCN can either decay freely, be absorbed, up-scatter on the walls of the trap, or escape back through the small rectangular guide through which they entered. Figure 7.2 shows the detail of the UCNA experiment. Once UCN enter the SCS and decay, the decay electrons spiral toward one detector on either side, guided by the 1 T holding field. The electrons pass through a MultiWire Proportional Chamber (MWPC) filled with neopentane, an unsaturated heavy hydrocarbon molecule. Hydrocarbon is preferred for its low- $Z$ , low-back scattering properties and because it can be pressurized to 100 torr. Backscattering is mostly caused by low energy electrons that take a random walk inside the material in the detectors (windows, wire chamber gas, wires, or scintillator) and return back out the direction they entered. The electrons then may travel to the other detector. This has the effect of diluting the asymmetry. The wire chamber gas is supported by kevlar backed 6  $\mu m$  thick mylar windows on the front and 6  $\mu m$  on the back. The backing gas behind the MWPC is  $N_2$  at 100 torr. Inside the  $N_2$  gas the scintillator is connected to light guides which direct scintillation photons towards four PMTs. The PMTs are inside bucking coils which are inside soft steel shields, to compensate for the field from the SCS magnet [92, 93]. The position of the impact point of each electron can be determined by the intersection of the  $x$  and  $y$  cathode plane wires in the MWPC. This allows for measurement

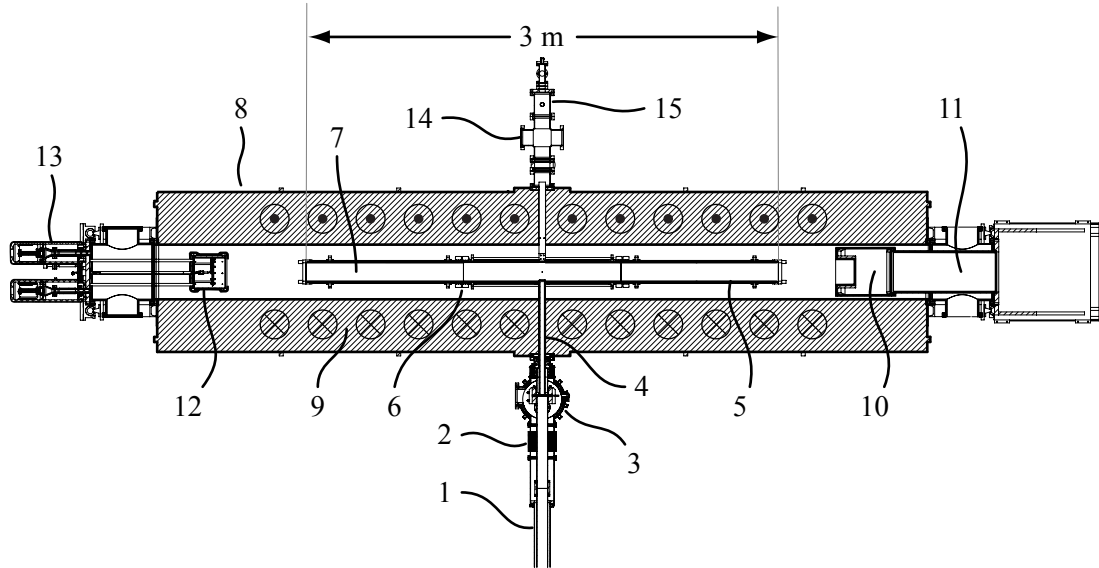


Figure 7.2. Detail of the SCS experimental setup. Show on the left are the UCNB silicon detectors while on the right are the UCNA MWPC/scintillator detectors. (1) UCN guide; (2) shutter vacuum system; (3) UCN shutter; (4) square UCN guide; (5) UCN decay trap; (6) decay trap clamps; (7) decay fiducial volume; (8) SCS; (9) SCS magnet; (10) UCNA MWPC and scintillator; (11) UCNA detector gas system; (12) UCNB Si detector; (13) UCNB detector electronics; (14) calibration load lock; (15) load lock vacuum system.

of the position dependent gain of the scintillator for improved energy reconstruction. [94]. With 16 wires in each direction, we achieve a resolution of  $\approx 2$  mm over the 45 mm radius fiducial volume [93].

### 7.1.1 UCNA Gain Monitoring System

Extracting correlation parameters such as  $A$  and  $b$  from the energy spectrum of electrons in a scintillating system requires good calibration of the overall gain and linearity of the relationship between the true electron energy and the light output measured. To monitor linearity and gain in the UCNA apparatus, we employed two systems. One system was a  $^{207}\text{Bi}$  source attached to each PMT face. The pulser was a 12 mm diameter scintillator cylinder with the radioactive material embedded inside the center. The second system was a custom Caltech-designed light emitting diode (LED) and photodiode (PD) paired system. In figure 7.3 we show the optical schematic view of the photodiode, LED gain and linearity monitoring system for UCNA and UCNb. Light is generated by a CAEN C529 6 channel LED driver at approximately 100 Hz with a width of about 8 ns. These rates were best set to match the real pulse shape from beta decay. One of two LEDs fire

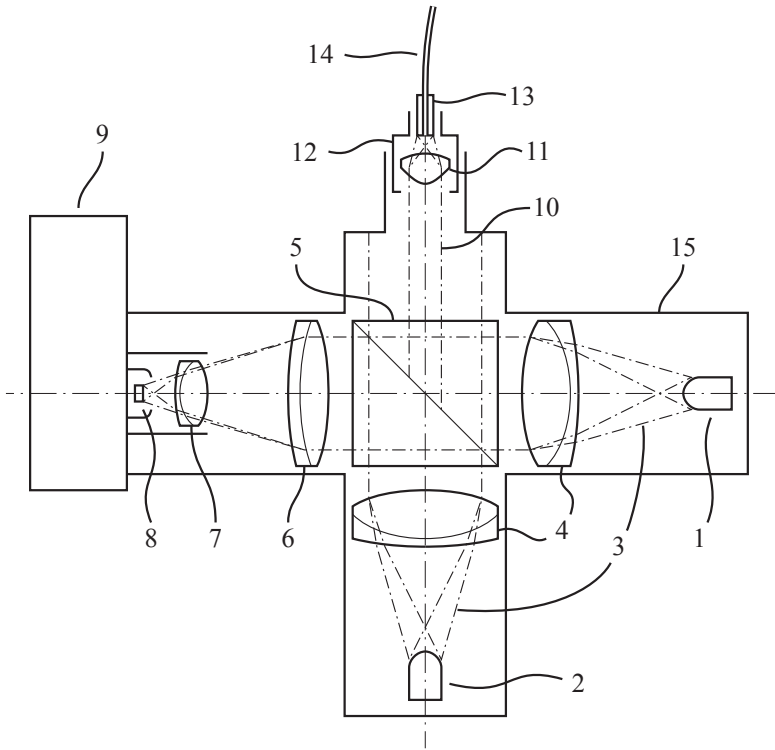


Figure 7.3. Optical schematic of the LED/PD pair gain and linearity monitoring system. (1) 405 nm LED; (2) 465 nm LED; (3) edge rays; (4) achromatic objective lenses; (5) beam splitter; (6) first stage imaging lens; (7) second imaging lens; (8) photodiode; (9) photodiode amplifier; (10) edge rays of fiber phase space; (11) fiber aspherical imaging lens; (12) factory assembled fiber collimator; (13) fiber SMA connector; (14) 400  $\mu\text{m}$  UV/VIS fiber; (15) 1 inch lens tube housing;

depending on a LabView software system. There is both a 405 nm (violet) LED (LED495E from Thorlabs in Newton, New Jersey), and a 465 nm (cyan) LED (ThorLabs LED465E). Two LEDs are used because the PMT photocathode has different thermal coefficients for different wavelengths near the blue region. The temperature, and therefore part of the gain shift, can be monitored independently from the relative gain shift of the two LEDs.

Edge rays, (3 in figure 7.3), denote the boundary of the image plan used by a spherical doublet lens (ThorLabs AC254-035-A), to collimate light prefocused by the optical housing lens of the LEDs. The collimated light passes through a nonpolarizing 50/50 beam splitter, (ThorLabs CM1-BS013). The reentrant primary lens, spherical achromatic doublet (ThorLabs AC254-035-A), focuses onto the secondary spherical achromatic thin doublet, (ThorLabs AC254-035-A) images the clear aperture of the photodiode objective lens onto

the factory mounted photo-diode, where it is amplified by an integrated preamp module (ThorLabs PDA10A).

The light from the two LEDs is combined and then split 50/50 through a reduced phase space ray bundle. Although the fiber coupling unit (ThorLabs F671SMA-405) has a tiny clear aperture of a few millimeters, it contains a pre-aligned ideal aspherical monochromatic lens designed for single mode laser coupling to a fiber at 405 nm. Thus the phase space that is captured is efficiently imaged onto the entrance plane of the SMA fiber head. Despite being designed for 405 nm, the fiber collimating lens is easily able to couple both 405 and 465 nm light into the 400  $\mu\text{m}$  fiber entrance. The fiber is optically connected to the scintillator in the experiment. However, the imaged spot of the LEDs is much larger than the entrance window to the fiber, thus the phase space is reduced. This is critical to the functioning of the system as the photodiode requires  $10^7$  photons to register a signal, but the PMTs require only a small sampled fraction of that light on the order of a few tens to thousands of photons at the most. Since the photodiode has low gain, and since it sees the split light from the LEDs, it should have a very linear dependence on the number of photons coupled to the fiber.

The entire system is held together with 1 inch optical threaded tubing, to align the optics and to prevent stray light from entering into the system. Data are taken to measure the linearity by ramping the pulse height of the trigger to the CAEN driver module. For a large fraction of the pulse heights (up to 20 V) the pulse height corresponded with light output of the LED. The 50/50 splitter allows for this linearity to be monitored with the Si photodiode. This light pulse measurement can be compared directly to the PMT response of the SCS detector. As the PMTs are not as linear as a photodiode, a linearity curve of light in versus PMT response can be measured. An example of linearity data is shown in figure 7.4. In 2010, UCNA did not have the LED/photodiode pair installed, so detailed measurement of the linearity response of the PMTs was not possible. However, in 2011, the system described here was installed, but not temperature stabilized. Photodiodes, when reversed biased, are typically linear better than  $10^{-4}$ . Also, with a temperature stability of 0.5%/ $^\circ\text{C}$ , a measurement of PMT gain down to the 0.1% level or better is achievable if the photodiode is stabilized to 0.2 $^\circ\text{C}$  or better. A fit to data taken from just one run from 2011 data shows a nonlinearity of 0.4%. In future analysis, this linearity can be applied to the UCNA data to increase the fidelity of the Monte Carlo, linearity and gain calibration.

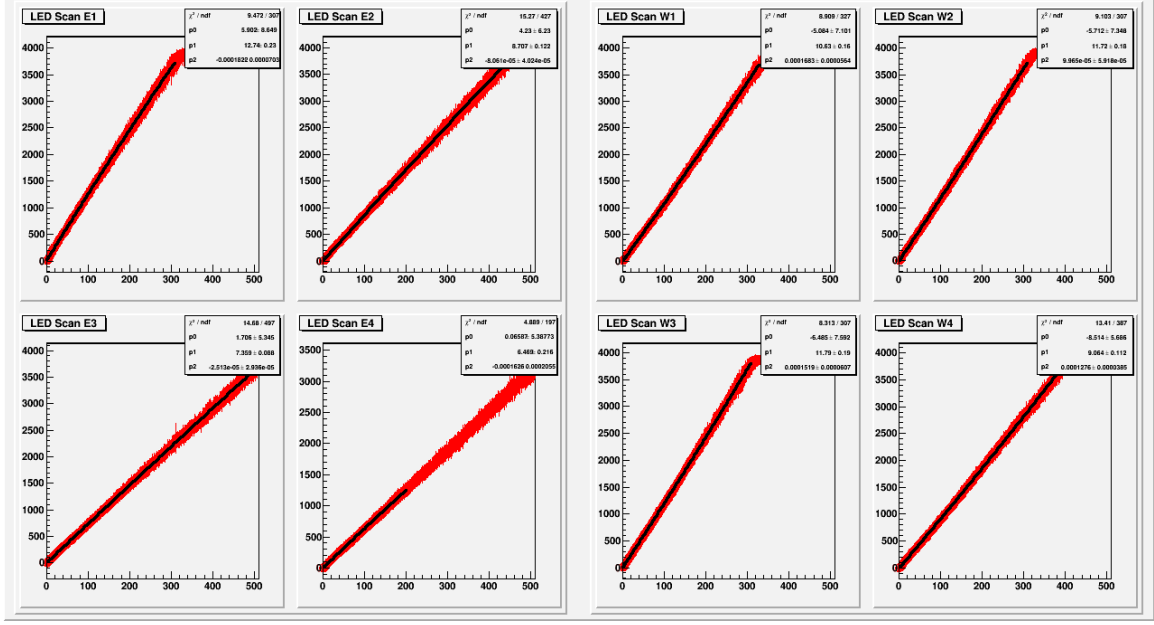


Figure 7.4. The linearity of an hour long run. The fit shows that these data are linear to 0.3%.

## 7.2 Overview of Analysis Procedures

As described in section 7.1, the UCNA experiment is a prime example of a parity-violating asymmetry in beta decay spectrum measurement. Here we develop techniques for constructing the experimental observable used to extract the  $b$  correlation with minimum systematic bias. This involves finding a quantity that cancels out the dependence of the spectrum on  $A$  which is treated like an unknown if  $A$  and  $b$  are to be determined independently. To find this quantity, which we will call the super sum, we must first develop a model of the rates measured in each detector for each spin state. This model must, at the minimum, account for the asymmetry,  $A$ , the detector efficiencies, and UCN loading efficiencies, all of which are major systematic effects.

### 7.2.1 Rate Model

In the UCNA apparatus, we measure four rates that depend on neutron spin and the polarity of the magnetic field of the detector. These rates, along with the asymmetry and

Fierz term,  $A$  and  $b$ , are

$$\begin{aligned} r_1^\uparrow &= \eta_1 n^\uparrow (1 + bx^{-1} + A_0 y) \Gamma_{SM}, & r_2^\uparrow &= \eta_2 n^\uparrow (1 + bx^{-1} - A_0 y) \Gamma_{SM}, \\ r_1^\downarrow &= \eta_1 n^\downarrow (1 + bx^{-1} - A_0 y) \Gamma_{SM}, & r_2^\downarrow &= \eta_2 n^\downarrow (1 + bx^{-1} + A_0 y) \Gamma_{SM}, \end{aligned} \quad (7.1)$$

where we have defined

$$x(E) \equiv \frac{E}{m_e}, \quad \text{and} \quad y(E, \theta) \equiv \langle P \rangle \beta \cos \theta, \quad (7.2)$$

where  $\langle P \rangle$  is the average polarization. These four rates are expressed in terms of the detector efficiency,  $\eta_{1,2}(E, \theta)$ . The UCN loading number for each spin state,  $n^\uparrow$  and  $n^\downarrow$ , which varies on order of a factor of 2, are independent of  $E$  and  $\theta$ , as the UCN physics is highly decoupled from the beta decay physics. Also, these rates involve the neutron lifetime and the differential decay rate as a function of energy as predicted by the Standard Model,

$$P_{\text{SM}}(E) = \tau_n \Gamma_{\text{SM}}(E). \quad (7.3)$$

The detector efficiencies are typically both near unity at  $E > 200$  keV, but fall to zero at lower energies near some cutoff,  $E_{1,2}^{\text{off}}$ . This cutoff will typically differ for each detector, introducing differences near cutoffs. The differences create a more complex cutoff function unless there is a way to extract the geometric mean in the beta spectrum. We will show a way to do this in section 7.2.2.

### 7.2.2 Asymmetry and Energy Spectrum

A simple asymmetry, which neglects detector and loading efficiency effects, as measured by two detector rates  $r_1$  and  $r_2$ , is given by

$$A = \frac{r_1 - r_2}{r_1 + r_2}, \quad (7.4)$$

where the total rate  $R$  and total counts  $N$  are fixed,

$$R = r_1 + r_2 = \frac{N}{T} \pm \frac{\sqrt{N}}{T}, \quad (7.5)$$

and if run for a total time period  $T$  will have error

$$\sigma_A^2 = \left( \frac{\partial A}{\partial r_1} \right) \sigma_{r_1}^2 + \left( \frac{\partial A}{\partial r_2} \right) \sigma_{r_2}^2 = \frac{4r_1r_2}{TR^3}. \quad (7.6)$$

However, detector efficiencies and neutron loading efficiencies can lead to large biases. This leads us to use a method for extracting  $A$  with a formula that canceled some of the detector and loading effects. One such formula is the super ratio.

We can divide out the detector and loading efficiencies with the dimensionless quantity called the super ratio [95] [96],

$$S(E, \theta) = \frac{r_1^\uparrow r_2^\downarrow}{r_2^\uparrow r_1^\downarrow}. \quad (7.7)$$

Using our rate model, we can derive

$$S(E, \theta) = \left( \frac{1 + bx^{-1} - A_0y}{1 + bx^{-1} + A_0y} \right)^2. \quad (7.8)$$

Assuming that the detector efficiency is independent of the spin state, the super ratio can be used to find the true asymmetry,  $A$ , which is independent of the loading and detector efficiencies, but which is not independent of the Fierz parameter,  $b$ ,

$$A(E, \theta) = \frac{1 - \sqrt{S}}{1 + \sqrt{S}}. \quad (7.9)$$

Assuming the rate model in equation (7.1) we obtain

$$A(E, \theta) = \frac{A_0y}{1 + bx^{-1}}. \quad (7.10)$$

If we were to use this to fit both  $A$  and  $b$  at the same time, we would obtain [26],

$$\sigma_A = \frac{14.8}{\sqrt{N}}, \quad \sigma_b = \frac{206}{\sqrt{N}}. \quad (7.11)$$

If we can fix  $b$ , we reduce the error on  $A_0$  considerably down to

$$\sigma_A = 14.8 \sqrt{\frac{1 - \rho^2}{N}} = \frac{2.7}{\sqrt{N}}, \quad (7.12)$$

where  $\rho = -0.983$  [26].

In order to extract the Fierz term from a beta decay electron energy spectrum, we need to find the ratio between the measured spectrum  $P_e(E)$  and the spectrum expected from the Standard Model,  $P_{\text{SM}}(E)$ . This Fierz ratio is defined as

$$R_F(E) = \frac{P_e(E)}{P_{\text{SM}}(E)} = \frac{1 + b \frac{m_e}{E}}{1 + b \langle \frac{m_e}{E} \rangle}. \quad (7.13)$$

To find this ratio from the UCNA experiment, it is helpful to extract a spectrum that does not have a significant dependence on  $A$ . We can use a formula called the super sum to do this. We can construct the super sum as the arithmetic mean of the geometric means of the spin/detector pairs. Just as we took the asymmetric component of the super ratio by dividing the difference of these pairs by the sum, here we just use the sum to preserve the symmetric component, which reduces to the spin symmetric term,

$$\Sigma(E, \theta) dE \equiv \frac{1}{2} \sqrt{r_1^\uparrow r_2^\downarrow} + \frac{1}{2} \sqrt{r_2^\uparrow r_1^\downarrow}, \quad (7.14)$$

where in the above rate model we have

$$\Sigma = \sqrt{\eta_1 \eta_2 n^\uparrow n^\downarrow} (1 + bx^{-1}) \Gamma_{SM}. \quad (7.15)$$

While this does not eliminate the detector efficiencies, it does remove any dependence on  $A$  from the extraction of  $b$  like a proportionality constant in front of the differential rate. This does not affect the overall shape of the spectrum, and when we go to normalize the spectrum in  $P(E) dE$ , this term drops out completely. We can then estimate the error on  $\sigma_\Sigma$  in terms of the total counted events for each spin state,  $N^\uparrow$  and  $N^\downarrow$ ,

$$\frac{\sigma_\Sigma}{\Sigma} = \frac{1}{2} \sqrt{\frac{1}{N^\uparrow} + \frac{1}{N^\downarrow}}. \quad (7.16)$$

### 7.3 Estimation of Systematic Errors on $b$ from UCNA

In this section we examine several systematic effects that arise when attempting to extract  $b$  from a beta decay spectrum. In order to determine what systematic effects to investigate, we must discuss how a real detector varies from an idealized one. A real detector will have a finite resolution in energy and angle. Even once we have a probability distribution function,  $P(E)$ , there will be some convolution function,  $f(E; E')$ , that will blur the probability

function, decreasing the effective resolution. This will of course decrease the ability to extract beta decay parameters, such as  $A$  and  $b$ , which depend on the spectral shape. Our intuition tells us that  $b$  will suffer more, but let us investigate that possibility.

Another concern is that the  $A$  and  $b$  terms are both affected by angle. The angle term,  $y$ , that appears in our rate model has a  $\cos \theta$  dependence that controls the asymmetric part of the rates. Typically, the angle itself cannot be measured and must be integrated away. This integration also has a convolving effect, particularly on  $A$  as it dilutes the asymmetry. The effect is not limited to  $A$ , as angular effects from backscattering, foil absorption, and magnetic field effects, all conspire to affect the  $b$  extraction as well.

A true distribution where all effects are mixed into one term would be the integrals,

$$\begin{aligned} r_1^\uparrow(E) &= n^\uparrow \int \eta_1(E; E', \theta') \Gamma_{bA}^+(E', \theta') dE' d\theta', \\ r_2^\uparrow(E) &= n^\uparrow \int \eta_2(E; E', \theta') \Gamma_{bA}^+(E', \theta') dE' d\theta', \\ r_1^\downarrow(E) &= n^\downarrow \int \eta_1(E; E', \theta') \Gamma_{bA}^+(E', \theta') dE' d\theta', \\ r_2^\downarrow(E) &= n^\downarrow \int \eta_2(E; E', \theta') \Gamma_{bA}^+(E', \theta') dE' d\theta', \end{aligned} \quad (7.17)$$

where we have defined,

$$d\Gamma_{bA}^\pm \equiv (1 + bx^{-1} \pm Ay) d\Gamma_{SM}. \quad (7.18)$$

It is clear that there is no impact on the super sum and super ratio from the spin state occupancy, and these will cancel out as before. The effect of the convolution is more subtle, however. There is unlikely to be a simple closed form expression for  $\eta_i(E; E', \theta')$ , but we can assume that it is separable into three parts: a detector energy response function (an angle dependent backscatter and dead layer effect)  $\eta^r$ ; a threshold function from real detector efficiency as a function of energy  $\eta^{\text{th}}$ ; and a PMT response function  $\eta^{\text{pe}}$ . The latter is typically dominated by a Poisson function, from the finite nature of the number of photoelectrons. These separable terms can be integrated in three stages,

$$\eta(E; \theta', E') = \int \eta^{\text{pe}}(E, E''; \mu_i) \eta^{\text{th}}(E''; \mu_j) \eta^r(\theta', E'; \mu_k) dE''. \quad (7.19)$$

While no exact closed form expression for any of these components likely exists, we may easily make some helpful approximations of the three functions, which certainly are a rea-

sonable approximation, by comparison, to the data.

### 7.3.1 Analytical Detector Model

The angle and backscatter smearing function,  $\eta^r$ , should have a smaller width when backscatters are summed together as the energy from the detector on each side should be better accounted for. However, the detector energy response function still exists due to dead layer effects. In our analysis, we will eliminate most backscattered events from the data stream as we can cut out events that fire on both detectors. Looking back at equation (7.19), the detector backscatter response functions can be approximated by the simplifying exponential function

$$\eta^r(E; E', E_{\text{tail}}) \approx \begin{cases} E^{\text{tail}} e^{-(E-E')/E^{\text{tail}}} & E < E', \\ 0. & \end{cases} \quad (7.20)$$

While our backscatter may be well approximated by an exponential, a more realistic model is the convolution of a Gaussian with a exponential,

$$\eta^r(x; \lambda, \sigma) = \frac{1}{\sqrt{8\pi}\lambda} \int_{\lambda}^{\infty} e^{y/\lambda - 1} e^{-(x-y)^2/2\sigma^2}. \quad (7.21)$$

This gives the basis for our response functions,

$$\eta^r(x; \lambda, \sigma) = \exp\left(\frac{\sigma^2}{2\lambda^2} + \frac{x}{\lambda} - 1\right) \operatorname{erfc}\left(\frac{\sigma^2 + \lambda(x-\lambda)}{\sqrt{2}\lambda\sigma}\right). \quad (7.22)$$

A plot of a family of these functions is shown in figure 7.5(a). The value of these functions is that they are simple representations of resolution caused by backscattered electrons and other effects. The skew component is for backscatter like effects. The resolution function has a sharp full energy edge for electrons that have no backscatter, and then a decaying lower energy tail due to energy loss in backscattered electrons. The symmetric part is for other resolution widening effects such as from electronic noise and shot noise. The resolution component of our toy model can be expressed as a Poisson distribution,

$$\eta_{1,2}^{\text{pe}}(E, E') = \frac{\mu_k^x e^{-\mu}}{\Gamma(x+1)}, \quad (7.23)$$

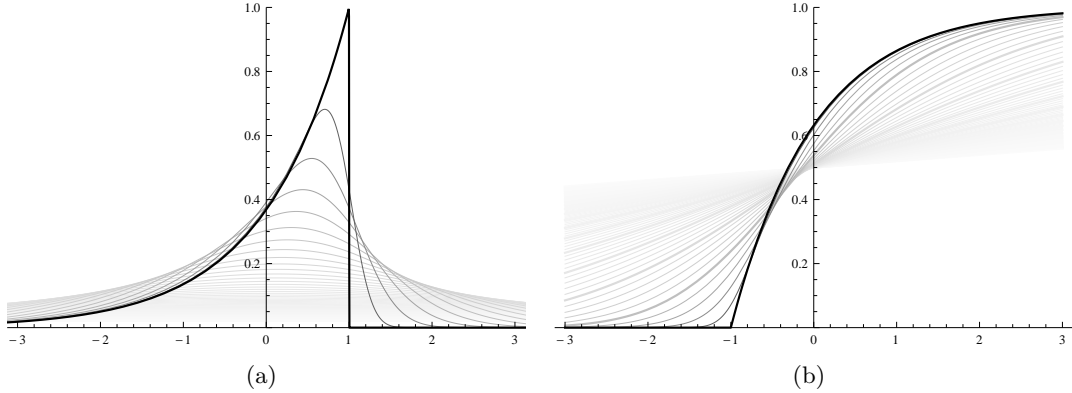


Figure 7.5. (a) A plot of the family of functions in equation (7.22) for  $\sigma = 1$ ,  $\lambda \in \{0, 1/5, 2/5, \dots\}$ . (b) A plot of the family of threshold functions in equation (7.25) also for  $\sigma = 1$ ,  $\lambda \in \{0, 1/5, 2/5, \dots\}$ .

where

$$x \equiv \frac{E - E'}{E_k^{\text{pe}}}. \quad (7.24)$$

The next part of our toy can be modeled by

$$\eta^{\text{th}}(x; \lambda, \sigma) = \frac{1}{2}\eta(x; \lambda, \sigma) - \frac{1}{2}\text{erf}\left(\frac{\lambda - x}{\sqrt{2}\sigma}\right), \quad (7.25)$$

which can serve as a quite reasonable detector response function,  $\eta^{\text{th}}(E; \mu_i)$ . A family of threshold functions are shown in figure 7.5(b). A threshold function describes the falloff of events at low energy due to detector thresholds. At low energy, electrons are not able to penetrate the detector. They are scattered, slowed, or stopped such that they do not register either in the wirechamber or in the scintillator below a cutoff energy. Further, the threshold function is not a sharp edge but has an asymptotic tail from the cutoff to higher energies as higher energy electrons are more likely to punch through the detector dead layers and be detected. Also, the cutoff is not completely a sharp edge on the low energy side due to resolution and other broadening effects. Equation (7.25) serves as a good approximation of both these effects. Simple Monte Carlo experiments show this effect does not strongly influence  $b$  extraction because the impact of the cutoff falls off exponentially at higher energies so we will ignore this effect for sufficiently high software threshold. Thus, a suitable energy range can be chosen that is above the cutoff so as to render no sizable effect on the spectral shape. Typically, the threshold cutoff is approximately 70 keV with a energy range starting at 150 keV. The tail, or skewness of the response function distribution

did not show a significant effects in the first Monte Carlo studies so in further studies, we neglect it in favor of a simpler symmetric distribution.

### 7.3.2 Backscatter Effects on Asymmetry and $b$ Extraction

In the UCNA experiment, there exists a problem of multiple foils between the detector and the fiducial volume where UCN decay. This means that not all emitted electrons make it through the foils, at least not on the first pass. A fraction of the electrons are backscattered, while others are fully absorbed. Either way, the asymmetry is diluted by this effect. To extract the physics asymmetry, this must be corrected. Knowing exactly what is the scale of this correction, is a challenge. As this does not affect the extraction of  $b$ , we remove discussion to an appendix. See appendix C for a discussion of effect of backscattering as a function of foil thickness on the asymmetry.

For  $b$  extraction, we use events that do not detectably backscatter by software cutting on events that do not register in both detectors. Later, we will compare only these non-backscattering events to similar event types in a physics Monte Carlo. The effect of ignoring backscattering events is only to add to the energy response width of the tail function. We investigated this by including events that register in both detectors, but this effect is small since double detector events account for only 3% of all events. Even a  $b$  of 0.1 would have only a  $\delta b = 0.003$  contribution to the total extraction. In the final analysis we cut out these events.

### 7.3.3 Biased Polarization

In section 7.2.1, our model for detector rates assumed that the polarization of neutrons was the same for both spin states. For the real experiment, this may not be the case. Here we study the size of this effect. An important systematic effect to analyze for its corrections on the extraction of  $A$  and  $b$  is that of polarization that is imperfect, or biased toward one spin type. A real neutron polarizer may introduce a biased polarization vector for the two different UCN spin loading types,

$$\langle P \rangle \neq \pm 1. \quad (7.26)$$

Instead, we introduce a small polarization component that is spin dependent,

$$\begin{aligned}\langle P \rangle_{1,2}^{\uparrow} &= \pm(p + \delta), \\ \langle P \rangle_{1,2}^{\downarrow} &= \mp(p - \delta).\end{aligned}\tag{7.27}$$

In this case, we recover

$$\begin{aligned}r_{1,2}^{\uparrow}(E) &= \eta_{1,2} n^{\uparrow} [1 + bx^{-1} \pm (p + \delta)Ay] \Gamma_{\text{SM}}, \\ r_{1,2}^{\downarrow}(E) &= \eta_{1,2} n^{\downarrow} [1 + bx^{-1} \mp (p - \delta)Ay] \Gamma_{\text{SM}}.\end{aligned}\tag{7.28}$$

Plugging this into the super sum, we find only a quadratic contribution in  $\delta$  to

$$\Sigma = (1 + bx^{-1})(1 + \Delta_b) \Gamma_{\text{SM}},\tag{7.29}$$

We get the correction to the Fierz ratio

$$\Delta_b(\delta) = -\frac{\delta^2 A^2 y^2}{(1 + bx^{-1})^2 - p^2 A^2 y^2} + \mathcal{O}(\delta^4).\tag{7.30}$$

Similarly, we can apply the same method to the super ratio to extract a correction for the measured  $A$ ,

$$\frac{1 - \sqrt{S}}{1 + \sqrt{S}} = \frac{Ay}{1 + bx^{-1}} (1 + \Delta_A).\tag{7.31}$$

The asymmetry is corrected with

$$\Delta_A(\delta) = \frac{\delta^2 p A^2 y^2}{(1 + bx^{-1})^2 - p^2 A^2 y^2} + \mathcal{O}(\delta^4).\tag{7.32}$$

We find that both  $\Delta_b$  and  $\Delta_A$  are second order in  $\delta$ . For UCNA,  $\delta < 1\%$  so  $\Delta_A, \Delta_b \approx 10^{-6}$ . These are small enough effects to be neglected.

### 7.3.4 Simulation Study of Systematics

Presented in this section are the results of a series of Monte Carlo studies of key systematic effects. As this analysis is basically a study of the electron energy distribution, the major factors influencing this are detector energy response, detector background and backscattering effects. Backscattering was discussed in section 7.3.2. Here we address the other systematic sources of error. The effects examined were detector gain, detector linearity in

second and third order, energy resolution, and background subtraction mismatch. As shown in the previous section, it is possible to construct a toy model of the effects produced by the full physics Monte Carlo. The toy model can be altered with the systematic effects listed above, without the need for the full physics simulation. The advantage of this method, is that we can vary the parameters,  $\mu_i$ , in the model, and quantify the effect on the error in  $b$  as well as determine the  $\chi^2/\text{ndf}$  values for the fit to the Fierz ratio,  $R_F$ . The procedure used changed the value of the parameter being tested,  $\mu_i$  while keeping  $\chi^2/\text{ndf} < 2$ . These maximum values are also consistent with the response and background systematic uncertainties from the full UCNA analysis. Also, to be consistent with the UCNA data, the same number of events, 25 million, was used. A combination of these values sampled from an appropriate distribution, was used randomly multiple times to determine the effective average error on  $b$ . This allows us to build a covariance model of the parameters without the need for lengthy physics Monte Carlo, which can take minutes per event [97]. Some of the parameters are correlated, so a change in two parameters at the same time may inversely or identically alter  $b$ , rather than any one change in a single parameter by itself. For example, many parameters spread the resolution width, so changing one has a nearly identical effect as another. Both spread the resolution in the energy range by some amount in the same direction. Conversely, some parameters are inversely related, such as energy offset and cutoff energy. A change in one can be offset by a change in the other.

We began the study by testing for the extraction of  $b$  without altering any parameters of the analytical model. This acted as a control test to see what value of  $b$  would arise from the Fierz ratio of the control Monte Carlo to another control with  $b = 0$ . Then we fit the curve

$$\frac{1 + bx^{-1}}{1 + b \langle x^{-1} \rangle} \quad (7.33)$$

to this ratio, and extracted  $b$  from the fit. Three values of  $b$  were simulated,  $b = 0, \pm 0.05$  and these were compared to a Monte Carlo of a null  $b$ . Figure 7.6(a)–7.6(c) show this control study.

The nonlinearity of the detectors response was then investigated by taking the Fierz ratio of a simulated set of data with  $b = 0, \pm 0.05$ . To characterize the nonlinearity, we introduce a quadratic and quartic nonlinearity function

$$\delta x = -1.71\alpha(x - a)(x - b) + 5.86\beta(x - a)(x - (a + b)/2)(x - b), \quad (7.34)$$

Table 7.1. A summary of numerical systematic studies

parameter	$\mu_i$	$\delta\mu_i$	$b$	fit $b$
control	none	0	-0.05	-0.054(2)
			0.0	-0.004(2)
			0.05	0.052(2)
quadratic	0	0.007	-0.05	-0.037(4)
			0.0	0.084(3)
			0.05	0.133(3)
quartic	0	0.003	-0.05	-0.076(5)
			0.0	-0.025(5)
			0.05	0.030(5)
resolution	0.05	0.005	-0.05	-0.059(2)
			0.0	-0.006(2)
			0.05	0.043(2)
endpoint	2.53	0.005	-0.05	-0.044(5)
			0.0	-0.054(5)
			0.05	0.100(5)
background	0	0.002	-0.05	-0.055(5)
			0.0	-0.000(4)
			0.05	0.046(5)

where  $a$  and  $b$  are the starting point and endpoint and  $x = E/m_e$ . A plot of this linearity map is shown in figure 7.7 where the influence of the parameters on the nonlinearity can be seen in an exaggerated manner. In these studies, we first varied the  $\alpha$  parameter with the maximum value of  $\alpha = 3.6\text{keV}/m_e$ . Figure 7.8(a)–7.8(c) show an study where the second order linearity is tested by varying the  $\alpha$  parameter in the energy distortion function

Similarly to the quadratic nonlinearity study, the third order parameter was varied to determine the impact of higher order nonlinearity. Figure 7.9(a)–7.9(c) show distortion experiments using the same distortion function as above but varying the  $\beta$  parameter such that  $\beta = 1.0 \text{ keV } /m_e$  at maximum.

Another study was performed by varying the resolution of the detectors. Detector resolution was varied in a simple Gaussian model and then the Fierz parameter, extracted. Figure 7.10(a)–7.10(c) show variation of the width by 10% from  $\sigma = 0.05$  to  $\sigma = 0.055$  in dimensionless units. This is equivalent to a resolution width of 51 and 56 keV respectively. Even though the real resolution is a function of energy such as the  $\propto \sqrt{E}$  due to the shot noise effect, for this study it was held constant. The detailed Monte Carlo showed the true  $E$  dependence had a negligible effect.

Figure 7.11(a)–7.11(c) show variation in the end point by 2.5 keV such that  $x'_0 = 0.998x_0$ . This works out to a gain shift of 0.3% which is consistent with the gain stabilization of the real data set.

Figure 7.14(a)–7.14(c) show an example where an artificial background is introduced. The background has the toy fourth-order spectral shape shown in figure 7.12. The toy background captures the two important features of the real background, shown in 7.13 [97], of gammas in the low energy regime and muon background toward high energy. The amplitude of background variation is  $\approx 0.2\%$  overall which is 10% of the total size of the background noise to signal which for UCNA is 2%.

Figure 7.15(a)–7.15(c) show a single example of a combination of randomly generated values of all parameters about the center values used in the previous experiments. The random values are generated using a Gaussian distribution such that the values used above are one standard deviation. Based on these studies where 100 separate parameter values were sampled, we compute a total systematic error of  $\sigma_b = 0.08$ .

## 7.4 Results from UCNA data

Presented in this section are the results of the UCNA 2010 data set compared to physics Monte Carlos and the systematic studies mentioned in the previous section. Two Monte Carlos were used to compare to UCNA data. One Monte Carlo was written using the GEANT4 toolkit [98] and was developed by Dr. J. Liu and graduate student M. P. Mendenhall [96,97]. The other was written using the PENELOPE [99], developed by graduate student (now Dr. R. Pattie [95]. Shown in figure 7.16 are the super sums of both data from the UCNA 2010 run and the full GEANT4 electron physics Monte Carlo with the residuals shown in figure 7.17. Shown in figure 7.18 are the super sums of both data from the UCNA 2010 run and the full PENELOPE Monte Carlo with the residuals shown in figure 7.19.

The gray bands in figure 7.20 and 7.21 represent the systematic error of a null result consistent with  $b = 0$ . The band is computed using an envelope of approximately 70% of Monte Carlo curves generated from the toy model used in the previous section. These results show that a best fit to the GEANT4 calculated Fierz ratio,  $R_F$ , of the fit function

$1 + bm_e/E - \langle m_e/E \rangle$ ) gives

$$b_n = 0.079 \pm 0.005(\text{stat}) \pm 0.080(\text{sys}), \quad (7.35)$$

and from PENELOPE gives

$$b_n = 0.095 \pm 0.005(\text{stat}) \pm 0.080(\text{sys}). \quad (7.36)$$

Averaging these, the systematic error in equations (7.35) and (7.36) give us a limit on  $-0.044 < b_n < 0.218$  (90% C.L.).

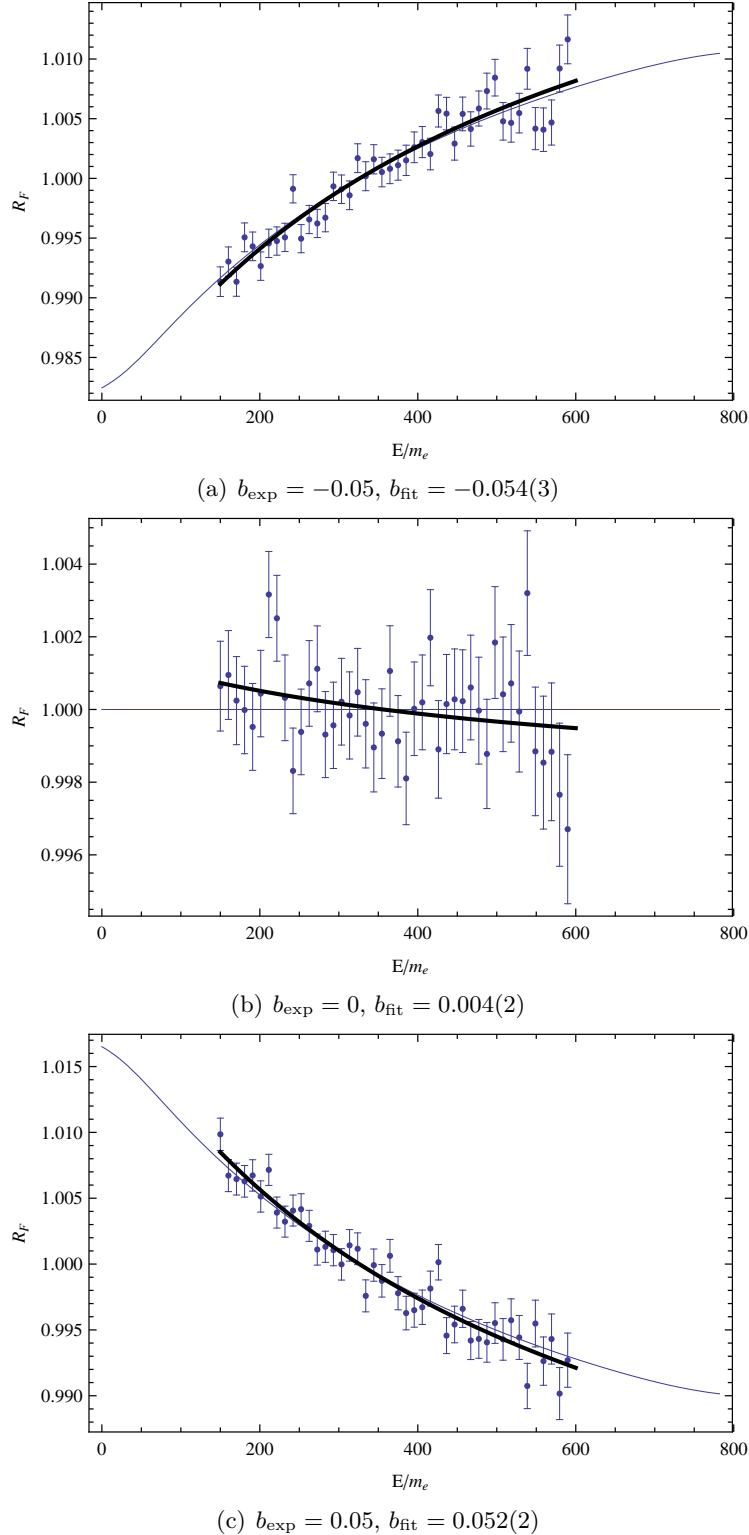


Figure 7.6. These plots show the results of three control studies. In each test, we have set  $b = 0$  and  $\pm 0.05$ . The Fierz ratio was computed and plotted by dividing out by a Monte Carlo spectrum with  $b = 0$ . The thin line is the analytical ratio,  $R_F$ . The thick line is the best fit to the randomly generated points shown as dots with error bars.

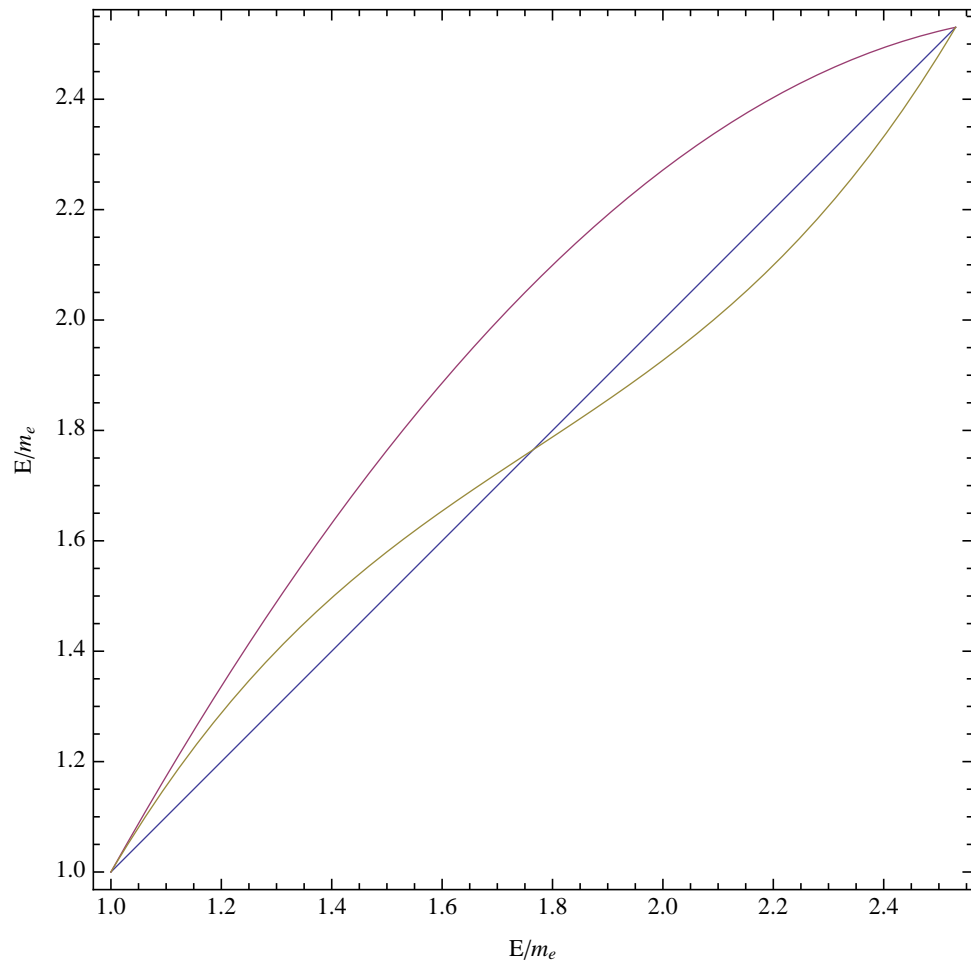


Figure 7.7. A plot of the linearity map in equation (7.34) for  $\alpha = 0.3$  (red) and  $\beta = 0.1$  (yellow) compared to linear (blue).

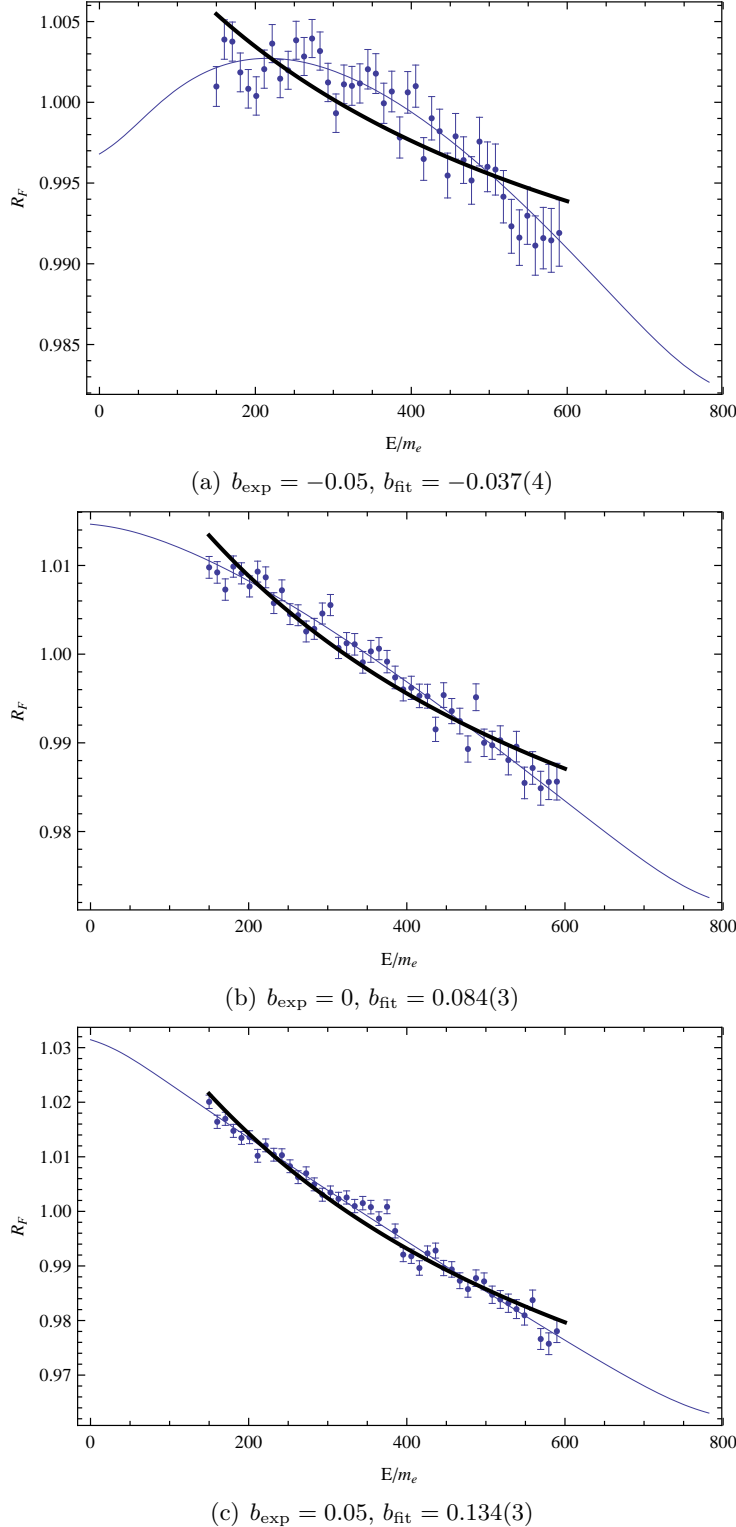


Figure 7.8. In this set of plots, we show the results of a study similar to the control test in 7.6. In this study however, a quadratic term in the linearity of the gain was varied to  $\alpha = 0.007$ . Again, Monte Carlo data with  $b = 0, \pm 0.05$  was divided by a spectrum with  $b = 0$ . The curves are the same as described in figure 7.6.

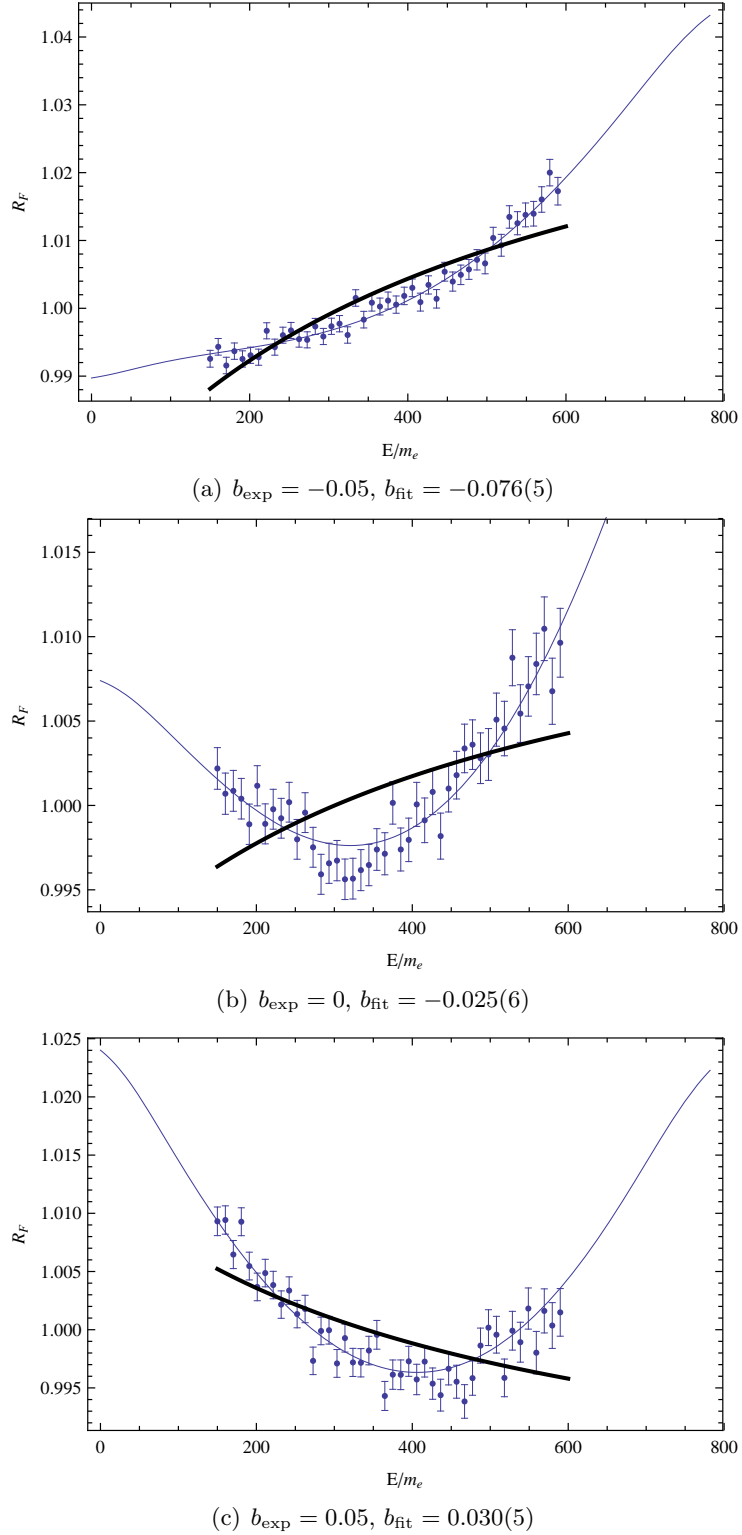


Figure 7.9. This study was similar to the nonlinearity study with a quadratic term,  $\alpha$ , except here the third order term was set to  $\beta = 0.003$ . The curves are the same as described in figure 7.6.

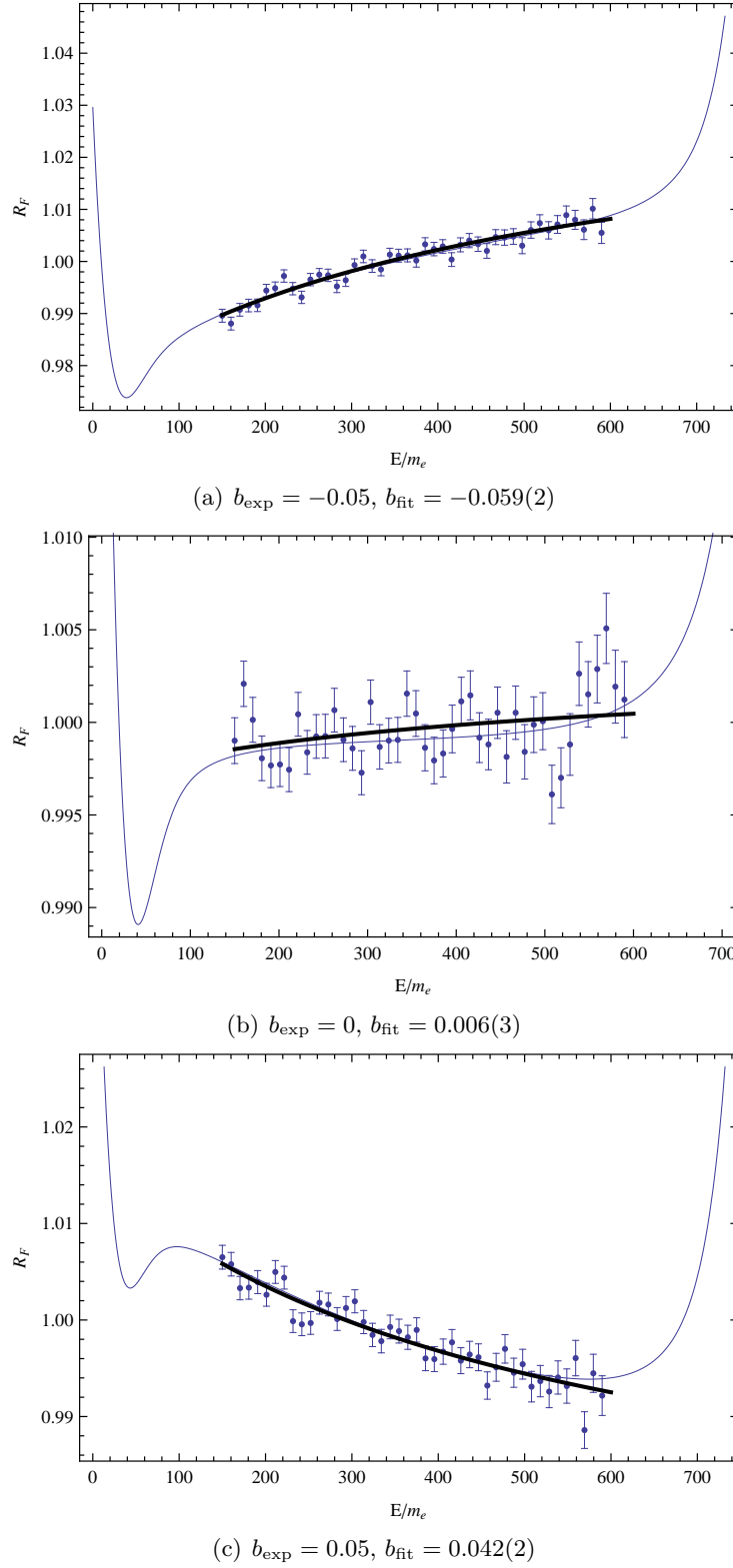


Figure 7.10. In this study, the resolution was increased by 10%. The curves are the same as described in figure 7.6.

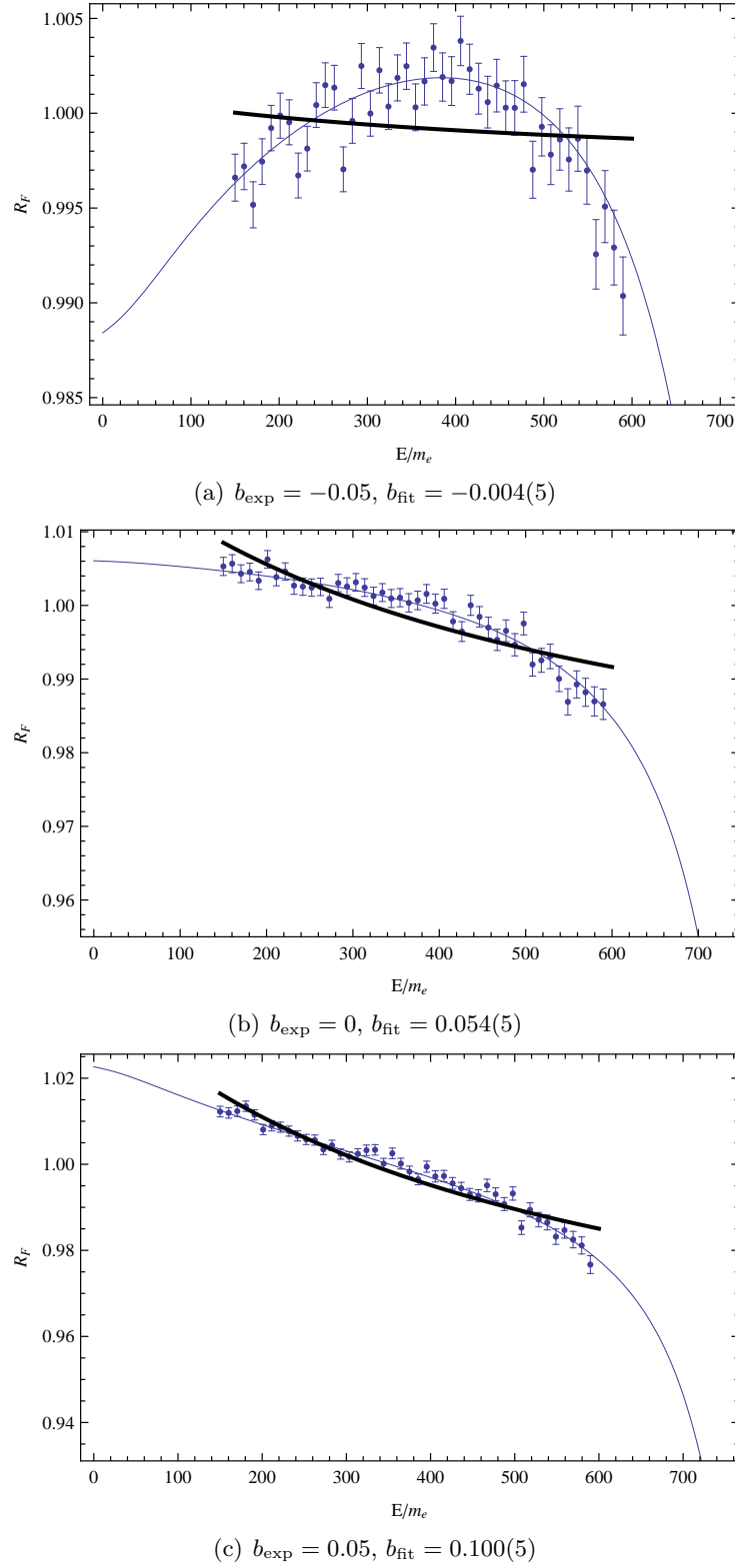


Figure 7.11. In this study, the endpoint was increased by 0.3%. The curves are the same as described in figure 7.6.

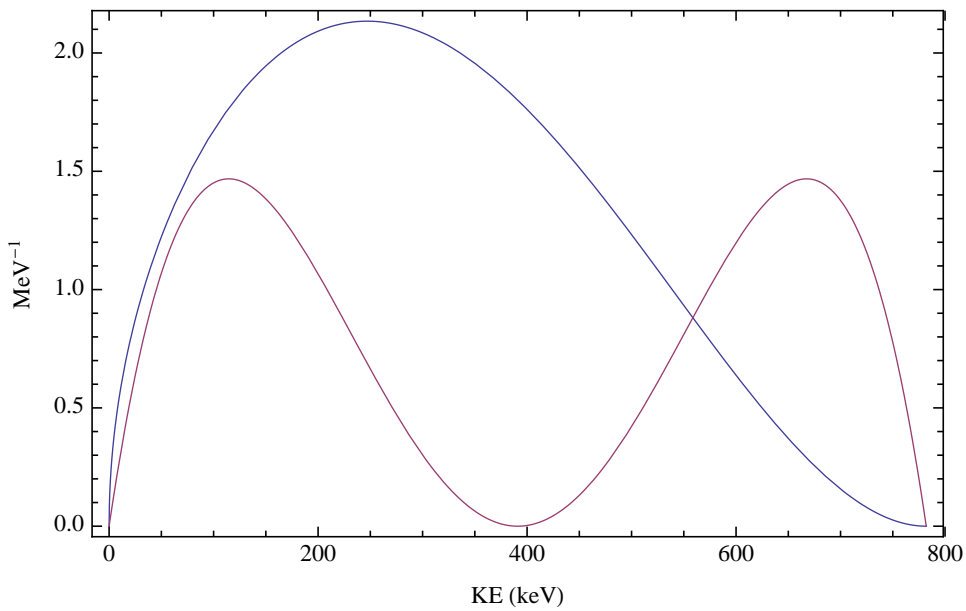


Figure 7.12. A plot of the toy background shown with a beta decay spectrum.

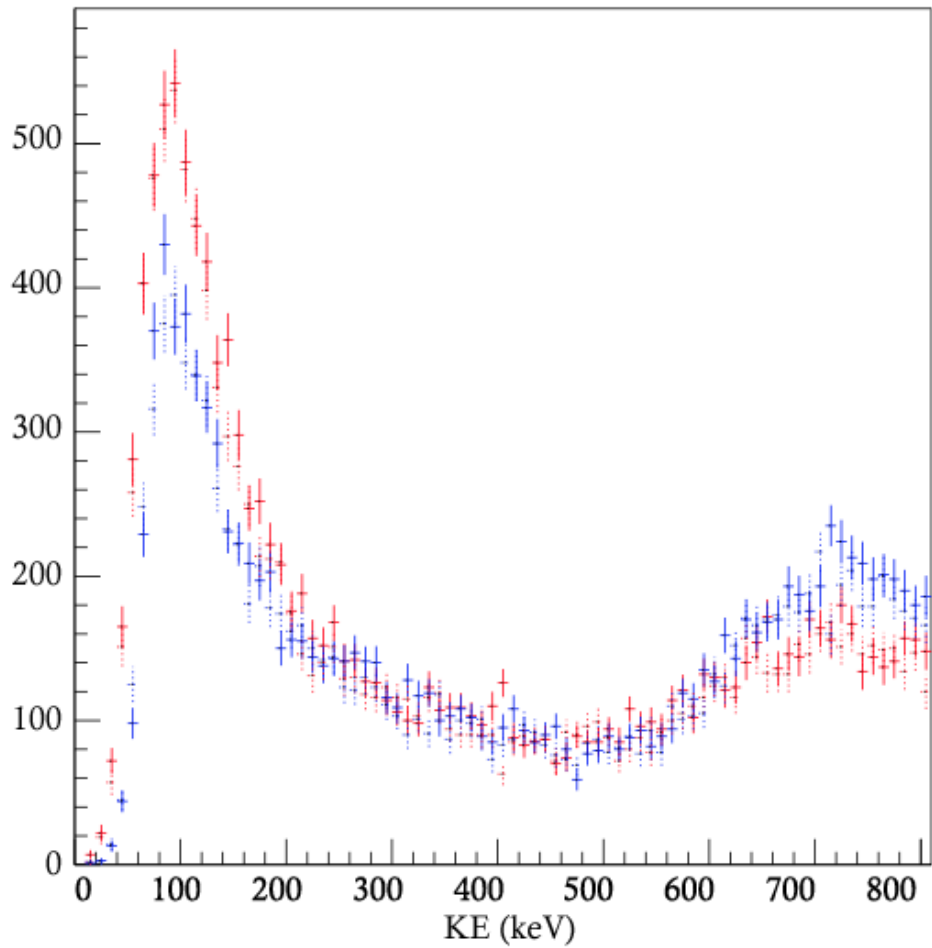


Figure 7.13. A plot of the real east and west backgrounds from UCNA 2010 data.

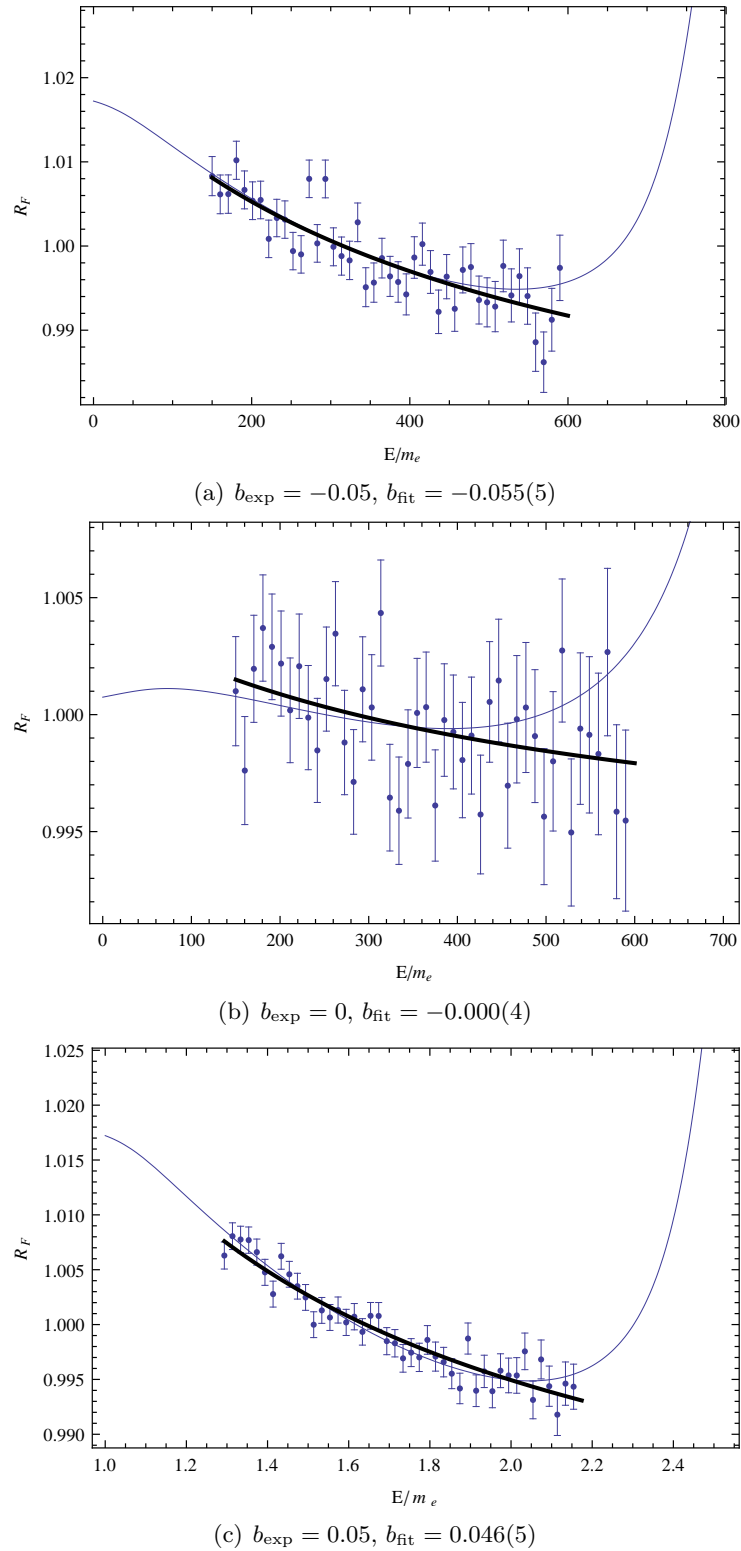


Figure 7.14. In this study, an artificial background was introduced to simulate mismatched background subtraction. The curves are the same as described in figure 7.6.

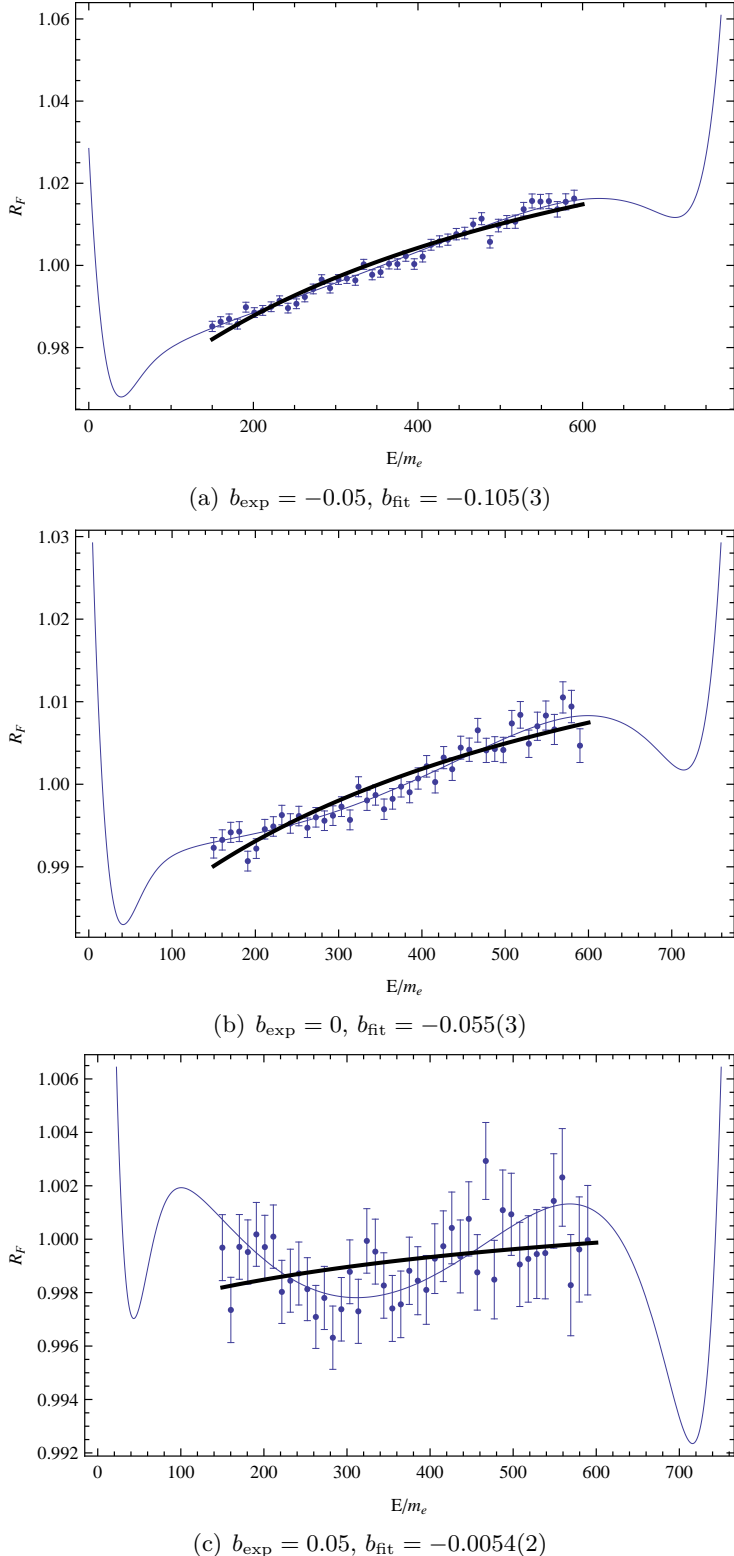


Figure 7.15. This figure show a single example of a combination of randomly generated values of all parameters about the center values used in the previous experiments. The random values are generated using a Gaussian distribution such that the values used above are one standard deviation. The curves are the same as described in figure 7.6.

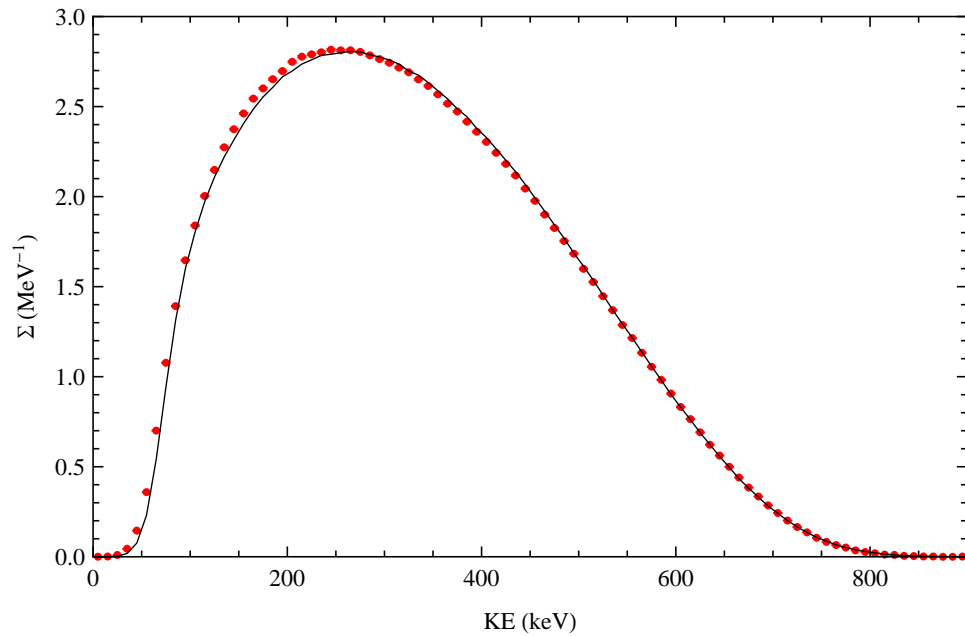


Figure 7.16. A comparison of the UCNA 2010 super sum data and the GEANT4 Monte Carlo super sum spectrum.

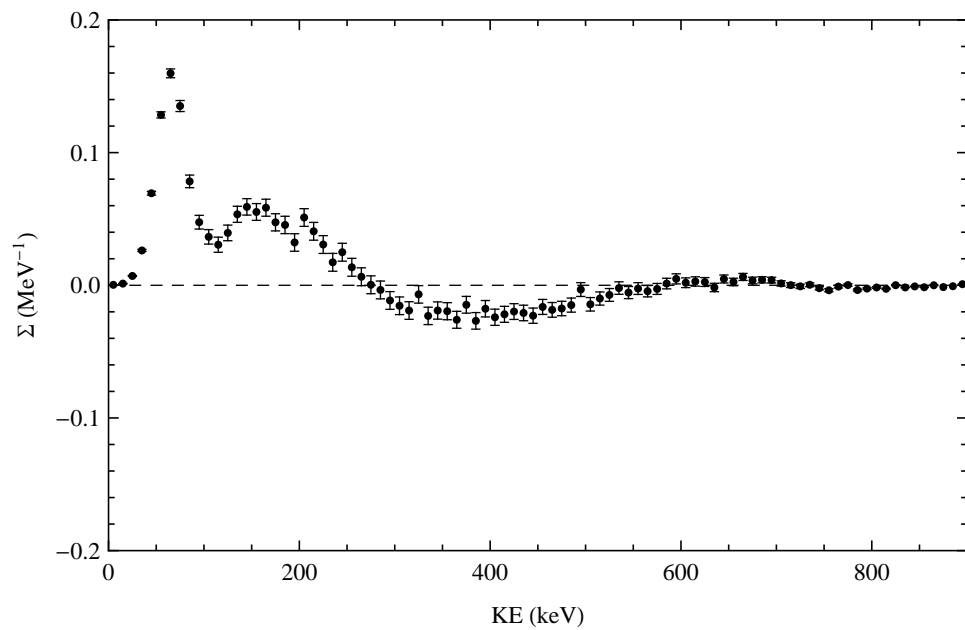


Figure 7.17. Residual of the UCNA 2010 data super sum and the UCNA GEANT4 Monte Carlo super sum.

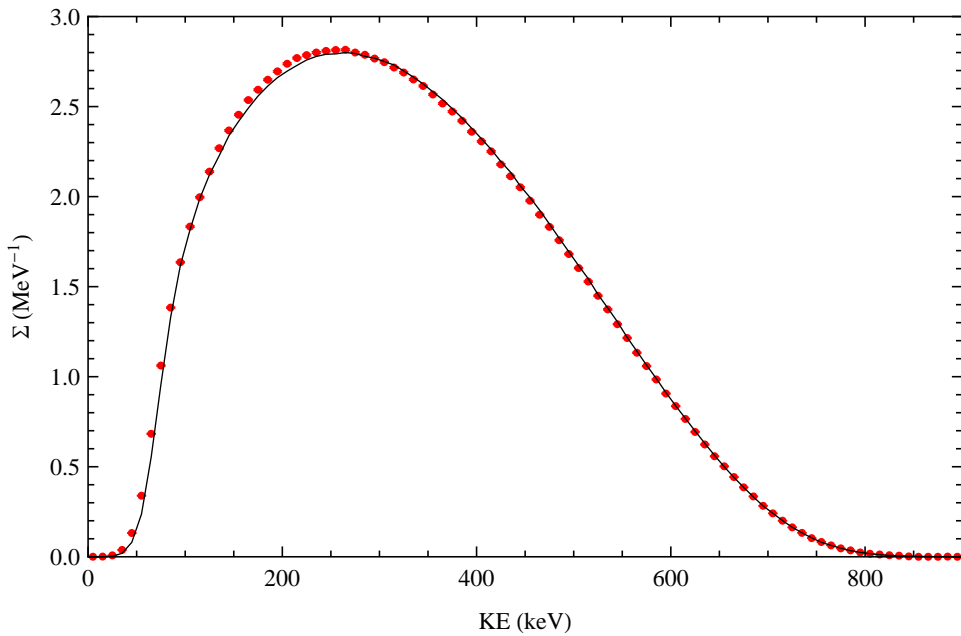


Figure 7.18. A comparison of the UCNA 2010 super sum data and the PENELOPE Monte Carlo super sum spectrum.

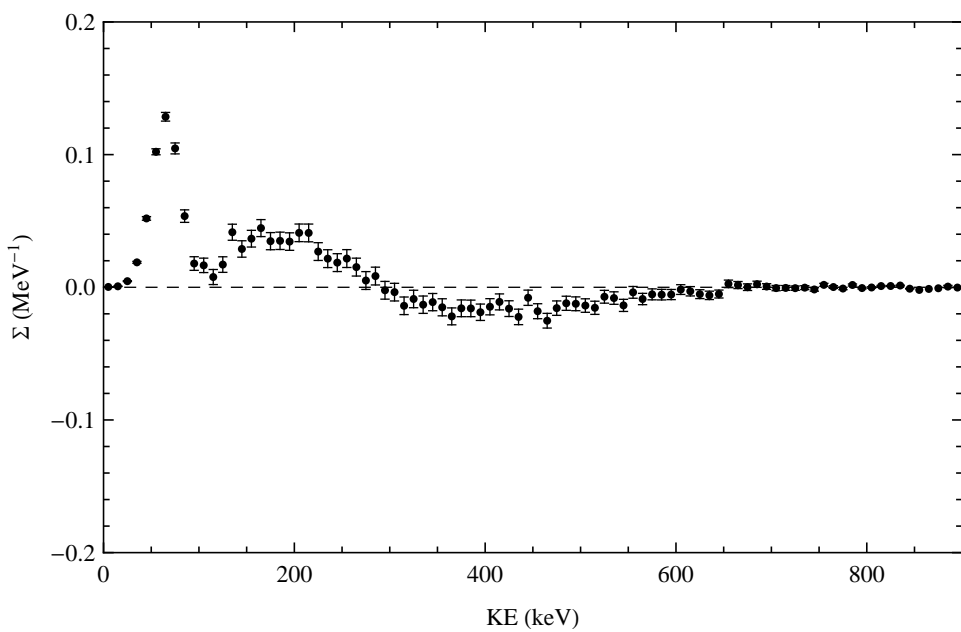


Figure 7.19. Residual of a comparison of the UCNA 2010 super sum data and the UCNA PENELOPE Monte Carlo super sum.

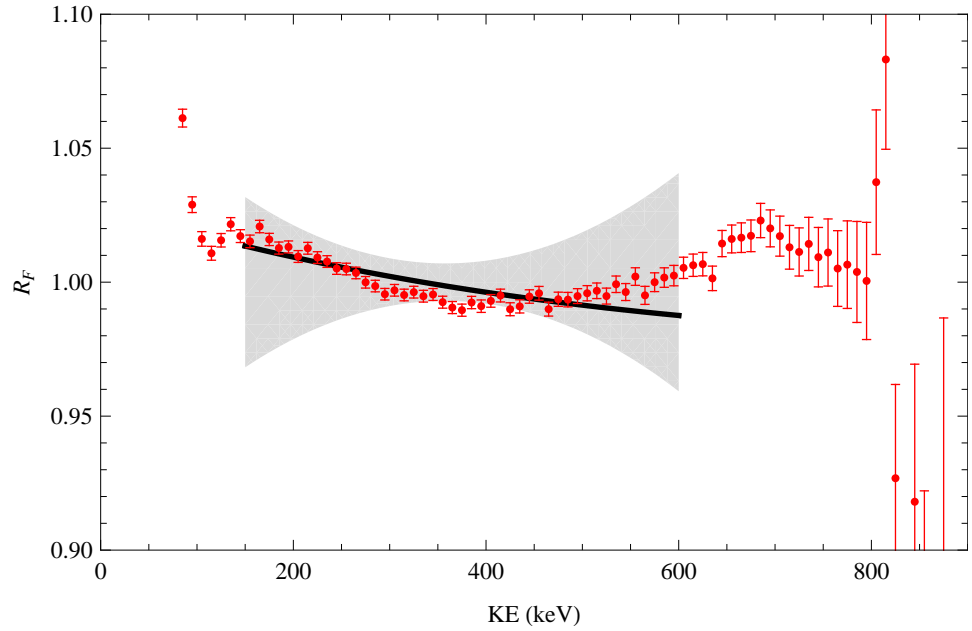


Figure 7.20. The Fierz ratio of UCNA 2010 data and the GEANT4 Monte Carlo. The dark line is the fit function  $R_F \approx 1 + b(m_e/E - \langle m_e/E \rangle)$ . The gray band represents the possible  $b = 0$  systematic  $1\sigma$  limit based on an envelope of possible Fierz ratio curves with randomly varied parameters as described in the previous section. The fit gives  $b_{\text{fit}} = 0.079 \pm 0.005$ .

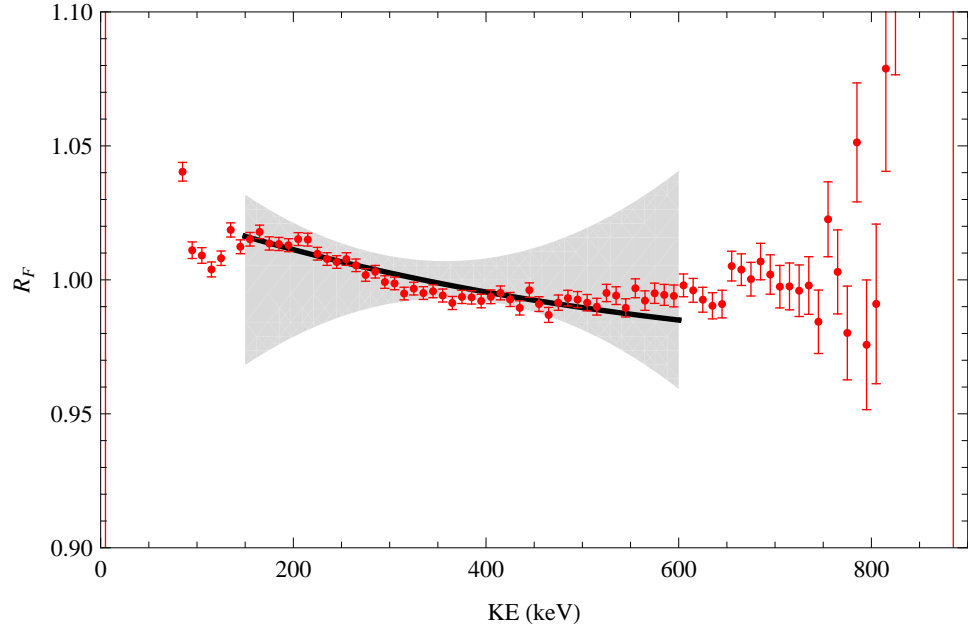


Figure 7.21. The Fierz ratio of UCNA 2010 data and the PENELOPE Monte Carlo spectrum. The dark line is the fit for the fit function  $R_F \approx 1 + b(m_e/E - \langle m_e/E \rangle)$ . The gray band represents the possible  $b = 0$  systematic  $1\sigma$  limit. The fit yields  $b_{\text{fit}} = 0.095 \pm 0.005$ .

## Chapter 8

# The UCNb Experiment

In any field find the strangest thing  
and then explore it.

---

JOHN WHEELER

### 8.1 Detector concept

The UCNb experiment started around a simple suggestion from Dr. Chris Morris that we could make an experiment that measures the neutron beta decay spectrum, to unprecedented accuracy, with a detector and UCN trap in one device. By placing a scintillating chamber that also stored neutrons at the LANL UCN source gate valve, where the density is highest [100], around 60 UCN/cc [101], we could measure the neutron electron spectrum with better statistics than any other UCN apparatus in the experimental hall. The experiment also could be modeled after an optical integrating sphere, which could measure light output from the scintillator in an position independent manner. But such an experiment would require a material that could act as an electromagnetic calorimeter and still have a high enough Fermi potential to store UCN.

Deuterated polystyrene (DPS) was a good first candidate. It has a Fermi potential of 150 neV. But it is not quite as high as the 180 neV of the stainless steel used to direct UCN to the experiment. So with DPS there could be some loss, but it is still large enough to store a significant fraction of the UCN spectrum if the entire experiment is elevated 30 mm above the main beam line. A major drawback of DPS is its very high cost. Building the entire scintillator out of DPS would be ideal from a design standpoint, but at \$1k/cc the price was prohibitive for a prototype.

Table 8.1. Possible UCNb scintillator and wall coating material choices.

scintillator	coating	$V_F$ (neV)	photons (MeV $^{-1}$ )	decay time (ns)
BC-408	BC-444	156	10,000	2
BC-444	-	156	10,000	2
CaF <sub>2</sub>	-	102	25,000	900
CaF <sub>2</sub>	MgF <sub>2</sub>	133	25,000	900
BC-408	MgF <sub>2</sub>	133	10,000	2

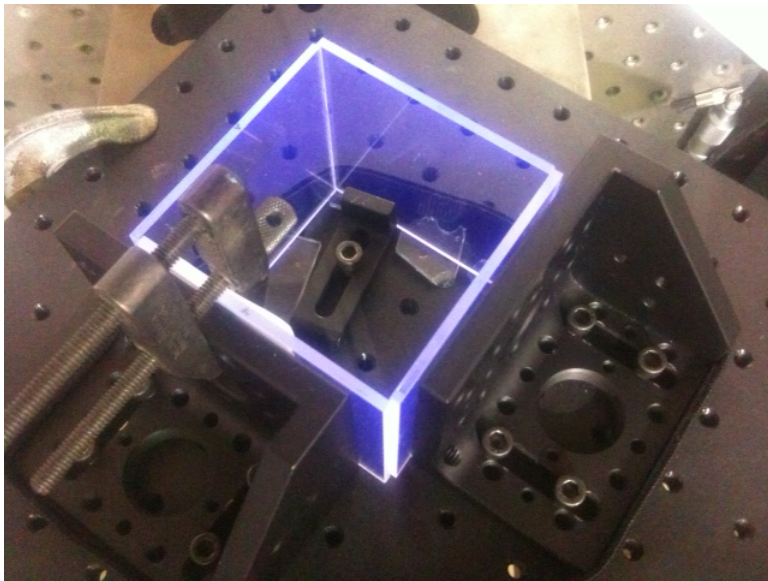


Figure 8.1. This photo shows the assembly process for the scintillator boxes used in UCNb. The boxes were locked into place with PTFE protected optical clamps mounted to an optical breadboard. The entire assembly was lifted up so that edge to be bonded would be facing as upright as possible.

Polystyrene is a good plastic scintillator. At 60% of anthracene, it outputs 10,000 photons per MeV of energy deposited [102]. This results in a resolution of 3% or 30 keV at 1 MeV.

Dr. Alexander Saunders proposed placing a thin (100  $\mu\text{m}$ ) layer of DPS on top of PS scintillator to reduce the neutron absorption losses due to the hydrogen in standard PS. The DPS would emit UV similarly to PS, but the wave shifter in the scintillator region would reemit in the visible range [103].

Other candidates were bare CaF<sub>2</sub> and MgF<sub>2</sub> on CaF<sub>2</sub>. While these scintillators do not have as high of a UCN storage potential, CaF<sub>2</sub> has a higher and more linear light yield than plastic scintillator. In the end, the best choice was MgF<sub>2</sub> because of the quality of its surface and reasonably high potential, at 133 neV. Table 8.1 shows a list of possible surface coatings and scintillator choices available to the UCNb experiment. Figure 8.1 shows a prototype CaF<sub>2</sub> box and figure 8.2 shows a prototype MgF<sub>2</sub> box.



Figure 8.2. This photo shows the  $\text{MgF}_2$  polystyrene scintillator box assembled and placed inside the integrating cube. The top is on top of the box showing the insert hole for the insertable source.

## 8.2 Modeling UCNb

### 8.2.1 The integrating sphere

An important feature of the UCNb experiment is the integrating reflector. Though actually a cube in the prototype device, the principles in modeling the reflector is the same as with any optical integrating sphere. The rate of light,  $\Gamma_S$ , onto a sensitive detector of area  $A_S$  is determined by the mean free path

$$\ell_S = \frac{4V}{A_S}, \quad (8.1)$$

giving

$$\Gamma_S = \frac{A_S c}{4V}. \quad (8.2)$$

There is also a photon rate reflected off the outer reflector of area  $A_R$  with reflectivity  $\rho$ ,

$$\Gamma_R = \frac{\rho A_R c}{4V}. \quad (8.3)$$

A photon in an integrating sphere has three options during its lifetime. The first possibility is that it is absorbed by the dead area of the reflector,  $A_D \equiv (1 - \bar{\rho})A_R$ . The second possible

outcome is that it is reflected and continues on its way, and the third is that it is detected by the photosensitive area of the detector. The total efficiency of the detector is given by the ratio of live rates. These three possibilities are encoded in an infinite sum for the efficiency  $\eta$ ,

$$\eta = \sum_{k=0}^{\infty} \frac{A_S}{A_T} \left(1 - \frac{A_S + A_D}{A_T}\right)^k, \quad (8.4)$$

where  $A_T = A_D + A_S + A_R$ . The geometric series sums to reveal the integrating sphere efficiency

$$\eta = \frac{A_S}{A_S + A_D}. \quad (8.5)$$

This result makes sense, as we can only have the final state of the photon ultimately in the sensitive area or the dead area. Equation (8.5) can be given explicitly for certain geometries and detector layouts. Let us assume that we have  $n$  detectors, each of radius  $a$ . For a spherical integrating chamber of diameter  $d$ , this works out to

$$\eta_{\text{sphere}} = \left[1 + \frac{d^2(1 - \bar{\rho})}{na^2}\right]^{-1}. \quad (8.6)$$

For a cubic integrating chamber of side length  $d$ , this works out to

$$\eta_{\text{cube}} = \left[1 + \frac{6d^2(1 - \bar{\rho})}{n\pi a^2}\right]^{-1}. \quad (8.7)$$

The sphere thus has greater efficiency than the cube, so this can be used to estimate the effects of the position dependence at the corners of a cube over a sphere.

### 8.2.2 Monte Carlo

Caltech undergraduate student Chi Feng and I constructed a Monte Carlo model of the UCNb experiment using GEANT4 [104]. The system simulates electrons from 1 keV to several MeV. Simulating electron energies below 1 keV becomes less reliable because of the complexities of the atomic physics at that scale.

Also simulated in GEANT4 is the optical model of the reflector and scintillator. Optical photons are reflected off the high reflectivity outer surface of the integrating chamber. Figure 8.3 shows the geometry of both the reflector and the scintillator used in one of the Monte Carlo studies. Some photons are internally trapped in the scintillator until they are

scattered out into the reflecting chamber or are absorbed by the bulk. This model allowed for calculation of the optical properties beyond just using the analytical model in (8.5). This is important for studying the systematic effects of position dependence and absorption variation of different materials.

Using both the electron and optical models, GEANT4 allowed us to analyze the response function of the energy loss to light conversion. The modeled function is a combination of multiple factors: the response of the light output from different positions within the scintillator box, the optical position dependent response function, and finally the spread of the response function caused by Poisson statistics (also called shot noise). Figure 8.3 shows one of the modeled geometries where the scintillating box was smaller than the integrating reflector.

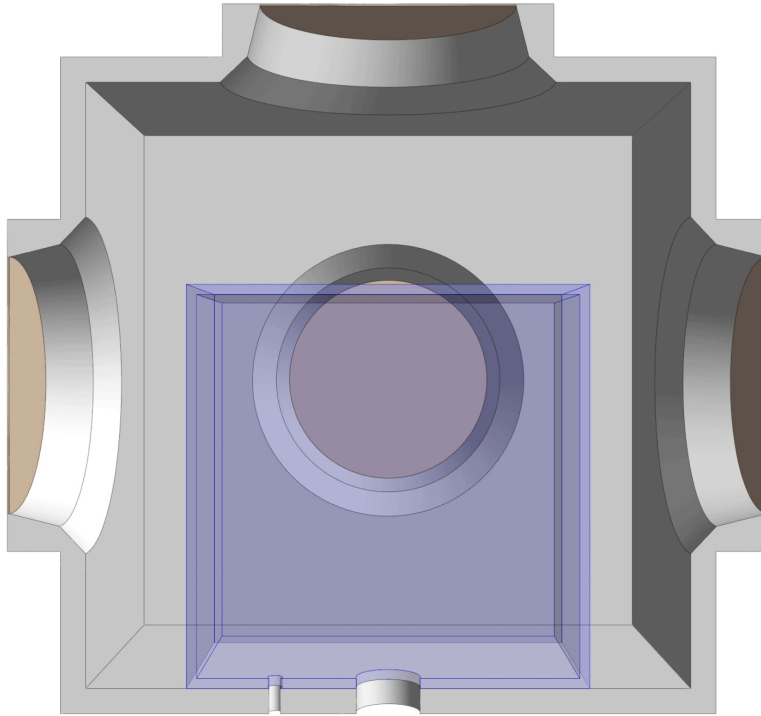


Figure 8.3. One of the Monte Carlo 2012 geometry used as generated by GEANT4

Figure 8.4 shows a simulation of a single photon emitted from the collision point of a 10 keV electron with the plastic scintillator wall. A UV photon that is produced is shifted to blue, and then reflects multiple times until it is detected by the simulated PMT window. Only one photon is shown in figure 8.4(a) for clarity. In reality, many photons are released as shown in figure 8.4(b).

Nominally, even in a well-designed  $4\pi$  scintillator with very minimal position dependence, the largest part of the response that broadens the response function (e.g., resolution) is the Poisson noise from the finite number of photons.

Figure 8.5 shows the difference in response function for 100 keV electrons directed toward the photodetector or aimed at a wall without a photodetector. The response function shows that direct photodetector events have a bimodal distribution, whereas wall events do not [105]. The bimodal distribution is a result of some events depositing more of their scintillator generated light directly into the window of the PMT. Figure 8.6 shows the difference in response function caused by position dependence.

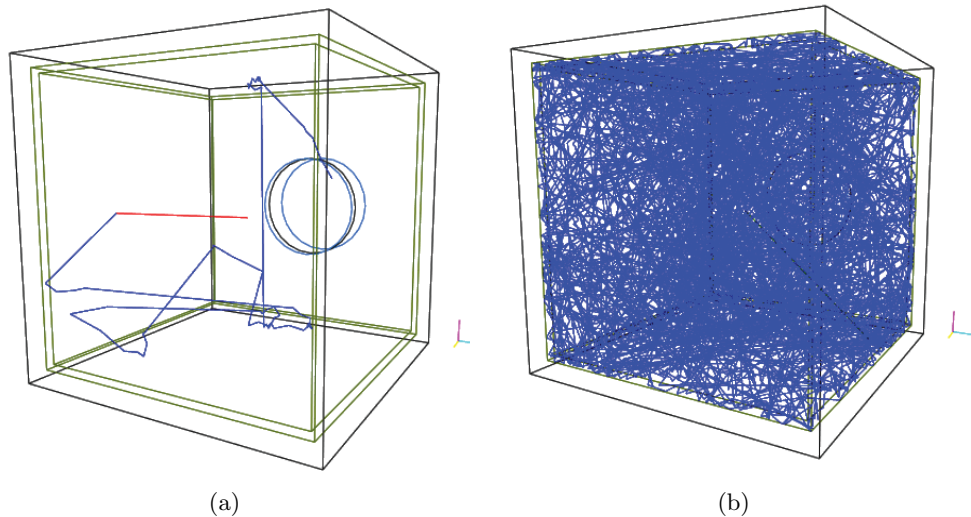


Figure 8.4. Monte Carlo simulation of a collision of a 10 keV electron with the scintillator wall (a) showing only one UV photon which generates one blue photon and (b) a shower of UV photons which are waveshifted into blue photons.

## 8.3 Error budget

### 8.3.1 Response function

As discussed in chapter 7, one of the most difficult challenges in extracting  $b$  is the determination of the response function. This is further compounded by the problem that most calibration sources are not exact monoenergetic sources and have overlapping conversion lines. Good approximations of mono-energetic electron sources are conversion electron sources such as  $^{113}\text{Sn}$  or  $^{207}\text{Bi}$  which have conversion lines in the neutron beta decay energy

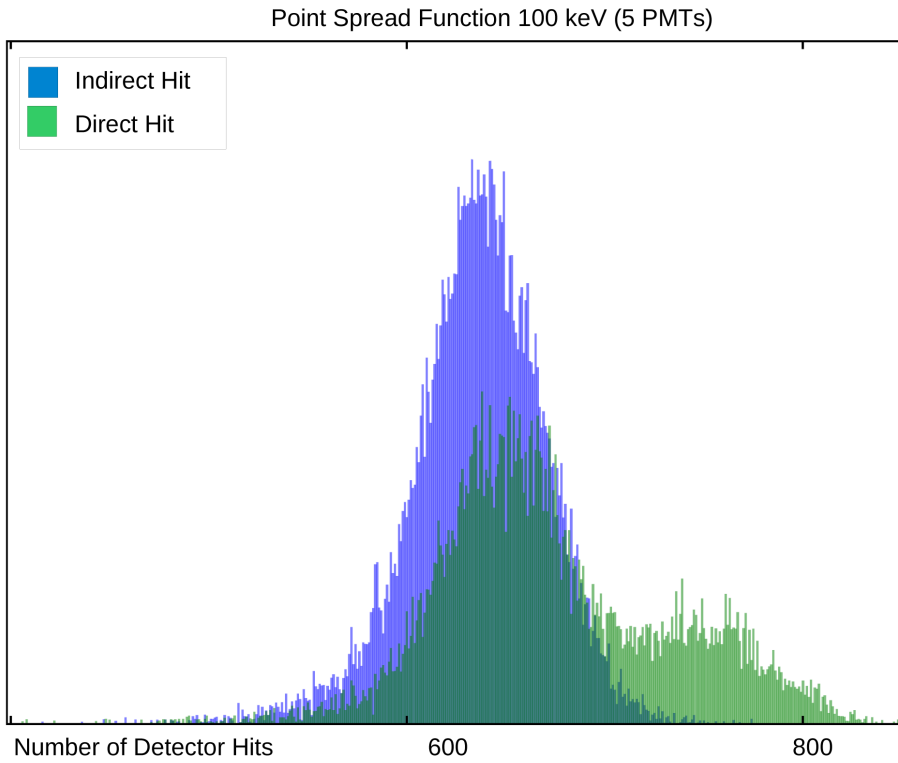


Figure 8.5. Monte Carlo results of events directed toward a detector or toward a wall.

range. Because of the poor resolution of a scintillator-based calorimeter, the response function is difficult to measure directly without good understanding of these type of electron sources. One solution is to calibrate the response function *ex situ* using an electron accelerator. We have one such “e-gun” at the Kellogg Radiation Laboratory at the California Institute of Technology. The e-gun only reaches an energy of 135 keV which is not the full range of the end point,  $E_0$ , of the neutron beta decay spectrum. Ideally, we would want to calibrate to even higher energy than the end point to extend the region in which we test for linearity. A possible improvement to the UCNb experiment is to construct an e-gun that covers most or all of the energy range of neutron beta decay electrons. One advantageous option would be to construct this *in situ* with the UCN source.

### 8.3.2 Inherent $\gamma$ backgrounds

Several inherent backgrounds are present in the experimental hall which must be subtracted. The pulsed proton beam induces spallation inside the target, producing thermal neutrons

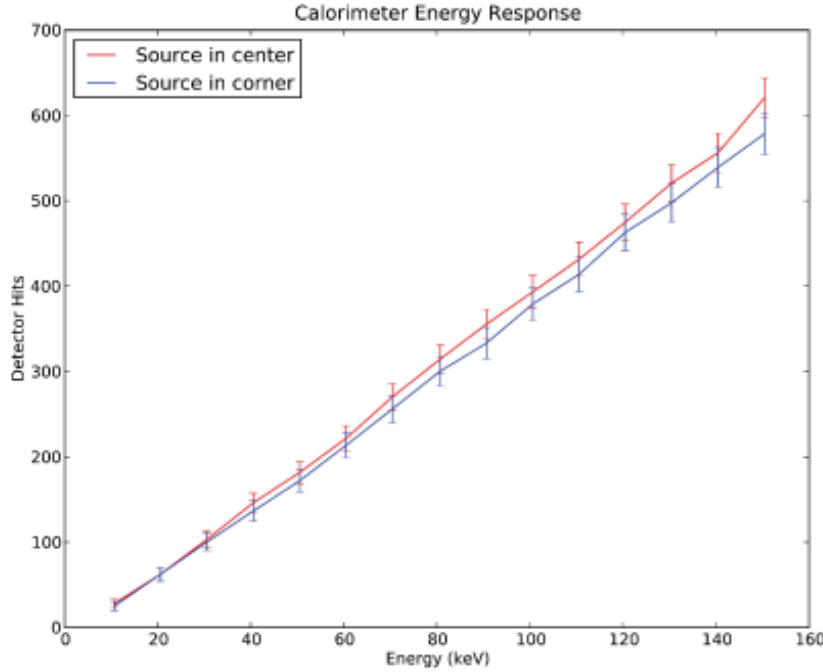


Figure 8.6. Monte Carlo results of events produced in the center or the corner of the scintilator in the geometry that fills the entire detector.

that quickly activate the iron and concrete in the shield package. This creates long-lived activated nuclei as well as prompt gammas. The prompt background can easily be gated out by vetoing a short time window around the beam pulse, about 1 ms every 5 seconds. The longer-lived components are much more difficult to veto. They must be shielded out by a lead shield and background subtracted.

### 8.3.3 UCN generated backgrounds

UCN can generate background from the prompt  $\gamma$  following neutron capture on the walls of the storage vessel. This prompt  $\gamma$  rate can be estimated by

$$\Gamma = \rho \lambda_n \sigma_n v_0 / v_n, \quad (8.8)$$

where  $\rho$  and  $\sigma_n$  are the density and thermal cross section for nuclei in the walls,  $\lambda_n$  is the wavelength of the UCN,  $v_n$  is the UCN velocity, and  $v_0 = 2200$  m/s the thermal speed of neutrons. For deuterated polystyrene walls, the main capture nucleus is mostly carbon. The thermal capture cross section for  $^{12}\text{C}$  (98.9%) is 0.0035 barn. Using this for UCN at 5

m/s we get a neutron capture rate of  $6 \times 10^{-7}$  per bounce,

$$(5 \times 10^{22} / \text{cc})(80 \text{ nm})(0.0035 \text{ barn})(2200 \text{ m/s})/(5 \text{ m/s}) = 6 \times 10^{-7}. \quad (8.9)$$

In the large plastic scintillator geometry, the box volume is  $2 L$  so there are  $6 \times 10^4$  k UCN at 30 UCN/cc so the overall bounce rate is about 3 MHz. This yields a prompt gamma rate of about 2 Hz. The gammas should generate  $\approx 3\%$  Compton rate in the beta scintillator which leads to a  $\approx 50$  mHz prompt background. The noise to signal ratio for this is  $\approx 7 \times 10^{-4}$ , independent of UCN density.

The thermal cross section for  $^{13}\text{C}$  (1.1%) is 0.0014 barn, so the natural abundance capture rate is 8 mHz. This gives an additional prompt gamma background of 0.2 mHz and a noise to signal  $\approx 3$  ppm, which is obviously dwarfed by the  $^{12}\text{C}$  capture background.

In addition to the prompt background, UCN can also activate materials that later beta decay. Unlike the prompt UCN generated background, this background would build up over time. For example,  $^{14}\text{C}$  beta decay could be a source of background because the peak and end point (156.5 keV) is in the region of interest for  $b$ . To find out how big this effect is, we need to know the effective beta decay rate generated by UCN capture on natural  $^{13}\text{C}$ . What we find is that even after running 100 days of continuous activation, though time dependent, this background is very small,  $\approx 70$  nHz. This has a noise to signal of 1 ppb. Unlike the prompt background, this depends on the UCN density. These calculations show the biggest background is from prompt gammas from capture on  $^{12}\text{C}$ , but this rate is still small enough for a 0.01 measurement of  $b$ .

#### 8.3.4 Lead shield

In order to limit the inherent background, the experiment must be placed inside a lead shielding box. Since even high energy gammas can scatter inside the experiment and create a low energy background, the shielding must have a high attenuation factor to 1 MeV gammas. The lead shield can be seen schematically in figure 8.14.

### 8.4 Calibration and gain monitoring

Since the measurement of  $b$  is basically a measurement of the energy spectrum, careful calibration and gain monitoring are required. We designed a new PMT base to increase the



Figure 8.7. This photo shows our custom Hamamatsu R7725 base assembly.

linearity specifications provided by Hamamatsu for tube type R7725 (see figure 8.7 and 8.8.) The PMT base circuit was a custom modification of the original Hamamatsu design. One important change was the increase of the voltage rating of the capacitors, as these failed in the UCNA experiment and caused severe nonlinearity in the original Burle bases, first used in the UCNA apparatus. Another change was the addition of more interstage capacitors in the lower stages to help replenish charge on the lower stage dynodes of the PMT. Assuming the log of the gain,  $\log G = 7$ , each stage has a gain of roughly  $10^{7/12} \approx 3.8$  and thus if charge is depleted on a stage  $n$  dynode, the output signal could drop at peak voltage by

$$\ell = 10^{-(n \log G)/12}. \quad (8.10)$$

A goal of  $10^{-3}$  linearity would require a capacitor on the 5th stage of the voltage divider chain. Some comparatively simple changes were also made such as adding a bypass  $100 \text{ M}\Omega$  resistor to allow discharge of the signal isolation capacitor.

While the new design improved linearity, many systematic effects such as gain drift and temperature-dependent linearity remained. Because the gain follows voltage to the 12th power for a 12 stage PMT, a slight change within the resistance chain can lead to a large change in gain. To mediate these stability errors, the experiment is designed to be temperature stabilized using copper cooling plates attached to a high precision cooler. Even with temperature stability however, gain monitoring is required. To do this, we prototyped several gain monitoring systems (GMS) for monitoring the drifts in optical and electronic

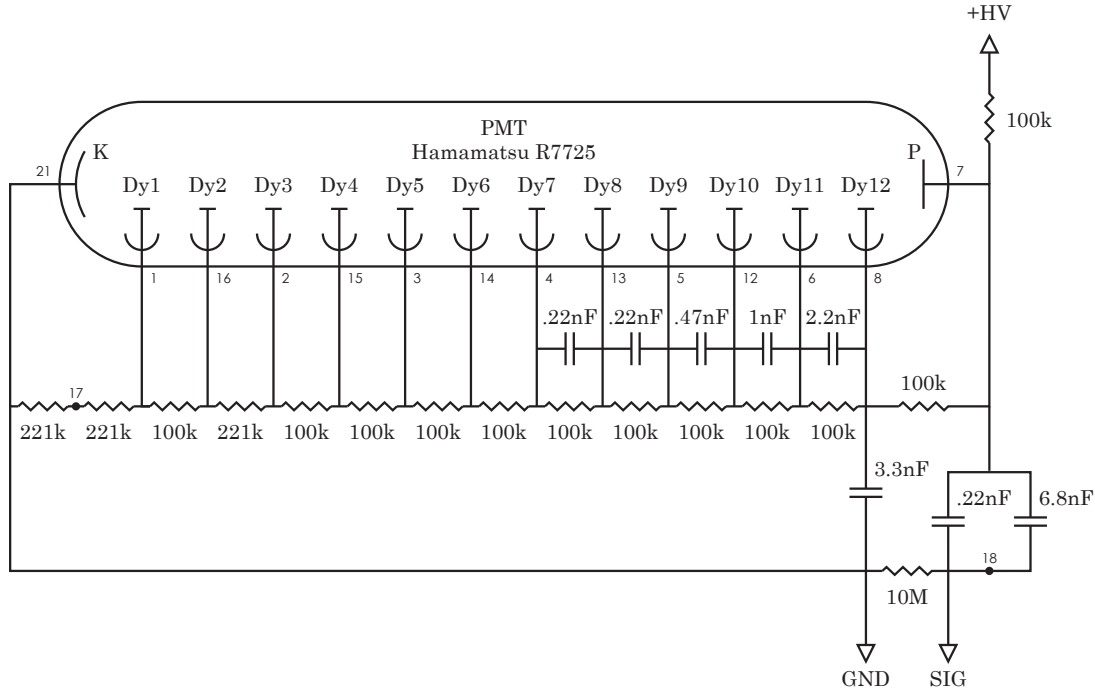


Figure 8.8. The schematic of the Hamamatsu R7725 base design.

gain.

#### 8.4.1 Insertable sources

An important method for monitoring gain is a direct measurement of the light output from a known and stable electron source. An ideal solution is to use radioactive sources that emit conversion electrons. Two examples are  $^{113}\text{Sn}$  and  $^{207}\text{Bi}$  with conversion lines around 360 keV for  $^{113}\text{Sn}$  and 500 keV and 1 MeV for  $^{207}\text{Bi}$ . We designed a source that sits on the end of a fiber and can be inserted and withdrawn without breaking vacuum. This is done with a fiber feedthrough and vacuum bellows. The value of a source that can be inserted with a sealed vacuum bellows system is that the PMT voltage does not need to be toggled off and on. Also, the system does not need to be vented and pumped down, all time consuming and possibly gain destabilizing.

Figure 8.9 shows us a magnified view of the tip of the insertable sources. Figure 8.10 show us detail of the machined tip of the insertable sources. The sources were made from a

scintillating blue fiber, 1 mm in diameter. A jig was constructed by the Caltech Instrument Shop to drill a 800  $\mu\text{m}$  cup 1000  $\mu\text{m}$  deep. The inside of the cup is coated with dried radioactive material such as  $^{113}\text{Sn}$  or  $^{207}\text{Bi}$ . The fiber is scintillating so that if an electron

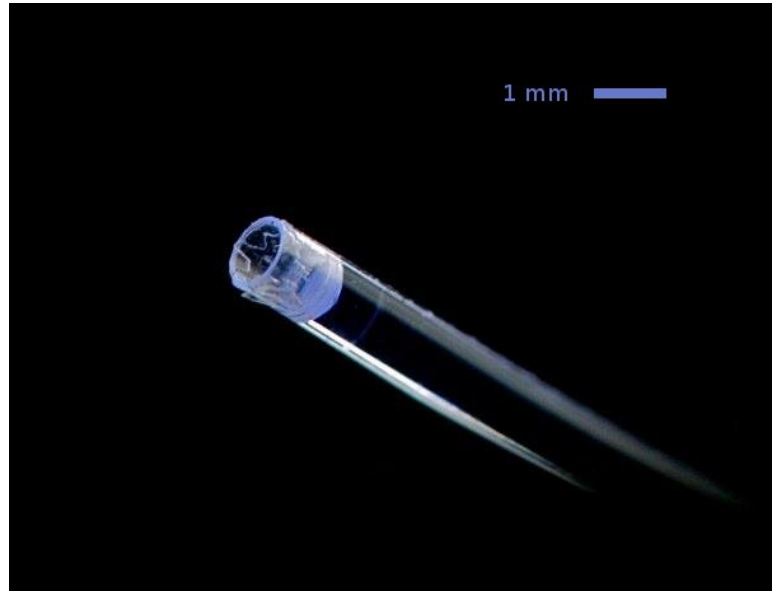


Figure 8.9. An insertable source used for calibrating with a conversion electron source such as  $^{113}\text{Sn}$  or  $^{207}\text{Bi}$  without venting the UCNb vacuum system.

passes through the wall of the cup, or into the fiber, a tagging signal can be detected. This may be done with a PMT on the end of the fiber, outside the vacuum system. This can either be used as a veto, or, if enough light is captured, can be used to measure the lost energy. The amount of light captured is limited by the trapping efficiency of the fiber, which is low if unclad.

#### 8.4.2 Other calibration sources

Two other methods were tested as a means of calibration. The first method used traditional gamma sources, cobalt-60 and cesium-137, outside the vacuum chamber. The gamma rays from these sources Compton scatter off electrons in the calorimeter, leaving a Compton edge. The UCNb calorimeter, made of carbon and hydrogen, is too thin and too low in  $Z$  to see a full energy photopeak. Figure 8.11 and figure 8.12 show spectra of the Co and Cs sources used to identify the Compton edge as a calibration point.

Also used as a calibration source was activated xenon. We placed natural xenon into the LANL UCN source and froze it to the bottom surface where the cold neutron density is

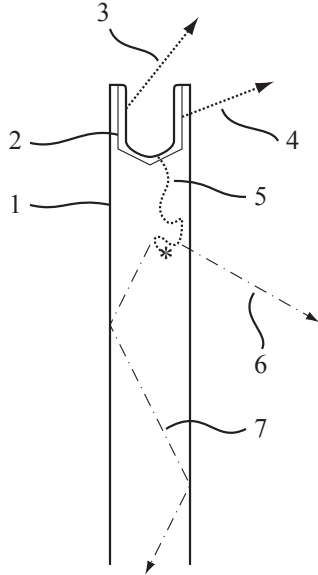


Figure 8.10. A detailed schematic of the insertable source. (1) 1 mm plastic scintillator fiber; (2) machined hole coated with radioactive material; (3) conversion electron leaving the hole; (4) tagged conversion electron; (5) vetoed conversion electron; (6) liberated scintillation light; (7) trapped scintillation light.

largest. Within minutes the xenon is activated and can be warmed back into the gas phase. The gas is stored and small quantities can be carefully delivered into the detector. Figure 8.13 shows a plot of data taken using activated Xe. The dominant peaks are 134 keV from  $^{125}\text{Xe}$  with a 16.9 hour half-life and 444 keV from  $^{135}\text{Xe}$  which also has a 915 keV end point beta decay spectrum and a 9.14 hour half life.

## 8.5 The experiment

In this section we describe the UCNb experimental setup and discuss some early results from runs during the 2010–2012 run period. Since most of this time period was spent on constructing the experiment, little time was left for iterative running and revising. However, enough run time was collected to learn about the systematic effects to help steer the design for the upcoming run cycle.

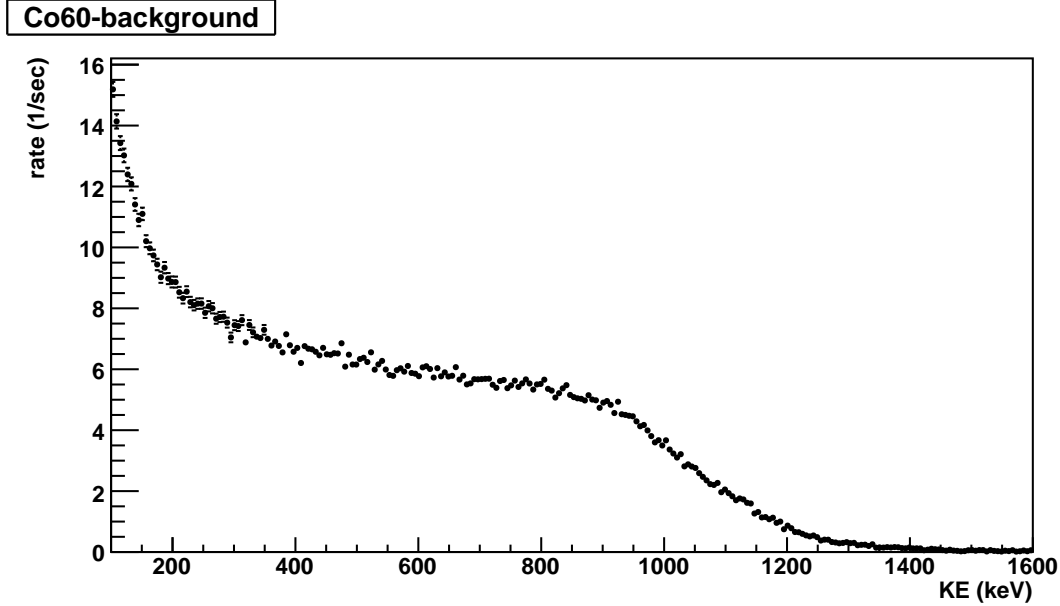


Figure 8.11. Exterior  $^{60}\text{Co}$  source

### 8.5.1 Mechanical setup

A schematic view of the UCNb experiment *in situ* is shown in figure 8.14. UCN first exit the source shield package. The density of UCN are sampled by a small hole into the Gate Valve monitor. UCN that fall through this guide are accelerated by gravity and detected by a  $^3\text{He}$  proportional wire chamber neutron detector. The majority of UCN continue on through the UCN Gate Valve. UCN can be shut off to most experiments by closing the gate valve. As discussed in chapter 5, the UCN source is sealed off from the rest of the UCN beam line by a zirconium foil. The foil is embedded in a magnetic field generated by the prepolarizing magnet (PPM). The coils in the PPM are contained in a return yoke so as to minimize the field outside PPM bore. Hall probe measurements have shown the field to drop to 20 Gauss outside the bore. While most of the UCN beam line is well isolated from the UCN source, the UCNb experiment is not. Instead, it has a small port before the gate valve that can be closed by its own ball valve. After the ball valve, is a thin ( $6 \mu\text{m}$ ) polyethylene window. Polyethylene was chosen because it has a near-zero Fermi potential which allow UCN to pass through without the magnetic boost needed to pass through the 90 neV potential of the zirconium foil. This avoids the need to polarize the UCN entering the UCNb apparatus, which would cut the UCN density in half and introduce a systematic asymmetry by making the UCN sensitive to magnetic fields. When the ball valve is open, UCN enter the decay

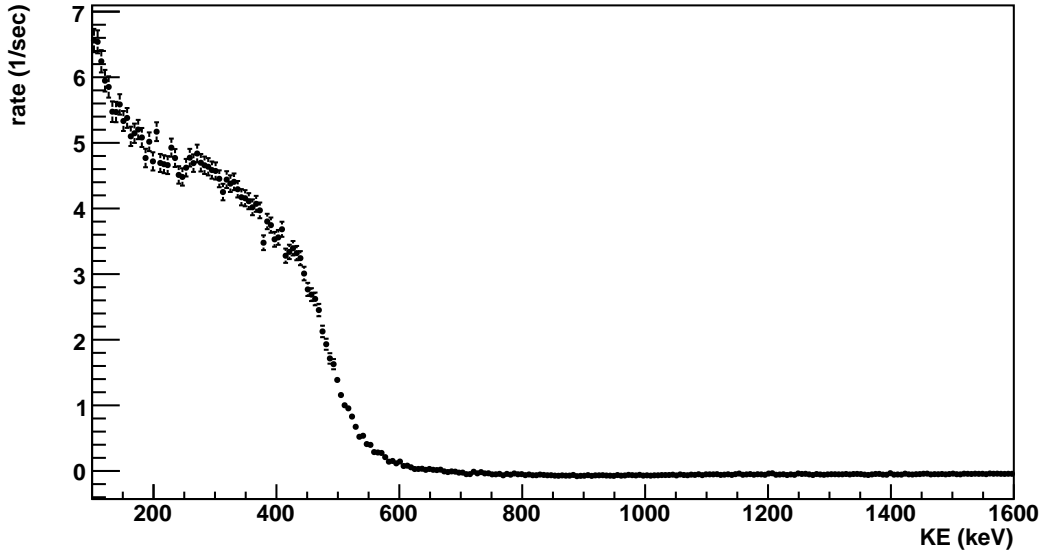
**Cs137-background**


Figure 8.12. Exterior  $^{137}\text{Cs}$  source

volume enclosed by the scintillating walls. Surrounding the walls is a 7 mm thick layer of Spectralon made by Lab Sphere in North Sutton, New Hampshire. [106, 107]. Spectralon is a special reflective material made of sintered PTFE, with reflectivity of 99% at 400 nm. Connecting to the top is the insertable source. The source is connected by a vacuum bellows to an optical fiber, via 1 mm fiber UV/VIS feedthrough. The source consists of a scintillating fiber with a small cup. We manufactured the  $^{207}\text{Bi}$  sources at California Institute of Technology and the  $^{113}\text{Sn}$  source at North Carolina State University. Radioactive material was dried inside the cup repeatably until the desired activity of about 50 nCi was achieved.

PMTs also enter the integrating cubical reflector, but not the scintillating cube. The PMTs are connected to an electronic voltage divider base, that is mounted inside the vacuum chamber, but is sealed off from the vacuum by o-ring seals that hold a pressurized non-conductive gas, typically  $\text{CF}_4$  which has a high dielectric standoff.

In one set of runs, the entire assembly sat inside of a lead shielding enclosure to reduce the ambient and beam background.

### 8.5.2 Electronics

The photosensors used were Hamamatsu R7725 Bialcali photomultiplier tubes. These tubes are the same type as employed by the UCNA experiment. A custom base circuit was already

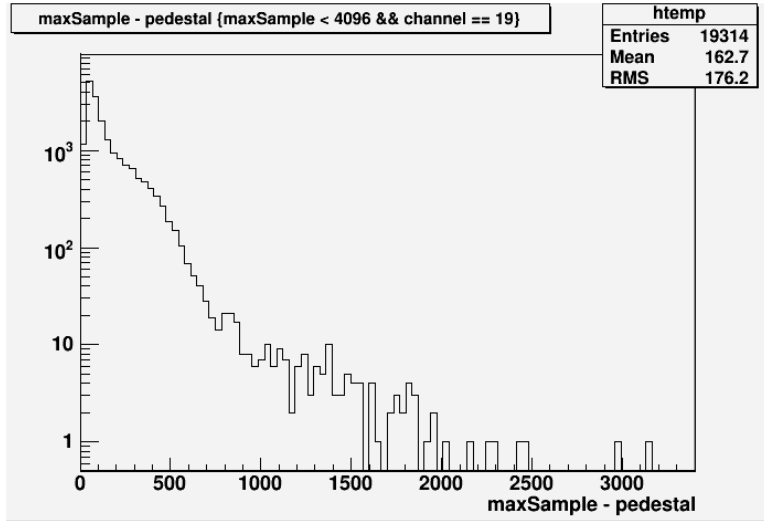


Figure 8.13. Activated Xe run in the large DPS geometry.

designed and tested by Hickerson and Morris for the UCNA experiment. The linearity tests were also performed in the SCS using the UCNA light pulser system and DAQ, so we knew that the combination PMT and base would have linearity of at least 1% in a similar rate and charge per pulse as the UCNb experiment.

Figure 8.18 shows an example of the electronic schematic used for runs in 2012. The output of the PMT base was amplified by an Ortec 474 timing filter amplifier. A small integration time of 20 ns was added to smooth out some high frequency noise. The input to the 474 is terminated at  $100\ \Omega$ , whereas the PMT base was terminated at  $50\ \Omega$  to impedance match the signal cables used, so a  $100\ \Omega$  termination resistor must be placed in parallel with the signal line.

The output is then split to a Phillips Scientific 708 discriminator and also a  $> 64$  ns delay for the ADC. The threshold of the discriminator was typically set to 30 mV, right above the single photon peak. The discriminator logic pulse was fed into a Phillips Scientific 756 coincidence unit to allow for 2/4 coincidence of multiple PMT channels.

The coincidence signal was used as a trigger for a Phillips Scientific 794 gate generator. This gate generator also had an inhibit input used to gate off beam pulses from a conditioned H-GX signal provided by the LANCE accelerator. The output of the 794 was split back to act as a gate for the Phillips Scientific 744, to gate on the delayed PMT output signal, and to a scalar and timer pair used to measure the raw rate. The corrected gated signal was either fed back directly into our custom flash ADC (fADC) or was summed with all channels

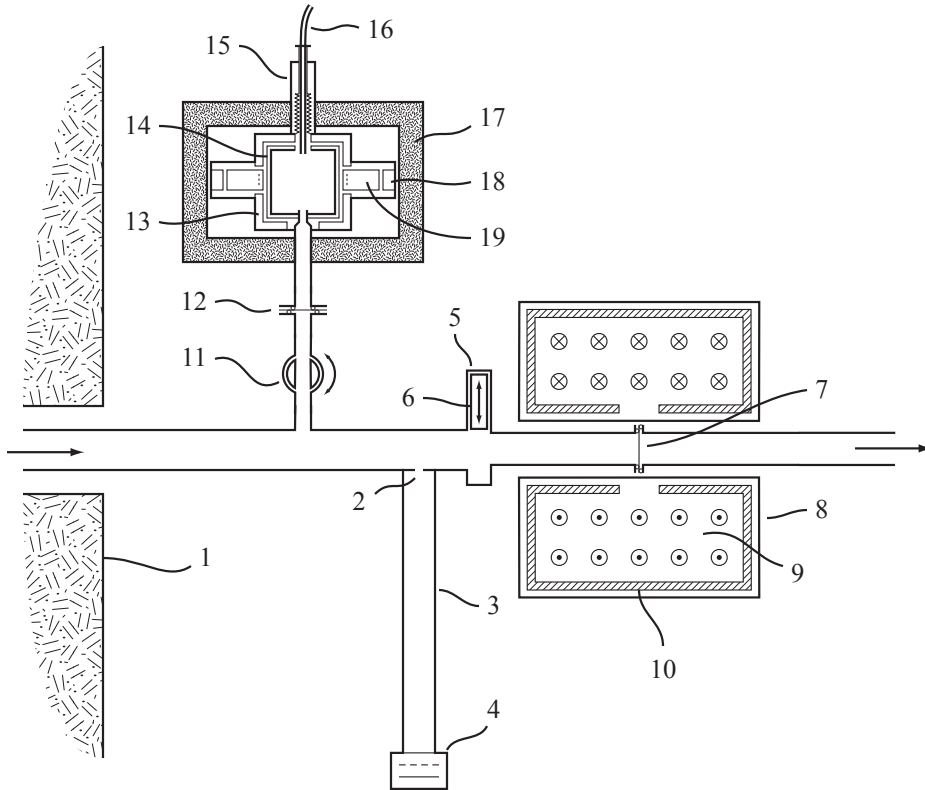


Figure 8.14. Experimental setup for the foil transmission measurements. (1) the shield package surrounding the UCN sources; (2) the UCN monitor port; (3) UCN guides; (4) UCN  $^3\text{He}$  detectors; (5) gate valve housing; (6) UCN valve; (7) Zr foil; (8) PPM; (9) PPM current coils; (10) PPM shielding yoke; (11) UCNb 1" ball valve; (12) UCNb 1" UCN guide with thin polyethylene film window; (13) Spectralon reflector; (14) scintillator; (15) insertable source bellows; (16) insertable source fiber; (17) Pb shielding; (18) PMT base; (19) PMT.

and fed into a MCA for a simple, less gain matched signal. The fADC was designed and built by Dr. Fred Grey of Regis University primarily for use at LANL on the  $\mu$ rad project.

## 8.6 Results

In our first runs we discovered that we had  $^6\text{He}$  contamination from spallation in the source vacuum enclosure. Using a timing of 30 seconds between beam pulses, we could isolate the  $^6\text{He}$  signal (807 ms half-life and 3.5 MeV endpoint) from the UCN generated signal and the  $\gamma$  ray prompt background. The results are shown in 8.19. For later runs, a UCN transport thin polyethylene film was inserted to block the  $^6\text{He}$ . Polyethylene was used because it has a Fermi potential very near zero.

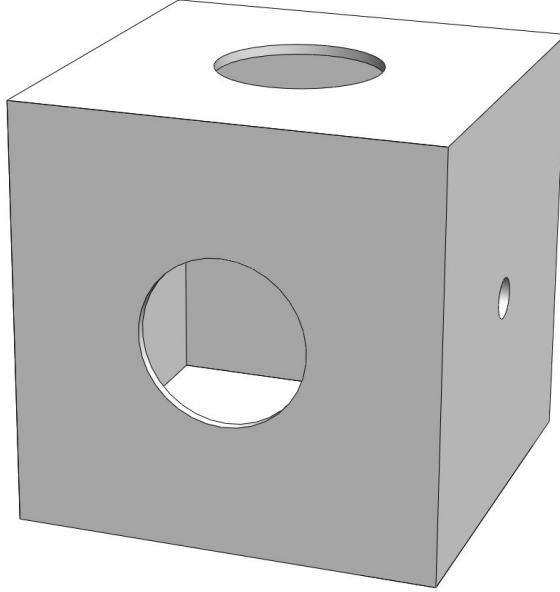


Figure 8.15. The Spectralon reflector.

Shown in figure 8.20 are the calibration results from runs using a  $^{207}\text{Bi}$  disk placed inside the scintillator box. The disk was placed in the center of the bottom of the box, over the UCN entrance hole. The drawback of this calibration scheme is that conversion electrons may scatter off the disk holder material (Mylar) before reaching the scintillator. Another drawback is that optics of the integrating box are altered by the presence of the 1" silver colored disk. This electron scattering results in peak broadening and resolution reduction. However, the 1 MeV peak of Bi is still plainly visible allowing a reliable method to find the location of the neutron endpoint.

Figure 8.21 shows the calibration results for a  $^{113}\text{Sn}$  disk, also embedded in mylar. Again, this has the same drawbacks as the Bi disk by affecting optics and electron scattering. In the 2012 data runs, we were able to use the insertable sources. These are designed to impact the optics less as well as tag the events where scattering occurs.

In figure 8.22, the results from a background-subtracted run using the  $^{207}\text{Bi}$  insertable source are shown. An unexpected result is that the single 1 MeV peak appears bimodal. Similarly, figure 8.23 shows the  $^{113}$  insertable source. We suspect that this is the result of the geometry of the fiber cup shape in which some electrons leave the cup through the open bottom, and some must pass through fiber. It is also possible that this is the result of the splitting predicted by the GEANT4 Monte Carlo as shown in figure 8.5, however, it is not clear why the bimodal splitting would be on the order of 50% when the Mote Carlo predicts



Figure 8.16. This CAD drawing shows the UCNb experiment in a proposed 2012 geometry.

around 10% of the events should be direct and have a higher light output. Further analysis and measurement is needed to see if this effect can be eliminated by cutting on the pulse height of light through the fiber or by reducing the position dependence of the box.

Figure 8.24 shows the background subtracted runs of UCN placed in the UCNb apparatus. The runs consisted of 120 sec of the UCN valve open, with 120 sec runs with the UCN valve closed to serve as a background measurement. The background is shown in 8.25. The most striking feature of these runs are that what UCN generated signal does not appear to have any definitive beta decay spectral shape. The UCN rate in the range 100–1600 keV, as calculated using the rate with the UCN vale closed subtracted from the rate with the UCN valve open is  $4.9(1) \text{ sec}^{-1}$ . This was on top of a background rate (UCN valve closed) of  $29.4(1) \text{ sec}^{-1}$ . If the UCN generated rate was completely accounted for by beta decay, the density would be 2.8 UCN/cc.



Figure 8.17. This CAD drawing shows a cross section of the UCNb experiment in one of the proposed 2012 geometries. Inside is shown the  $\text{CaF}_2$  scintillator with a  $\text{MgF}_2$  coating.

To date, the UCNb experiment has been an effective prototype of a UCN calorimeter except for the inability to store UCN for long lifetimes, and the inability to collect a definitive beta decay spectrum. Future upgrades should help alleviate these issues.

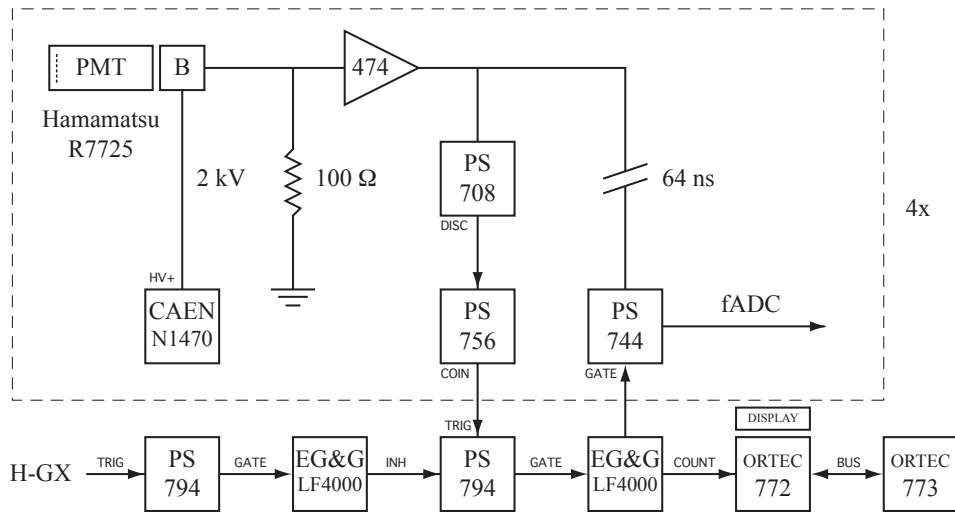


Figure 8.18. The electronic schematic for the NIM electronics for a typical UCNb experimental setup. The detail of the PMT base labeled B is shown in figure 8.8.

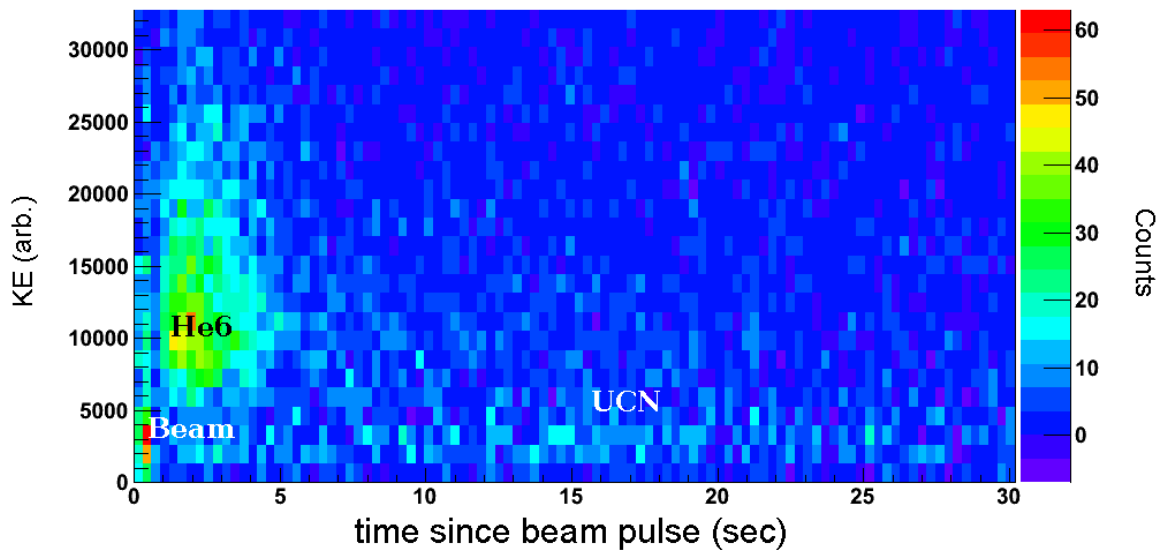


Figure 8.19. A 2D plot of counts per time, by time versus pulse height. Visible is the decay of spallation  ${}^6\text{He}$ , the beam pulse background, and the UCN generated signal which has the longest lifetime determined by the storage time of the UCN source.

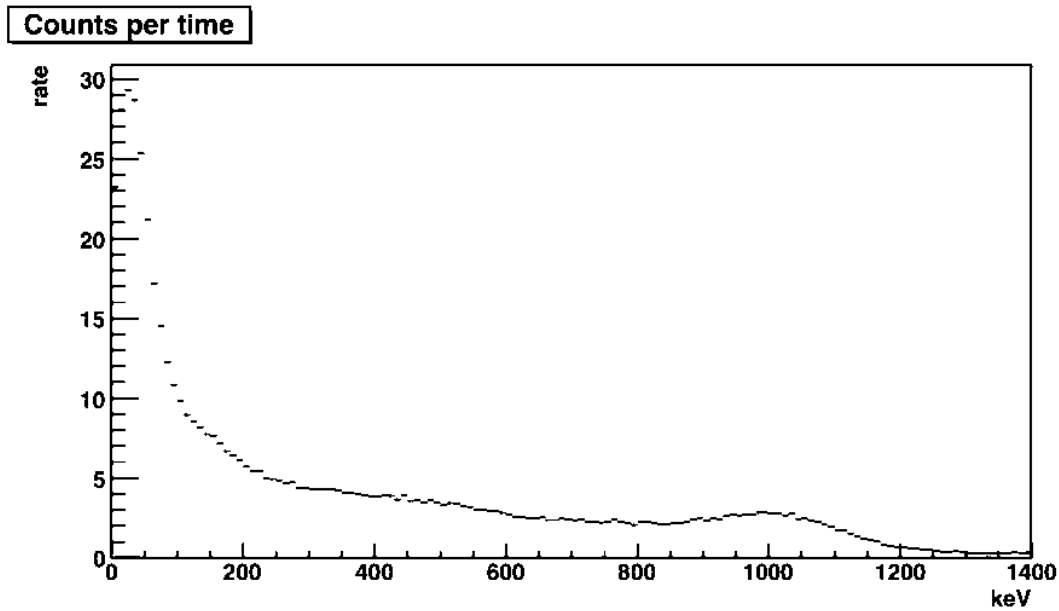


Figure 8.20.  $^{207}\text{Bi}$  2010 from a calibration disk.

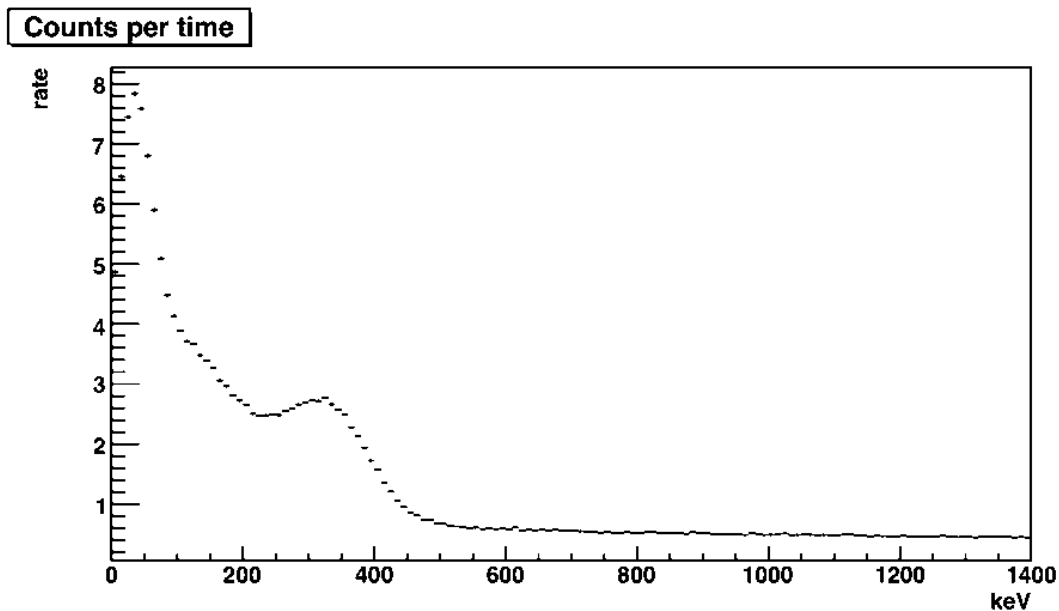


Figure 8.21.  $^{113}\text{Sn}$  2010 from a calibration disk.

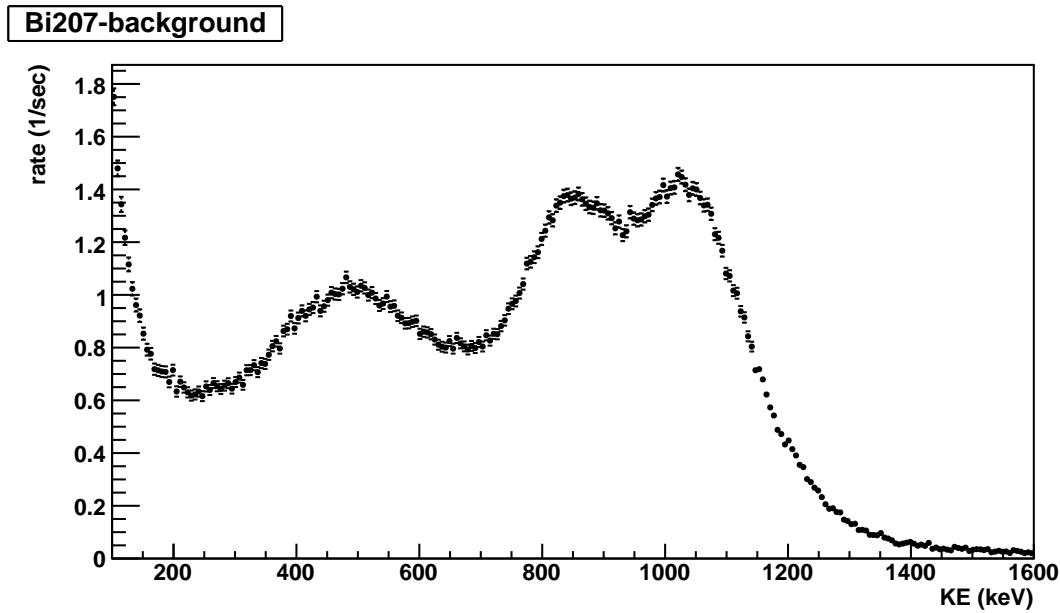


Figure 8.22. Background-subtracted  $^{207}\text{Bi}$  2012 using the insertable source.

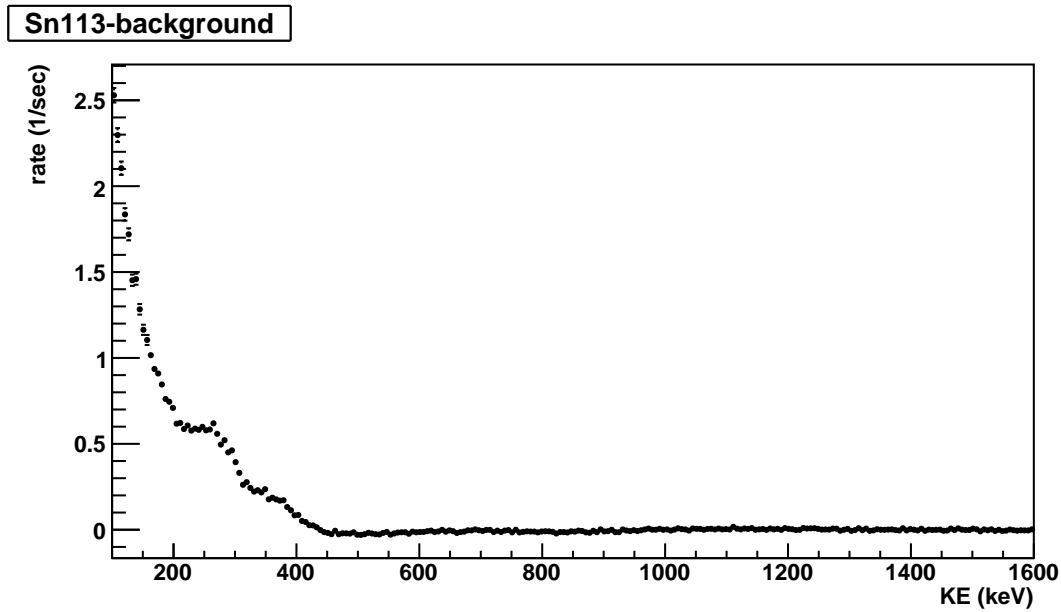


Figure 8.23. Background-subtracted  $^{113}\text{Sn}$  2012 using the insertable source.

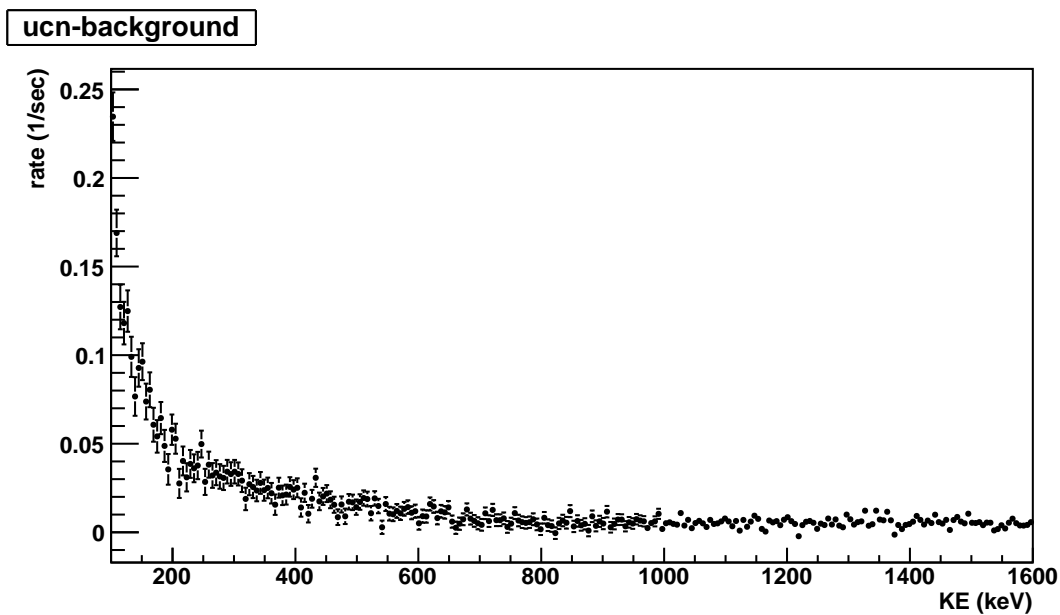


Figure 8.24. Background-subtracted UCN generated signal from the 2012 run.

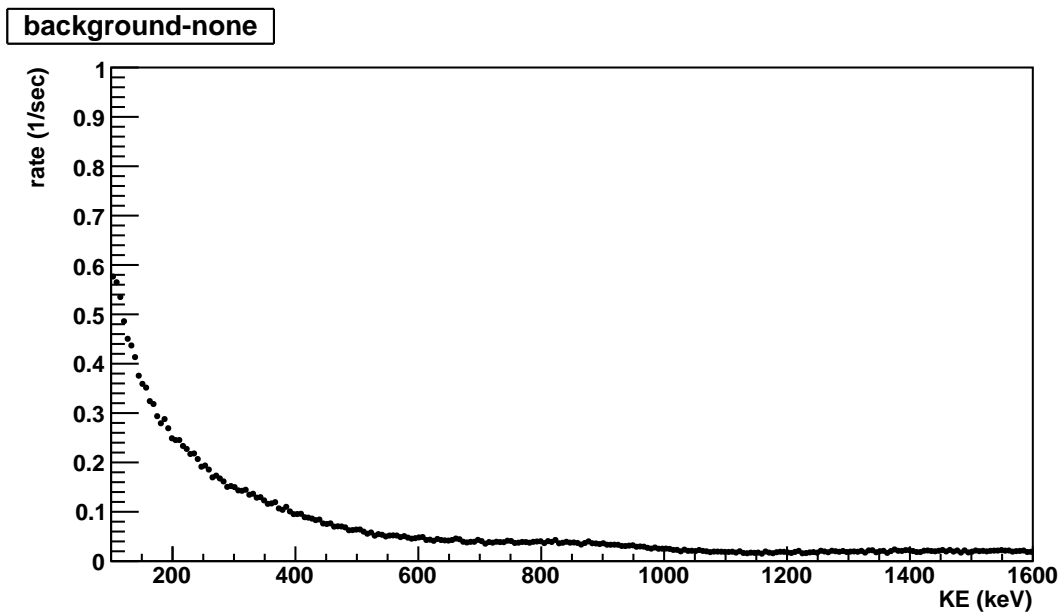


Figure 8.25. Background from the 2012 run.

# Chapter 9

## Future Directions

### 9.1 Upgrades for UCNb

The future holds some exciting possibilities for the UCNb experiments. The final goal of the current experimental project at LANSCE is to measure  $|b_n| < 10^{-3}$ . To do this, several improvements over the current prototype are required. These improvements include developing the detector coatings; increasing the size of both the detector volume and integrating sphere; adding a phoswich (see below); and increasing the overall symmetry of the response.

The detector stack needs to store neutrons. Developing a working coating, which does not leak UCN to regions where they can generate background, is the top goal of the remainder of 2012. Past that, the goal will likely be to create a coating that is thin, even, and does not have a significant dead layer to electrons.

Another improvement is to increase the overall size of the entire apparatus. The larger the storage cell, the larger the signal to background becomes. A larger storage cell also allows for large statistics to be collected very quickly, decreasing the variation in background. Also, by increasing the size of the integrating sphere relative to the storage cell, the position response can be reduced through optical integration. Figure 9.1 shows a possible upgrade to the UCNb experiment that is larger, with eight PMTs, but still fits onto the current platform.

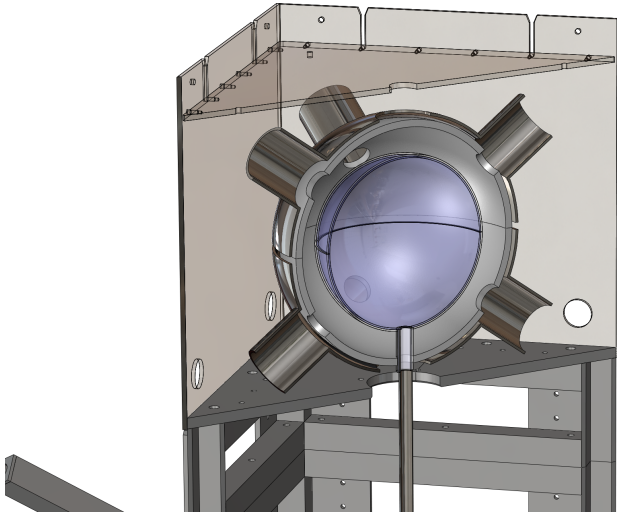
One method for rejecting lower energy gammas, x-ray and Compton background is to use a phoswich. A phoswich is a sandwich of multiple scintillators with different characteristics that allows for the distinction of different particle types or momenta directions. For example, one implementation in the UCNb box is to place a hermetic outer slow scintillator around a fast inner scintillator.



Figure 9.1. This drawing shows a cartoon of a possible upgrade of the UCNb experiment. There are eight PMTs that lie on the faces of a virtual icosahedron that lay on the outer spherical vacuum jacket.

A phoswich also acts as a muon veto. Adding a phoswich to the design is a critical step to lowering the extrinsic background from outer Compton electrons generated in the vacuum enclosure. The phoswich will also help identify low-energy x-rays and Compton electrons that are intrinsically generated by UCN from inside the box. Experimentally determining if the phoswich provides an effective method for tagging both types of background event, extrinsic and UCN generated, will be the highest priority for UCN run the next year. Increasing the spherical symmetry is an important method of decreasing the systematic error induced from varying response from differing parts of the apparatus. A spherically symmetric scintillator will release the same amount of light, at the same angles for each electron. Light emitted into a true integrating sphere will be integrated equally and uniformly. Figure 9.2 shows a cross section of a possible upgrade to the UCNb experiment which has uniform spherical symmetry. The experiment has a clamshell design with two halves merging at an equator. The new design also features a phoswich that envelops the main scintilating calorimeter.

Figure 9.2. This drawing shows a cross section of a possible upgrade of the UCNb experiment. The integrating chamber and scintillator are spherical to maximize symmetry.



## 9.2 Future Run plans

The run plan for the rest of 2012 is to construct two boxes of different sizes. Each box will have an inner and outer layer. The inner layers will be the primary detector made of fast BC-404 (or EJ-204). The outer boxes will be made of BC-444 (or EJ-240) and will produce a slow response time pulse which can be used as a veto by pulse shape analysis [102].

## 9.3 Toward $10^{-4}$

Another, equally important goal is to develop a path toward a  $|b_n| < 10^{-4}$  experiment. Due to the low resolution of PMTs and scintillators, it is difficult to see how the current approach could take us to  $10^{-4}$ . This would require measuring the response mean and other moments to more than two orders of magnitude below actual detector resolution. Detectors with better resolution would allow for a better measurement of the response function of the detector.

Other detectors possibilities include high resolution Si detectors such as will be used for the UCNB experiment [108]. Another possibility is to use microcalorimeters. Microcalorimeters have resolution in the eV range, yet can measure over MeV energy ranges making them ideal for precision spectroscopy.

Whatever direction the experiment takes, reaching a precision of  $10^{-4}$  would unlock new insight into scalar and tensor interactions.

## Appendix A

### ***n*-forms**

For the  $p$ -form  $\alpha \in \Lambda^p(\mathbb{R}^n)$ , and  $q$ -form  $\beta \in \Lambda^q(\mathbb{R}^n)$ ,

$$\alpha \wedge \beta = (-1)^{p+q} \beta \wedge \alpha, \quad (\text{A.1})$$

and

$$d(\alpha \wedge \beta) = d\alpha \wedge \beta + (-1)^p(\alpha \wedge d\beta). \quad (\text{A.2})$$

Stokes' Theorem say for a  $k$ -manifold  $M$  with boundary  $\partial M$  and  $\omega$  is a  $(k-1)$ -form on  $M$ , then

$$\int_M d\omega = \int_{\partial M} \omega. \quad (\text{A.3})$$

## Appendix B

# Leptoquarks

In this appendix we have a table provided by Dr. V. Cirigliano and Dr. E. Passemard. We present the Lagrangian used to calculate the effective four-fermion interaction term and the Fierz rearrangement terms,

$$\begin{aligned}
\mathcal{L} = & g_{1L} \bar{q}_L^c i\tau_2 \ell_L S_1 + g_{1R} \bar{u}_R^c e_R S_1 + \tilde{g}_{1R} \bar{d}_R^c e_R \tilde{S}_1 \\
& + g_{3L} \bar{q}_L^c i\tau_2 \vec{\tau} \cdot \vec{\ell}_L \cdot \vec{S}_3 + g_{2L} \bar{d}_R^c \gamma^\mu \ell_L V_{2\mu}^\dagger \\
& + g_{2R} \bar{q}_L^c \gamma^\mu e_R V_{2\mu}^\dagger + \tilde{g}_{2L} \bar{u}_R^c \gamma^\mu \ell_L \tilde{V}_{2\mu}^\dagger \\
& + h_{2L} \bar{u}_R \ell_L R_2^\dagger + h_{2R} \bar{q}_L i\tau_2 e_R R_2^\dagger + \tilde{h}_{2L} \bar{d}_R \ell_L \tilde{R}_2^\dagger \\
& + h_{1L} \bar{q}_L \gamma^\mu \ell_L U_{1\mu} + h_{1R} \bar{d}_R \gamma^\mu e_R U_{1\mu} \\
& + \tilde{h}_{1R} \bar{u}_R \gamma^\mu e_R \tilde{U}_{1\mu} + h_{3L} \bar{q}_L \vec{\tau} \cdot \gamma^\mu \ell_L \cdot \vec{U}_{3\mu}.
\end{aligned} \tag{B.1}$$

interaction	4 – fermion vertex	Fierz – transformed vertex
$g_{1L}\bar{q}_L^c i\tau_2 \ell_L S_1$	$-\frac{g_{1L}g_{1L}^*}{M_{S_1}^2} (\bar{q}_L^{ci}(i\tau_2)^{ij}\ell_L^j) (\bar{\ell}_L^\ell(i\tau_2)^{\ell k} q_L^{ck})$	$\frac{1}{2} \frac{g_{1L}g_{1L}^*}{M_{S_1}^2} (\bar{q}_L^k(i\tau_2)^{ij}\gamma^\mu q_L^i) (\bar{\ell}_L^\ell(i\tau_2)^{lk}\gamma_\mu \ell_L^j)$
$g_{1R}\bar{u}_R^c e_R S_1$	$\frac{g_{1R}g_{1R}^*}{M_{S_1}^2} (\bar{u}_R^c e_R) (\bar{e}_R u_R^c)$	$-\frac{1}{2} \frac{g_{1R}g_{1R}^*}{M_{S_1}^2} (\bar{u}_R \gamma^\mu u_R) (\bar{e}_R \gamma_\mu e_R)$
	$\frac{g_{1L}g_{1R}^*}{M_{S_1}^2} (\bar{q}_L^{ci}(i\tau_2)^{ij}\ell_L^j) (\bar{e}_R u_R^c)$	$\frac{1}{2} \frac{g_{1L}g_{1R}^*}{M_{S_1}^2} (\bar{u}_R(i\tau_2)^{ij} q_L^i) (\bar{e}_R \ell_L^j)$
		$-\frac{1}{8} \frac{g_{1L}g_{1R}^*}{M_{S_1}^2} (\bar{u}_R(i\tau_2)^{ij} \sigma^{\mu\nu} q_L^i) (\bar{e}_R \sigma_{\mu\nu} \ell_L^j)$
$\tilde{g}_{1R}\bar{d}_R^c e_R \tilde{S}_1$	$\frac{\tilde{g}_{1R}\tilde{g}_{1R}^*}{M_{\tilde{S}_1}^2} (\bar{d}_R^c e_R) (\bar{e}_R d_R^c)$	$-\frac{1}{2} \frac{\tilde{g}_{1R}\tilde{g}_{1R}^*}{M_{\tilde{S}_1}^2} (\bar{d}_R \gamma^\mu d_R) (\bar{e}_R \gamma_\mu e_R)$
$g_{3L}\bar{q}_L^c i\tau_2 \vec{\tau} \cdot \vec{\ell}_L \cdot \vec{S}_3$	$-\frac{g_{3L}g_{3L}^*}{M_{S_3}^2} (\bar{q}_L^{ci}(i\tau_2)^{ij}(\tau^a)^{jk}\ell_L^k)$ $(\bar{\ell}_L^\ell(i\tau_2)^{\ell m}(\tau^a)^{mn} q_L^{cn})$	$\frac{1}{2} \frac{g_{3L}g_{3L}^*}{M_{S_3}^2} (\bar{q}_L^n(i\tau_2)^{ij}(\tau^a)^{jk}\gamma^\mu q_L^i)$ $(\bar{\ell}_L^\ell(i\tau_2)^{\ell m}(\tau^a)^{mn}\gamma_\mu \ell_L^k)$
$g_{2L}\bar{d}_R^c \gamma^\mu \ell_L V_{2\mu}^\dagger$	$-\frac{g_{2L}g_{2L}^*}{M_{V_2}^2} (\bar{d}_R^c \gamma^\mu \ell_L^i) (\bar{\ell}_L^i \gamma_\mu d_R^c)$	$-\frac{g_{2L}g_{2L}^*}{M_{V_2}^2} (\bar{d}_R \gamma^\mu d_R) (\bar{\ell}_L^i \gamma_\mu \ell_L^i)$
$g_{2R}\bar{q}_L^c \gamma^\mu e_R V_{2\mu}^\dagger$	$-\frac{g_{2R}g_{2R}^*}{M_{V_2}^2} (\bar{q}_L^{ci} \gamma^\mu e_R) (\bar{e}_R \gamma_\mu q_L^{ci})$	$-\frac{g_{2R}g_{2R}^*}{M_{V_2}^2} (\bar{q}_L^i \gamma^\mu q_L^i) (\bar{e}_R \gamma_\mu e_R)$
	$-\frac{g_{2L}g_{2R}^*}{M_{V_2}^2} (\bar{d}_R^c \gamma^\mu \ell_L^i) (\bar{e}_R \gamma_\mu q_L^{ci})$	$-2 \frac{g_{2L}g_{2R}^*}{M_{V_2}^2} (\bar{q}_L^i d_R) (\bar{e}_R \ell_L^i)$
$\tilde{g}_{2L}\bar{u}_R^c \gamma^\mu \ell_L \tilde{V}_{2\mu}^\dagger$	$-\frac{\tilde{g}_{2L}\tilde{g}_{2L}^*}{M_{V_2}^2} (\bar{u}_R^c \gamma^\mu \ell_L^i) (\bar{\ell}_L^i \gamma^\mu u_R^c)$	$-\frac{\tilde{g}_{2L}\tilde{g}_{2L}^*}{M_{V_2}^2} (\bar{u}_R \gamma^\mu u_R) (\bar{\ell}_L^i \gamma^\mu \ell_L^i)$

Table B.1. Four fermion vertices for leptoquarks inferred from the Lagrangian of reference [1–3] for  $F = 0$ . Courtesy Dr. V. Cirigliano and Dr. E. Passemar [4].

interaction	4 – fermion vertex	Fierz – transformed vertex
$h_{2L}\bar{u}_R\ell_L R_2^\dagger$	$\frac{h_{2L}h_{2L}^*}{M_{R_2}^2} (\bar{u}_R \ell_L^i) (\bar{\ell}_L^i u_R)$	$\frac{1}{2} \frac{h_{2L}h_{2L}^*}{M_{R_2}^2} (\bar{u}_R \gamma^\mu u_R) (\bar{\ell}_L^i \gamma_\mu \ell_L^i)$
$h_{2R}\bar{q}_L i\tau_2 e_R R_2^\dagger$	$\frac{h_{2R}h_{2R}^*}{M_{R_2}^2} (\bar{q}_L^i e_R) (\bar{e}_R q_L^i)$ $- \frac{h_{2L}h_{2R}^*}{M_{R_2}^2} (\bar{u}_R \ell_L^i) (\bar{e}_R (i\tau_2)^{ij} q_L^j)$ $- \frac{h_{2L}h_{2R}^*}{M_{R_2}^2} (\bar{u}_R \ell_L^i) (\bar{e}_R (i\tau_2)^{ij} \ell_L^i)$ $- \frac{1}{8} \frac{h_{2L}h_{2R}^*}{M_{R_2}^2} (\bar{u}_R \sigma^{\mu\nu} q_L^j) (\bar{e}_R (i\tau_2)^{ij} \sigma_{\mu\nu} \ell_L^i)$	$\frac{1}{2} \frac{h_{2R}h_{2R}^*}{M_{R_2}^2} (\bar{q}_L^i \gamma^\mu q_L^i) (\bar{e}_R \gamma_\mu e_R)$
$\tilde{h}_{2L}\bar{d}_R\ell_L \tilde{R}_2^\dagger$	$\frac{\tilde{h}_{2L}\tilde{h}_{2L}^*}{M_{\tilde{R}_2}^2} (\bar{d}_R \ell_L^i) (\bar{\ell}_L^i d_R)$	$\frac{1}{2} \frac{\tilde{h}_{2L}\tilde{h}_{2L}^*}{M_{\tilde{R}_2}^2} (\bar{d}_R \gamma^\mu d_R) (\bar{\ell}_L^i \gamma_\mu \ell_L^i)$
$h_{1L}\bar{q}_L \gamma^\mu \ell_L U_{1\mu}$	$- \frac{h_{1L}h_{1L}^*}{M_{U_1}^2} (\bar{q}_L^i \gamma^\mu \ell_L^i) (\bar{\ell}_L^j \gamma_\mu q_L^j)$	$\frac{h_{1L}h_{1L}^*}{M_{U_1}^2} (\bar{q}_L^i \gamma^\mu q_L^j) (\bar{\ell}_L^j \gamma_\mu \ell_L^i)$
$h_{1R}\bar{d}_R \gamma^\mu e_R U_{1\mu}$	$- \frac{h_{1R}h_{1R}^*}{M_{U_1}^2} (\bar{d}_R \gamma^\mu e_R) (\bar{e}_R \gamma_\mu d_R)$ $- \frac{h_{1L}h_{1R}^*}{M_{U_1}^2} (\bar{q}_L^i \gamma^\mu \ell_L^i) (\bar{e}_R \gamma_\mu d_R)$	$\frac{h_{1R}h_{1R}^*}{M_{U_1}^2} (\bar{d}_R \gamma^\mu d_R) (\bar{e}_R \gamma_\mu e_R)$ $- 2 \frac{h_{1L}h_{1R}^*}{M_{U_1}^2} (\bar{q}_L^i d_R) (\bar{e}_R \ell_L^i)$
$\tilde{h}_{1R}\bar{u}_R \gamma^\mu e_R \tilde{U}_{1\mu}$	$- \frac{\tilde{h}_{1R}\tilde{h}_{1R}^*}{M_{\tilde{U}_1}^2} (\bar{u}_R \gamma^\mu e_R) (\bar{e}_R \gamma_\mu u_R)$	$\frac{\tilde{h}_{1R}\tilde{h}_{1R}^*}{M_{\tilde{U}_1}^2} (\bar{u}_R \gamma^\mu u_R) (\bar{e}_R \gamma_\mu e_R)$
$h_{3L}\bar{q}_L \vec{\tau} \gamma^\mu \ell_L \cdot \vec{U}_{3\mu}$	$- \frac{h_{3L}h_{3L}^*}{M_{U_3}^2} (\bar{q}_L^i (\tau^a)^{ij} \gamma^\mu \ell_L^j) (\bar{\ell}_L^\ell \gamma_\mu (\tau^a)^{\ell k} q_L^k)$	$\frac{h_{3L}h_{3L}^*}{M_{U_3}^2} (\bar{q}_L^i (\tau^a)^{ij} \gamma^\mu q_L^k) (\bar{\ell}_L^\ell \gamma_\mu (\tau^a)^{\ell k} \ell_L^j)$

Table B.2. Four fermion vertices for leptoquarks inferred from the Lagrangian of reference [1–3] for  $F = 2$ . Courtesy Dr. V. Cirigliano and Dr. E. Passemar [4].

## Appendix C

# Asymmetry dilution from thin foils

One method for addressing the challenge of determining the correction necessary to a measured asymmetry is to measure the effective dilution of asymmetry as a function of foil thickness. By using multiple foils, each with a different thickness, we can extrapolate to zero thickness, which should have the maximal asymmetry. Here we analyze the details of such an experimental approach.

We can dilute the asymmetry measurement by varying  $d$ , such as a detector window thickness, which will scatter events to the opposing rate count. A simplifying approximation of the dilution of the asymmetry due to back scatter may be given by an exponential form away from the baseline (and physical) asymmetry,  $A_0$ . The measured value is then approximately

$$A = A_0 e^{-d/\ell}. \quad (\text{C.1})$$

This gives us a form for the two rates that we can use to find  $\sigma_A$  from the Poisson statistics of  $r_1$  and  $r_2$  with errors  $\sigma_{r_1} = \sqrt{r_1/T}$  and  $\sigma_{r_2} = \sqrt{r_2/T}$ ,

$$r_1 = \frac{1}{2}R \left( 1 + A_0 e^{-d/\ell} \right) = \frac{1}{2}R (1 + A), \quad (\text{C.2})$$

and

$$r_2 = \frac{1}{2}R \left( 1 - A_0 e^{-d/\ell} \right) = \frac{1}{2}R (1 - A), \quad (\text{C.3})$$

so that

$$\sigma_A^2 = \frac{4r_1 r_2}{TR^3} = \frac{1 - A_0^2 e^{-2d/\ell}}{TR^3} = \frac{1 - A^2}{TR^3}. \quad (\text{C.4})$$

We can make a linear approximate the dilution of the asymmetry dependence on  $d$

provided  $d \ll \ell$ .

$$A \approx A_0 \left(1 - \frac{d}{\ell}\right). \quad (\text{C.5})$$

We want to estimate  $A_0$  for nonzero values of  $d$ . We can estimate the error on  $A_0$  from a least square fit of  $A$  if we spend varying amount of time  $T_i$  for each point  $d_i$ .

$$\sigma_{A_0}^2 \approx \frac{R}{\Delta} \sum_i \frac{T_i d_i^2}{1 - A_i^2}, \quad (\text{C.6})$$

where

$$\Delta = \left( \sum_i \frac{RT_i}{1 - A_i^2} \right) \left( \sum_i \frac{RT_i d_i^2}{1 - A_i^2} \right) - \left( \sum_i \frac{RT_i d_i}{1 - A_i^2} \right)^2, \quad (\text{C.7})$$

and  $A_i \approx A_0(1 - d_i/\ell)$ .

Near the limit that the foils are thin, and therefore the backscatter is small,  $A_0$  may be determined by as few as two points. Under this approximation the extrapolation is simply linear. We consider only two extreme points measured at  $d_1$  and  $d_2$  (both nonzero) for time periods  $T_1 = \lambda T$  and  $T_2 = (1 - \lambda)T$  and with asymmetries  $A_1$  and  $A_2$  as measured at those points. With

$$\sigma_{A_0}^2 \approx \frac{N}{\Delta} \left( \frac{\lambda d_1^2}{1 - A_1^2} + \frac{(1 - \lambda)d_2^2}{1 - A_2^2} \right), \quad (\text{C.8})$$

and

$$\Delta = N^2 \left[ \left( \frac{\lambda}{1 - A_1^2} + \frac{(1 - \lambda)}{1 - A_2^2} \right) \left( \frac{\lambda d_1^2}{1 - A_1^2} + \frac{(1 - \lambda)d_2^2}{1 - A_2^2} \right) - \left( \frac{\lambda d_1}{1 - A_1^2} + \frac{(1 - \lambda)d_2}{1 - A_2^2} \right)^2 \right], \quad (\text{C.9})$$

where we can minimize  $\sigma_{A_0}$  by varying  $\lambda$ .

$$\lambda = \frac{d_2 \sqrt{1 - A_1^2}}{d_2 \sqrt{1 - A_1^2} + d_1 \sqrt{1 - A_2^2}}. \quad (\text{C.10})$$

With this value, the optimal time spent on the two measurements is

$$T_1 = \frac{T d_2 \sqrt{1 - A_1^2}}{d_2 \sqrt{1 - A_1^2} + d_1 \sqrt{1 - A_2^2}}, \quad \text{and} \quad T_2 = \frac{T d_1 \sqrt{1 - A_2^2}}{d_2 \sqrt{1 - A_1^2} + d_1 \sqrt{1 - A_2^2}}. \quad (\text{C.11})$$

This gives us a minimized estimated error on  $A_0$  of

$$\sigma_{A_0} = \frac{1}{\sqrt{N}} \left| \frac{d_2 \sqrt{1 - A_1^2} - d_1 \sqrt{1 - A_2^2}}{d_2 - d_1} \right|. \quad (\text{C.12})$$

For the case that  $d$  is very small compared to  $\ell$  so that  $A_0 \approx A_1 \approx A_2$  we can use

$$\lambda = \frac{d_2}{d_2 + d_1}, \quad (\text{C.13})$$

so that the error minimized measurement times are

$$T_1 = \frac{Td_2}{d_2 + d_1}, \quad \text{and} \quad T_2 = \frac{Td_1}{d_2 + d_1}. \quad (\text{C.14})$$

This gives us an estimated error on  $A_0$  of

$$\sigma_{A_0} \approx \sqrt{\frac{1 - A_0^2}{N}}. \quad (\text{C.15})$$

# Bibliography

- [1] W. Buchmuller, R. Ruckl, and D. Wyler. Leptoquarks in lepton–quark collisions. *Physics Letters B*, 442(3-4):191, 1987.
- [2] W. Buchmuller, R. Ruckl, and D. Wyler. Erratum. *Physics Letters B*, 448(3–4):320, 1999.
- [3] S. Davidson, D. Bailey, and A. B. Campbell. Model independent constraints on leptoquarks from rare processes. *Z. Phys. C - Particles and Fields*, 61(4):613–643, 1994.
- [4] V. Cirigliano and E. Passemar. Four fermion vertices for leptoquarks. Private communication, 2012.
- [5] C. W. Misner, K. S. Thorne, and J. A. Wheeler. *Gravitation*. W. H. Freeman, San Francisco, 1970.
- [6] H. Abele, E. Barberio, D. Dubbers, F. Glueck, J. C. Hardy, W. J. Marciano, A. Serebrov, and N. Severijns. Quark mixing, CKM unitarity. *arXiv [hep-ph]*, 2003.
- [7] Sam B. Treiman, Roman Jackiw, Bruno Zumino, and Edward Witten. *Current Algebra and Anomalies*. Springer, Berlin, Germany, 1995.
- [8] S. J. Bell and R. Jackiw. A PCAC puzzle:  $\pi^0 \rightarrow \gamma\gamma$  in the  $\sigma$ -model. *Nuov. Cim. A*, 60(1):47–61, 1969.
- [9] S. Adler. Axial-vector vertex in spinor electrodynamics. *Phys. Rev.*, 177(5):2426–2438, 1969.
- [10] I. B. Khriplovich and A. R. Zhitnitsky. What is the value of the neutron electric dipole moment in the Kobayashi-Maskawa model? *Phys. Lett. B*, 109(6):490–492, 1982.

- [11] I. B. Khriplovich and S. K. Lamoreaux. *CP Violation Without Strangeness*. Springer, Berlin, 1997.
- [12] M. Pospelov and A. Ritz. Theta-induced electric dipole moment of the neutron via QCD sum rules. *arXiv [hep-ph]*, 1999.
- [13] A. C. Baker, D. D. Doyle, P. Geltenbort, K. Green, M. G. van der Grinten, G. P. Harris, P. Iaydjiev, N. S. Ivanov, R. D. J. May, M. J. Pendlebury, D. J. Richardson, D. Shiers, and F. K. Smith. Improved experimental limit on the electric dipole moment of the neutron. *Phys. Rev. Lett.*, 97(13), 2006.
- [14] S. K. Lamoreaux and R. Golub. Comment on “An improved experimental limit on the electric-dipole moment of the neutron,” C. A. Baker et al. [hep-ex/0602020]. *arXiv [hep-ex]*, 2006.
- [15] T. Bhattacharya, V. Cirigliano, S. D. Cohen, A. Filipuzzi, M. Gonzalez-Alonso, M. L. Graesser, R. Gupta, and H.-W. Lin. Probing novel scalar and tensor interactions from (ultra)cold neutrons to the LHC. *arXiv [hep-ph]*, 2011.
- [16] J. Erler and M. J. Ramsey-Musolf. Low energy tests of the weak interaction. *arXiv [hep-ph]*, 2004.
- [17] J. Beringer et al. (Particle Data Group). *Phys. Rev. D*, 86, 2012.
- [18] J. C. Hardy and I. S. Towner. Superallowed nuclear beta decays: A critical survey with tests of cvc and the standard model. *arXiv [nucl-th]*, 2004.
- [19] U. Mosel. *Fields, Symmetries, and Quarks*. Springer, Berlin, 1999.
- [20] S. Profumo, M. Ramsey-Musolf, and S. Tulin. Supersymmetric contributions to weak decay correlation coefficients. *Phys. Rev. D*, 75(7), 2007.
- [21] N. Kaiser. Isospin breaking in neutron  $\beta$ -decay and su(3) violation in semi-leptonic hyperon decays. *arXiv [nucl-th]*, 2001.
- [22] F. L. Wilson. Fermi’s theory of beta decay. *American Journal of Physics*, 36(12), 1968. A complete English translation of Fermi’s paper on beta decay published in *Zeitschrift für Physik* (1934).

- [23] Samuel S. M. Wong. *Introductory Nuclear Physics*. Wiley, New York, 1998.
- [24] J. D. Jackson, S. B. Treiman, and H. W. Wyld Jr. Possible tests of time reversal invariance in beta decay. *Phys. Rev.*, 106(3):517–521, 1957.
- [25] J. D. Jackson, S. B. Treiman, and H. W. Wyld Jr. Coulomb corrections in allowed beta transitions. *Nucl. Phys.*, 4(C):206–212, 1957.
- [26] F. Glück, I. Joó, and J. Last. Measurable parameters of neutron decay. *Nuclear Physics A*, 593(2):125–150, Oct 1995.
- [27] B. Maerkisch. Precision measurements of the neutron decay asymmetry A. American Physical Society, 2012 Annual Meeting, 2012.
- [28] G. J. Mathews, T. Kajino, and T. Shima. Big bang nucleosynthesis with a new neutron lifetime. *arXiv [astro-ph]*, 2004.
- [29] Edward W. Kolb and Michael S. Turner. *The Early Universe*. Addison-Wesley Publishing Company, Ready, Massachusetts, 1990.
- [30] J. Hardy and I. Towner. Superallowed  $0+ \rightarrow 0+$  nuclear  $\beta$  decays: A new survey with precision tests of the conserved vector current hypothesis and the standard model. *Phys. Rev. C*, 79(5), 2009.
- [31] A. P. Serebrov, M. S. Lasakov, A. K. Fomin, P. Geltenbort, A. N. Murashkin, I. A. Krasnoshekova, Yu. P. Rudnev, and A. V. Vasiliev. Superconducting UCN polarizer for a new edm spectrometer. *Nucl. Inst. and Meth. in Phys. Res. A*, 545(1–2):490–492, 2005.
- [32] J. D. Bowman and S. I. Penttila. On the measurement of the neutron lifetime using ultracold neutrons in a vacuum quadrupole trap. *J. Res. Natl. Inst. Stand. Technol.*, 110(4):361–366, 2005.
- [33] P. L. Walstrom, J. D. Bowman, S. I. Penttila, C. Morris, and A. Saunders. A magneto-gravitational trap for absolute measurement of the ultra-cold neutron lifetime. *Nucl. Inst. Meth. in Phys. Res. A*, 599:82–92, 2008.

- [34] K. P. Hickerson. A new gravito-magnetic trap for measuring the neutron lifetime using ultracold neutrons. American Physical Society, 2008 Annual Meeting of the Division of Nuclear Physics, 2008.
- [35] K. P. Hickerson. A gravito-magnetic trap for measuring the neutron lifetime using ultracold neutrons. American Physical Society, 2009 Annual Meeting of the Division of Nuclear Physics, 2009.
- [36] Ya. B. Zeldovich. *Sov. Phys. JETP*, 9:1389, 1959.
- [37] V. K. Ignatovich. *The Physics of Ultracold Neutrons*. Oxford University Press, USA, 1990.
- [38] E. Fermi and W.H. Zinn. *Phys. Rev.*, 70:103, 1946.
- [39] T. Ito and G. Prezeau. Neutrino mass constraints on beta decay. *arXiv [hep-ph]*, 2004.
- [40] The ATLAS Collaboration. Observation of a new particle in the search for the standard model higgs boson with the atlas detector at the LHC. *arXiv [hep-ex]*, 2012.
- [41] S. Chatrchyan et al. Observation of a new boson at a mass of 125 gev with the cms experiment at the lhc. *Phys. Lett. B*, 716(1):30–61, 2012.
- [42] M. Maniatis. The Next-to-Minimal Supersymmetric extension of the Standard Model reviewed. *arXiv [hep-ph]*, 2009.
- [43] S. Tulin. Private communication, 2009.
- [44] M. Hirsch, H.V. Klapdor-Kleingrothaus, and O. Panella. Double beta decay in left-right symmetric models. *Physics Letters B*, 374(1-3):7–12, 1996.
- [45] D. S. Aristizabal, M. Hirsch, and S. Kovalenko. Leptoquarks: Neutrino masses and related accelerator signals. *Phys. Rev. D*, 77(5), 2008.
- [46] S. Kovalenko. Proton stability in leptoquark models. *Phys. Lett. B*, 562(1-2):104–108, 2003.
- [47] F. Wauters, I. Kraev, D. Zákoucký, M. Beck, M. Breitenfeldt, V. Leebeeck De, V. Golovko, V. Kozlov, T. Phalet, S. Roccia, G. Soti, M. Tandecki, I. Towner,

- E. Traykov, S. Gorp Van, and N. Severijns. Precision measurements of the  $^{60}\text{Co}$   $\beta$ -asymmetry parameter in search for tensor currents in weak interactions. *Phys. Rev. C*, 82(5), Nov 2010.
- [48] F. Wauters, V. De Leebeeck, I. Kraev, M. Tandecki, E. Traykov, S. Van Gorp, N. Severijns, and D. Zakoucky. Beta asymmetry parameter in the decay of  $^{114}\text{In}$ . *arXiv [nucl-ex]*, 2008.
- [49] N. Severijns, J. Deutsch, D. Beck, M. Beck, B. Delauré, T. Phalet, R. Prieels, P. Schuurmans, B. Vereecke, and S. Versyck. Fundamental weak interaction studies using polarised nuclei and ion traps. *Hyperfine Interactions*, 129(1–4):223–236, 2000.
- [50] B. Holstein. Limit on Fierz interference in nuclear beta decay. *Phys. Rev. C*, 16(2):753–756, 1977.
- [51] Roland Winston, Jaun C. Miñano, and Pablo Benítez. *Nonimaging Optics*. Elsevier Academic Press, San Diego, 2005.
- [52] Luis Gonzalez-Mestres. *Low Temperature Detectors for Neutrinos and Dark Matter II*. Edition Frontières, 1988.
- [53] M. Baldo-Ceolin, P. Benetti, T. Bitter, F. Bobisut, E. Calligarich, et al. A new experimental limit on neutron–anti-neutron oscillations. *Z. Phys.*, C63:409–416, 1994.
- [54] Robert Golub, David J. Richardson, and Steven K. Lamoreaux. *Ultra-cold Neutrons*. Adam Hilger, New York, 1991.
- [55] D. J. Richardson and S. K. Lamoreaux. Demonstration of Berry phase using polarized neutrons. *Nucl. Inst. Meth. A*, 284:192–196, 1989.
- [56] A. Steyerl. *J. Physique*, 45 Coll. C3, Suppl. No 3:C3 255, 1984.
- [57] A. I. Frank. Optics of ultracold neutrons and the neutron-microscope problem. *Sov. Phys. Uspekhi*, 30:110–33, 1988.
- [58] A. Steyerl, W. Drexel, S. S. Malik, and E. Gutsmeidl. *Physica B*, 151:36–43, 1988.
- [59] A. Steyerl, W. Drexel, T. Ebisawa, E. Gutsmiedl, R. Gähler, K. A. Steinhauser, W. Mampe, and P. Ageron. Neutron microscopy. *Rev. Phys. Appl.*, 23:171–180, 1988.

- [60] A. Serebrov, V. Varlamov, A. Kharitonov, A. Fomin, Yu. Pokotilovski, P. Geltenbort, J. Butterworth, I. Krasnoschekov, M. Lasakov, R. Tal'daev, A. Vassiljev, and O. Zherebtsov. Measurement of the neutron lifetime using a gravitational trap and a low-temperature fomblin coating. *Phys. Lett. B*, 605:72–78, 2005.
- [61] C. R. Brome, J. S. Butterworth, K. J. Coakley, M. S. Dewey, S. N. Dzhosyuk, R. Golub, G. L. Greene, K. Habicht, P. R. Huffman, S. K. Lamoreaux, C. E. H. Mattoni, D. N. McKinsey, F. E. Wietfeldt, and J. M. Doyle. Magnetic trapping of ultracold neutrons. *Phys. Rev. C*, 63:055502, 2001.
- [62] P. Schmidt-Wellenburg, K. H. Andersen, P. Courtois, M. Kreuz, S. Mironov, V. V. Nesvizhevsky, G. Pignol, K. V. Protasov, T. Soldner, F. Vezzu, and O. Zimmer. Ultracold-neutron infrastructure for the gravitational spectrometer granit. *arXiv [nucl-ex]*, 2008.
- [63] A. Saunders, J. M. Anaya, T. J. Bowles, B. W. Filippone, P. Geltenbort, R. E. Hill, M. Hino, S. Hoedl, G. E. Hogan, T. M. Ito, K. W. Jones, T. Kawai, K. Kirch, S. K. Lamoreaux, C. Y. Liu, M. Makela, L. J. Marek, J. W. Martin, C. L. Morris, R. N. Mortensen, A. Pichlmaier, S. J. Seestrom, A. Serebrov, D. Smith, W. Teasdale, B. Tipton, R. B. Vogelaar, A. R. Young, and J. Yuan. Demonstration of a solid deuterium source of ultra-cold neutrons. *arXiv [nucl-ex]*, 2003.
- [64] F. Atchison, B. Blau, A. Bollhalder, M. Daum, P. Fierlinger, P. Geltenbort, G. Hampel, M. Kasprzak, K. Kirch, S. Köchli, B. Kuczewski, H. Leber, M. Locher, M. Meier, S. Ochse, A. Pichlmaier, C. Plonka, R. Reiser, J. Ulrich, X. Wang, N. Wiehl, O. Zimmer, and G. Zsigmond. Transmission of very slow neutrons through material foils and its influence on the design of ultracold neutron sources. *Nucl. Inst. and Meth. in Phys. Res. A*, 608(1):144–151, 2009.
- [65] C. L. Morris, T. J. Bowles, J. Gonzales, R. Hill, G. Hogan, M. Makela, R. Mortenson, J. Ramsey, A. Saunders, S. J. Seestrom, W. E. Sondheim, W. Teasdale, H. O. Back, R. W. Pattie, A. T. Holley, A. R. Young, L. J. Broussard, K. P. Hickerson, J. Liu, M. P. Mendenhall, B. Plaster, R. R. Mammei, M. Pitt, R. B. Vogelaar, R. Rios, and J. Martin. Multi-wire proportional chamber for ultra-cold neutron detection. *Nucl. Inst. and Meth. in Phys. Res. A*, 599(2-3):248–250, 2009.

- [66] A. Steyerl. Interference in the ultracold neutron transmission through thin layers. *Z. Physik*, 252(5):371–382, 1972.
- [67] O. Zimmer. Transmission of ultra-cold neutrons through a weakly absorbing foil. *Nucl. Inst. and Meth. in Phys. Res. A*, 554(1–3):363–373, 2005.
- [68] A. D. Stoica and A. V. Strelkov. Ultracold neutrons (UCN) transmission through moving goffered foils. *Nucl. Inst. and Meth.*, 157(3):477–481, 1978.
- [69] Yu. Al. Muzychka, N. Yu. Pokotilovskii, and P. Geltenbort. Search for anomalous transmission of ultracold neutrons through metal foils. *Jetp Lett.*, 67(7):459–463, 1998.
- [70] E. V. Varlamov, V. V. Nesvizhevskii, P. A. Serebrov, R. R. Tal'daev, G. A. Kharitonov, P. Geltenbort, M. Pendlebury, V. A. Strelkov, N. V. Shvetsov, and K. Schreckenbach. Observation of the penetration of subbarrier ultracold neutrons through beryllium foils and coatings. *Jetp Lett.*, 66(5):336–343, 1997.
- [71] R. Mammei. Private communication, 2009.
- [72] R. Rios. Private communication, 2012.
- [73] A. Serebrov, A. Vassiljev, M. Lasakov, I. Krasnoschekova, A. Fomin, P. Geltenbort, and E. Siber. Low energy upscattering of UCN in interaction with the surface of solid state. *Phys. Lett. A*, 367(4–5):268–270, 2007.
- [74] S. Arzumanov, J. Butterworth, R. Golub, P. Geltenbort, and E. Korobkina. Temperature dependence of the UCN loss rate. *arXiv [cond-mat]*, 2002.
- [75] S. K. Lamoreaux and R. Golub. Calculation of the ultracold neutron upscattering loss probability in fluid walled storage bottles using experimental measurements of the thermomechanical properties of fomblin. *arXiv [nucl-ex]*, 2002.
- [76] A. Holly. UCNA logbook. Private communication, 2008.
- [77] C. Hirata. Private communication, 2012.
- [78] Scott Dodelson. *Modern Cosmology*. Academic Press, Boston, Massachusetts, 2003.

- [79] A. Serebrov, V. Varlamov, A. Kharitonov, A. Fomin, Yu. Pokotilovski, P. Geltenbort, I. Krasnoschekova, M. Lasakov, R. Taldaev, A. Vassiljev, and O. Zherebtsov. Neutron lifetime measurements using gravitationally trapped ultracold neutrons. *Phys. Rev. C*, 78(3), 2008.
- [80] K. A. Olive and E. D. Skillman. A realistic determination of the error on the primordial helium abundance: Steps toward non-parametric nebular helium abundances. *arXiv [astro-ph]*, 2004.
- [81] B. D. Fields and S. Sarkar. Big-Bang nucleosynthesis (Particle Data Group mini-review). *arXiv [astro-ph]*, 2006.
- [82] B. D. Fields and S. Sarkar. Big bang nucleosynthesis. 2005. Particle Data Group.
- [83] S. Sarkar. Big Bang nucleosynthesis: tools, 2012. <http://www-thphys.physics.ox.ac.uk/people/SubirSarkar/bbn.html>.
- [84] R. V. Wagoner. Big bang nucleosynthesis revisited. *Astrophys. J.*, 179:343–360, 1973.
- [85] L. Kawano. Let’s go: Early universe. 2. Primordial nucleosynthesis: The Computer way. 1992. FERMILAB-PUB-92-004-A.
- [86] L. Kawano. Let’s Go: Early Universe. Guide to Primordial Nucleosynthesis Programming. 1988. FERMILAB-PUB-88-034-A.
- [87] Y. I. Izotov, X. T. Thuan, and A. Valentin Lipovetsky. The primordial helium abundance from a new sample of metal-deficient blue compact galaxies. *Astrophys. J.*, 435:647, 1994.
- [88] I. Y. Izotov and T. X. Thuan. Chemical enrichment by massive stars. *New Astronomy Reviews*, 44(4–6):329–334, 2000.
- [89] I. Y. Izotov and X. T. Thuan. The primordial abundance of  $^4\text{He}$ : Evidence for non-standard Big Bang nucleosynthesis. *Astrophys. J.*, 710(1):L67–L71, 2010.
- [90] J. Yuan. *Progress towards a high precision measurement of the neutron spin-electron angular correlation in polarized neutron  $\beta$  decay with ultra-cold neutrons*. PhD thesis, California Institute of Technology, 2006.

- [91] W. S. Wilburn, V. Cirigliano, A. Klein, M. F. Makela, P. L. McGaughey, C. L. Morris, J. Ramsey, A. Salas-Bacci, A. Saunders, L. J. Broussard, and A. R. Young. Measurement of the neutrino-spin correlation parameter  $B$  in neutron decay using ultracold neutrons. *Rev. Mex. de Física*, 55(2):119–122, 2009.
- [92] T.M. Ito et al. A multiwire proportional chamber for precision studies of neutron  $\beta$  decay angular correlations. *Nucl. Inst. Meth. in Phys. Res. A*, 571(3):676–686, 2007.
- [93] B. Plaster et al. A solenoidal electron spectrometer for a precision measurement of the neutron  $\beta$ -asymmetry with ultracold neutrons. *Nucl. Inst. Meth. in Phys. Res. A*, 595(3):587–598, 2008.
- [94] M. Mendenhall. Endpoint map using Xe 915 keV endpoint. Private communication, 2011.
- [95] R. W. Pattie Jr et al. First measurement of the neutron  $\beta$ -asymmetry with ultracold neutrons. *arXiv [nucl-ex]*, 2008.
- [96] J. Liu, M. Mendenhall, A. Holley, H. Back, T. Bowles, L. Broussard, R. Carr, S. Clayton, S. Currie, B. Filippone, A. García, P. Geltenbort, K. Hickerson, J. Hoagland, G. Hogan, B. Hona, T. Ito, C.-Y. Liu, M. Makela, R. Mammei, J. Martin, D. Melconian, C. Morris, R. Pattie, A. Galván Pérez, M. Pitt, B. Plaster, J. Ramsey, R. Rios, R. Russell, A. Saunders, S. Seestrom, W. Sondheim, E. Tatar, R. Vogelaar, B. VornDick, C. Wrede, H. Yan, and A. Young. Determination of the axial-vector weak coupling constant with ultracold neutrons. *Phys. Rev. Lett.*, 105(18), 2010.
- [97] M. Mendenhall. Private communication, 2012.
- [98] S. Agostinelli et al. Geant4 A simulation toolkit. *Nucl. Inst. Meth. Phys. Res. A*, 506(3):250–303, 2003.
- [99] J. Baroc J. M. Fernndez-Varead F. Salvat J. Sempaua, E. Acostab. An algorithm for Monte Carlo simulation of coupled electron-photon transport. *Nucl. Inst. Meth. Phys. Res. B*, 132(3):377–390, 1997.
- [100] C. Morris, J. Anaya, T. Bowles, B. Filippone, P. Geltenbort, R. Hill, M. Hino, S. Hoedl, G. Hogan, T. Ito, T. Kawai, K. Kirch, S. Lamoreaux, C.-Y. Liu, M. Makela,

- L. Marek, J. Martin, R. Mortensen, A. Pichlmaier, A. Saunders, S. Seestrom, D. Smith, W. Teasdale, B. Tipton, M. Utsuro, A. Young, and J. Yuan. Measurements of ultracold-neutron lifetimes in solid deuterium. *Phys. Rev. Lett.*, 89(27), 2002.
- [101] A. Saunders et al. *Rev. Sci. Instrum. A*, 2011. submitted.
- [102] Saint Gobain. Plastic scintillators, 2012. <http://www.detectors.saint-gobain.com/Plastic-Scintillator.aspx>.
- [103] A. Saunders, 2009. Private communication.
- [104] C. Feng, K. P. Hickerson, and B. Filippone. A Monte Carlo simulation for understanding energy measurements of beta particles detected by the UCNb experiment. California Institute of Technology, 2010. Summer Undergraduate Research Fellowship.
- [105] C. Feng, K. P. Hickerson, B. Filippone, and R. Russell. A Monte Carlo simulation for understanding energy measurements of beta particles detected by the UCNb experiment, 2011. Poster.
- [106] LabSphere. Technical guide: Reflectance material and coatings, 2009. <http://www.labsphere.com/uploads/technical-guides/a-guide-to-reflectance-materials-and-coatings.pdf>.
- [107] LabSphere. Spectralon design guidlines, 2009. <http://www.labsphere.com/uploads/datasheets/PB-13005-000n>
- [108] M. Makela. LDRD update, 2011. Private communication.

# Index

- $g_A$ , 8–11
- $g_S$ , 10
- $g_T$ , 10
- $g_V$ , 8–11
- $n$ -forms, 121
- backing gas, 65
- beta decay parameters, 13, 73
- Burle, 103
- Cabibbo-Kobayashi-Maskawa matrix, 4
- CAEN, 66
- convolution, 74
- convolution function, 72
- edm, *see* electric dipole moment
- electric dipole moment, 6
- Fermi, 17
- Fermi potential, 16
- Fermi, Enrico, 15
- Fierz interference
  - center-of-mass term, 20
  - energy dependence of, 21
  - Fermi term, 23, 28
  - Gamow-Teller term, 23
  - in MSSM, 24
  - in NMSSM, 27
  - in the Standard Model, 20
- Gate Valve, 107
- gravitational potential, 17
- gravity, 17
- Hamamatsu, 103
- Higgs boson, 20, 24, 27
- high-field seekers, 17
- holding field, 65
- Lab Sphere, 108
- LANSCE, 64
- leptoquarks, 27
- low-field seekers, 17
- Monte Carlo, 78
- MSSM, 24
- muon veto, 119
- MWPC, 65
- neopentane, 65
- NMSSM, 27
- nuclear form factors, 8
- PDG, 14
- Perkeo II, 13
- Perkeo III, 13
- phoswich, 118
- PMT, 65
- PMT base, 102

polarization, 76

QCD, 8

quark decay, 9

quark-lepton mixing, 28

rate model, 69

response function, 74

Richard Feynman, 1

singlino, 27

Standard Model, 20

super potential, 27

super ratio, 71

super sum, 71, 72

superfield, 27

Supersymmetry, 24

ThorLabs, 67, 68

UCN units, 17

UCN $\tau$ ,, 17

UCNA, 64, 69, 72, 80

detector model, 74

VAST, 9